

https://dspace.org/

Classical and quantum entanglement: applications to quantum communication with structured photons

Ndagano, Bienvenu Irenge

2019
https://hdl.handle.net/10539/28904

Downloaded from a DSpace repository. https://dspace.org/

University of the Witwatersrand

Higher-Order Poincaré Beams from Lasers

Author:
Hend Sroor
ORCID:
0000-0001-5364-0659

Supervisors:
Prof. Andrew Forbes
Dr. Darryl Naidoo
ORCID:
0000-0003-2552-5586
0000-0002-7774-4935

A thesis submitted in fulfilment of the requirements for the degree of Doctor of Philosophy in Science

in the

School of Physics

February 2019



Declaration of Authorship

I, Hend Sroor, declare that this thesis titled, "Higher-Order Poincaré Beams from Lasers" and the work presented in it is my own. I confirm that this work submitted for assessment is my own and is expressed in my own words. Any uses made within it of the works of other authors in any form (e.g. ideas, equations, figures, text, tables, programs) are properly acknowledged at any point of their use. A list of the references employed is included.

Signed: 

Date: February 2019

Abstract

Traditional laser systems are usually designed in such a way as to produce the fundamental Gaussian mode. The Gaussian mode, however, is not ideally suitable for all applications at hand, thus presenting the need for structured light modes. These modes have captured great attention due to their unique properties and have found a myriad of applications.

Laser modes are often characterised based on intensity measurements to infer, through propagation, the beam quality factor. This detection scheme does not consider the polarisation state of the laser mode. Therefore, it is only effective for measuring the quality of laser modes with uniform polarisation (scalar modes). Structured modes with non-uniform polarisation, namely vector beams, are usually differentiated from scalar beams by qualitative measures, for example, visual inspection of beam profiles after a rotating polariser. There is no quantitative measure defines the quality of a vector mode, i.e. a measure that can tell how vector the beams is. Consequently, there are still many open questions such as: how can we manipulate light's degrees of freedom inside the resonator to control the generation of different families of structured light? And how can we detect and characterise these modes?

The work presented in this thesis subsequently focuses on laser beam shaping inside solid state resonators. Here we will generate desirable transverse modes of structured light and develop tools to detect them. We consider two approaches for laser beam shaping inside the laser resonator. The first approach involves using amplitude masking inside unstable canonical resonators to allow controlled generation of a unique family of structured modes known as fractal modes. The second approach involves coupling of light within metasurefaces inside the resonator for the selection of pure higher-order Laguerre-Gaussian modes and superpositions thereof. Subsequent to this, we develop a novel technique to quantitatively identify the purity of structured modes based on their "vectorial" nature. Finally, we investigate how the properties of such beams change when they are amplified through birefringent and isotropic amplifiers.

Acknowledgements

I wish to express my sincere gratitude and appreciation to everyone who walked me through the journey of my PhD, particularly:

My supervisor, Prof. Andrew Forbes, for all the time and effort he spent in assisting me in my work. You have inspired me to do my best and keep trying when it became hard. You have always kept your door open to questions and discussions. I have gained invaluable knowledge during my PhD, you have taught me to be a better researcher. I am really grateful for the opportunities you have given me to expand my network, explore science beyond the African continent and learn at an international level.

Dr. Darryl Naidoo, my co-supervisor, you have helped me develop my skills as an experimental physicist. For the guidance you have given me and the things you have taught me, I sincerely thank you.

Structured Light Group, whom I had the pleasure to know. We have spent a lot of fun time together. You people have inspired me and taught me a lot of things. Thanks to all of you. Bereniece and Bienvenu, thank you for being always there for me when I always needed you in these dark days with Taj Mahal chickens raising my spirit and encouraging me to keep going.

I would like to thank my family for their unending patience and support throughout the frustrating and exciting times of my life. I wont be stronger like this without you as my inspirations. You are the reason why I kept pushing. Thanks for all the catch-up Skypes and countless Duaas.

I would also like to thank my in-laws, Aziz and Fatima for their support. Your encouragement is much appreciated.

I would like thank my husband, Muhammad, thank you for tolerating my obsession while I indulged in my madness. You always took an interest in my research and provided me with endless support.

Finally, Alhamdu w Alshokr for Allah for what you have gifted me in life.

Contents

Declaration of Authorship i

Abstract ii

Acknowledgements iii

Contents iv

List of Figures vi

List of Tables xiv

List of Publications xvi

1 Introduction 1
- 1.1 Laser Resonators . . . 2
- 1.2 Analysis of Laser Resonators . . . 4
  - 1.2.1 Diffraction Effects of the Resonator . . . 5
  - 1.2.2 The Wave Analysis of the Resonator . . . 8
- 1.3 Eigensolutions of Laser Resonators . . . 10
- 1.4 Modal Decomposition . . . 15
- 1.5 Laser Beam Shaping . . . 16
  - 1.5.1 Amplitude Modulation . . . 17
  - 1.5.2 Phase Modulation . . . 18
- 1.6 Outline . . . 20

2 Fractal Light from Lasers 23
- 2.1 Introduction . . . 24
- 2.2 Transverse Fractals . . . 25
- 2.3 Resonator Simulations . . . 26
- 2.4 3D Fractals . . . 27
- 2.5 Self-similarity of Transverse Fractals . . . 31
- 2.6 Experiment . . . 33
- 2.7 Calculation of the Parameters of the Magnified Self-conjugate Plane . . . 38

2.8 Evolution of the Intensity Distribution over the Length of the Resonator . 40
2.9 Discussion and Conclusion 40

3 Higher-Order Poincaré Beams from Lasers 42
3.1 Metasurface J-plate for Intra-cavity Conversion of Arbitrary Polarisation to OAM States 44
3.2 Experimental Implementation of the J-plates 46
3.3 Results 47
3.3.1 Generation of HOPS Beams with Conjugate OAM States 47
3.3.2 Generation of HOPS Beams with Independent OAM States 49
3.4 Conclusion 53

4 A Beam Quality Measure for Vector Beams 55
4.1 Introduction 55
4.2 Theory 56
4.3 Experiment 59
4.4 Conclusion 63

5 Amplification of Higher-Order Poincaré Beams 64
5.1 Introduction 65
5.2 Theory 65
5.3 Experimental Setup 71
5.4 Results & Discussion 72

6 Conclusion 77

Bibliography 80

List of Figures

1.1 Schematic diagram shows a simple laser system consisting of two facing mirrors where w_0 represents the beam waist and z is the optical axis. . . 2

1.2 The stability diagram of optical laser resonators as a function of g_1(x-axis) and g_2 (y-axis). The blue shaded area represents stable resonators [1]. 5

1.3 shows the simulated intensity distribution of the optical field at mirror R_1 inside a resonator consisting of two mirrors (R_1 is planar mirror and R_2 has radius of curvature of 800 mm) separated by optical distance $L = 700$ mm. The frames show the intensity (a) of the initial field (b) after one round trip, (c) 10 round trips (d) 35 round trips and (e) 40 round trips. The field reached steady state after 35 round trips as the spatial profile does not change. This simulation is calculated for light of wavelength 633 nm. The resonator mirrors were represented by a 1000×1000 matrix over a physical size of 10×10 mm. An aperture or radius 0.275 mm was placed in front of R_1 for the selection of the lowest eigenmode. Due to the absence of gain in our simulation, the intensity was normalised after each round trip. 8

1.4 Graphical representation of the polarisation states of light on the Poincaré Sphere. 10

1.5 Schematic diagram shows a Gaussian beam profile with a beam radius w. 11

1.6 Schematic diagram shows the propagation of a Gaussian beam where z_R is the Rayleigh range where the Gaussian beam size is $\sqrt{2}$ of its size at the waist. 11

1.7 Transverse intensity profiles of higher order Laguerre Gaussian modes where ℓ and p are the azimuthal and radial indices, respectively. 13

1.8 Graphical representation of the OAM states of light in a given subset $|\ell|$. 14

1.9 Higher order Poincaré sphere representing vector vortex beams of subset $|\ell| = 1$. 15

1.10 Illustration shows the general beam shaping problem where an input beam needs to go through some optical system to reshape it to a desired pattern. 16

1.11 Shows an example of amplitude modulation by aperturing an input Gaussian beam to achieve a flattop beam 17

1.12 Dynamic phase modulation using a spiral phase plate. The plate causes an azimuthally varying phase which results in a beam having a helically twisted wavefront. 18

1.13 Schematic diagram illustrates the intra-cavity phase control where a desired flattop beam is selected at the output coupler (OC). The beam is propagated to mirror R_1 where we determine the phase of the beam $e^{i\theta}$. The mirror R_1 is designed to have phase $e^{-2i\theta}$. The reflected beam then carries phase $e^{-i\theta}$. Due to the reciprocity of light, the beam returns back after one round trip to what is was. This process repeats every round trip. 20

2.1 Imaging inside an unstable canonical resonator. The two spherical mirrors, M_1 (focal length f) and M_2 (focal length F), perform geometric imaging. We define two longitudinal coordinates, z and Z. Both the z and the Z axes coincide with the optical axis, but the $z = 0$ plane coincides with the plane S, the magnified self-conjugate plane, and the $Z = 0$ plane coincides with the plane of the mirror M_2. We use z in our theoretical analysis, Z in the experimental part. The transverse coordinates are x (not shown) and y. Three-dimensional imaging during one round trip is indicated by an object in the shape of the letter "P" (shown in black) and its image, which looks like a horizontally elongated letter "b" (shown in grey): the "P" has turned into a "b" because the transverse magnification, M, is negative, and so the image of the "P" is upside-down; the "b" is horizontally elongated because the longitudinal magnification, M_l, is positive and its magnitude is greater than that of the transverse magnification. A is an aperture immediately in front of M_2. The figure is drawn for a the particularly simple case of a confocal resonator (length $F + f$; the plane S then coincides with the common focal plane) with $M = -2$ and $M_l = +4$. 26

2.2 Self-similarity of the simulated lowest-loss eigenmode's intensity distribution in the magnified self-conjugate plane, S. The frames show the intensity after 20 round trips, starting with a uniform plane wave. The self-similarity of the pattern is demonstrated by showing its centre at different magnifications (×2, ×4, ×8), resulting in a similar pattern (rotated by 180° after each magnification by a factor 2 due to the resonator's transverse magnification, M, being negative); the dotted white square in the centre of the frame marked ×1 shows the outline of the area shown in the next frame. The horizontal dotted line is the orthographic projection of the lateral self-conjugate plane S_L, in which we demonstrate, below (see Fig. 2.3), the 3D self-similarity of the light. The figure is calculated for light of wavelength $\lambda = 632.8\,\mathrm{nm}$ in a resonator of the type shown in Fig. 2.1 with $F = 16.5\,\mathrm{cm}$, $f = 8.25\,\mathrm{cm}$, $M = -2$, and a seven-sided regular polygonal aperture of circumradius $r_0 = 2.4\,\mathrm{mm}$. The beam's transverse cross-sections were represented by a 1024×1024 array of complex numbers sampled over a physical area of size $1\,\mathrm{cm} \times 1\,\mathrm{cm}$. Further details of the way this simulation, and indeed all the other simulations in this chapter, was performed are given in Section 2.3. 28

2.3 Self-similarity of the intensity distribution in a lateral self-conjugate plane, S_L, which contains the optical axis and intersects the plane S horizontally in Fig. 2.2. The vertical dotted line is the orthographic projection of the plane S. Vertically, the plots are centred on the optical axis, z. The beam is the same as that shown in Fig. 2.2. After each magnification horizontally by a factor 4 and vertically by -2, the pattern looks similar again, which is shown for different magnifications. The dotted box in the centre of the frame marked $\times 1$ marks the outline of the area shown in the next frame ($\times(-2)$ vertically, $\times 4$ horizontally). The $\times 1$ frame represents a physical area of size 2 m (horizontally) by 10 mm (vertically). 29

2.4 Self-similarity of the intensity distribution in the lateral plane of a strip resonator of the type shown in Fig. 2.1. The different frames show the centre of the intensity distribution, successively magnified by a factor M in the vertical direction and by M^2 in the horizontal direction. The $\times 1$ frame represents a physical area of size 20 m (horizontally) by 2.82 cm (vertically), centred on the magnified self-conjugate plane and the optical axis in the horizontal and vertical direction, respectively. The dotted box shown in the top left frame outlines the area shown in the top right frame. The figure was calculated for light of wavelength $\lambda = 632.8$ nm, resonator parameters $F = 70.7$ cm and $f = 50$ cm (corresponding to transverse magnification $M = -\sqrt{2}$), and the aperture A was a slit of width 2.08 cm. Each beam cross-section was represented on 4096-element array of complex numbers, representing a physical width 4 cm. 30

2.5 Axial (a) and transverse (b) intensity cross-section through the field around the self-conjugate point at the centre of the plane S in the strip resonator from Fig. 2.4. Like in Figs. 2.2, 2.3 and 2.4, the self-similarity is demonstrated by successive magnifications, each of which stretches the part of the curve between the vertical dotted lines to the full width. The width of the curves marked $\times 1$ represents a physical length of 2 m (a) and 2.08 cm (b). The intensity range represented by the different curves has been adjusted so that corresponding features in the curves have roughly the same vertical size. 31

2.6 Evolution of the self-similarity of transverse intensity cross-sections upon propagation for the eigenmodes shown in Figs. 2.2 and 2.3 (a) and in Figs. 2.4 and 2.5 (b). The self-similarity is quantified here by $-d^2$, the negative of the normalised squared Euclidean distance between the central rectangle of the intensity cross-section in the transverse plane with the given z coordinate, and the central rectangle of the same size of the intensity cross-section after being stretched in the transverse directions by a factor M. The magnification was $M = -3$ in (a) and $M = -2$ in (b). The width and height of the central rectangle were arbitrarily chosen to be 1/4 of the width and height of the calculated intensity cross-section. The dotted vertical lines indicate the planes of the mirrors, M_1 and M_2, and the magnified self-conjugate plane, S. 33

2.7 Experimental setup, (a) schematic and (b) photo with the laser running. (a) The cavity comprised two concave mirrors, M_1 (radius of curvature R_1, corresponding to focal length $f = R_1/2$) and M_2 (radius of curvature R_2, focal length $F = R_2/2$), and an output coupler (OC) angled at 45° with a 99.8% reflectivity. The geometrical length of the cavity was G, that of the Nd:YAG gain medium was g. S is the magnified self-conjugate plane. One out of a variety of polygonal apertures was positioned in front of M_2. The intensity cross-section in the self-conjugate plane S was captured outside the cavity at a distance $R_2/2$ from M_2 using a CCD camera. (b) Clearly visible is the gain-medium assembly (bright yellow; centre) and the mounts for the end mirrors and the output coupler. The two tubes (light blue; bottom left) connecting to the gain-medium assembly are cooling tubes for the gain medium. 34

2.8 A few of the transverse intensity patterns recorded inside a resonator for parameters $F = 250\,\text{mm}$, $f = 75\,\text{mm}$, and $G = 343\,\text{mm}$. The self-conjugate plane S is positioned at $Z = Z_S = 231.8\,\text{mm}$. 35

2.9 Self-similarity of the intensity cross-sections in different transverse planes near the predicted position of the self-conjugate plane, $Z = Z_S = 231.8\,\text{mm}$. The images in the top row show the central $\approx 4\,\text{mm} \times 4\,\text{mm}$ of the experimentally recorded intensity cross-sections in the transverse planes $Z = 220\,\text{mm}$ (left), $Z = 230\,\text{mm}$ (center), and $Z = 240\,\text{mm}$ (right). The images in the bottom row show the centers of the corresponding top-row images, stretched by a factor $M = -3.32$, that is, stretched by a factor 3.32 and rotated by 180°. To show structure over a wider intensity range, the brightness of each pixel is proportional to the logarithm of the recorded intensity. 36

2.10 Evolution of the self-similarity upon propagation of measured transverse intensity cross-sections. Like in Fig. 2.6, the plot shows the negative normalised squared Euclidean distance, $-d^2$, as a function of axial coordinate Z. The predicted position of the self-conjugate plane S, $Z = Z_S = 231.8\,\text{mm}$, is indicated by a dotted black line surrounded by a grey area representing experimental uncertainties. The planes of the mirrors, M_1 and M_2, and the self-conjugate plane, S, are indicated by vertical dotted lines. 37

2.11 Collage of experimentally obtained intensity cross-sections measured close to the self-conjugate plane S inside a variety of laser cavities. The edge of the aperture in the central column is that of the 3rd iteration of the Koch snowflake (the first iteration being an equilateral triangle), the other apertures are regular hexagons. r_0 is the circumradius of the apertures, M is the approximate transverse round-trip magnification, and N_F is the Fresnel number. Like in Fig. 2.9, brightness is proportional to the logarithm of intensity. 38

2.12 Evolution of the eigenmode intensity cross-section between mirrors M_2 ($Z = 0\,\text{mm}$) and M_1 ($Z = 350\,\text{mm}$). The magnification was $M = 3.32$ ($F = 250$ mm, $f = 75\,\text{mm}$) with an aperture of circumradius $r_0 = 2\,\text{mm}$. The geometrical length of the cavity was $G = 350\,\text{mm}$, corresponding to an effective length of $L = 308.5\,\text{mm}$ due to the refractive index of the gain medium. 41

3.1 Illustration of (a) a HOPS representing vector vortex modes in the left and right polarisation basis and (b) a Generalised HOPS representing the vector vortex modes in the horizontal and vertical basis. The output beam profile is displayed at different positions on the sphere with arrows indicating polarisation distribution. 42
3.2 Schematic shows the transverse modes inside an unfolded cavity around the output coupler M_2 during one round trip. For some linear polarisation state represented by a double side arrow, the purity of the polarisation state is controlled by a half-wave plate HWP. Upon transmission through the J-plate, the beam acquires OAM of topological charge ℓ. Acting in reverse the OAM state is suppressed while maintaining the initial polarisation state and self repeating mode. 45
3.3 Experimental schematic of a nonlinear overlapped IR/green laser resonator for the intra-cavity generation of HOPS beams. The IR resonator consists of two mirrors M_1 and M_2 with Nd:YAG gain medium. The IR resonator serves as a pump for the second harmonic generation resonator. The overlapped green cavity comprised mainly of a KTP crystal that is placed in the resonators overlapped region and two mirrors M_3 and M_4 (green output coupler). A polarising beam splitter (PBS) is used to set the intra-cavity polarisation to the horizontal. The HWP is rotatable at some angle θ for controlling the polarisation states incident on the J-plate resulting in the active selection of arbitrary vector vortex modes. 46
3.4 Shows conversion efficiency of the second harmonic generation beam through a single pass (blue data points) and within a cavity configuration (red data points) together with their fitting curves (solid line). 48
3.5 Modal decomposition measurements are executed on the output mode to evaluate the modal weightings when the HWP angle $\theta = 0°$, $22.5°$ and $45°$. (b) shows the raw data where on-axis intensity (as indicated by the cross-hairs) means existence of the mode while no intensity indicates the mode's absence. 49
3.6 (a) Shows a pure vector vortex mode selected by propagating a diagonally polarised light through the J-plate. (b) shows a qualitative test of the vector vortex mode by passing it through a linear polariser. The orientation of the polariser is depicted by double side arrows 49
3.7 Shows azimuthal inner product measurements executed to evaluate the modal weightings of the output state. The measurements confirm the existence of pure $LG_{0,1}$ at HWP angle $\theta = 0°$ while pure $LG_{0,5}$ at $\theta = 45°$. (b) shows the raw data for the measurements at the Fourier plane where on-axis intensity means mode exists, null intensity means absence of the mode. 50
3.8 The output intensity profile of the laser after placing the J-plate 2. The output mode evolves from pure $LG_{0,1}$ at HWP angle $\theta = 0°$ mode to pure $LG_{0,5}$ at $\theta = 45°$ with superposition state in between. 51
3.9 Shows azimuthal inner product measurements executed to evaluate the modal weightings of the output state. The measurements confirm the existence of pure $LG_{0,10}$ at HWP angle $\theta = 0°$ while pure $LG_{0,100}$ at $\theta = 45°$. (b) shows the raw data for the measurements at the Fourier plane where on-axis intensity means the mode exists, null intensity means absence of the mode. 51

3.10 The output intensity profile of the laser after placing the J-plate 3. The output mode evolves from pure $LG_{0,10}$ at HWP angle $\theta = 0$ mode to pure $LG_{0,100}$ at $\theta = 45°$ with superposition state in between. 52
3.11 Shows the nano-antennas diffract light with no modulation when the incident beam size is bigger that metasurface active area. The incident beam was 3.2 mm in diameter while the active area of the metasurface was 2 mm in diameter. 52
3.12 A set of four subfigures. 54

4.1 Experimental generation and analysis of vector modes. Using a half-wave plate ($\lambda/2$) to adjust the polarisation of the fundamental Gaussian mode, we generated cylindrical vector modes with a q-plate of topological charge $q = 1/2$. The q-plate is aligned such that its global phase is zero with respect to the horizontal axis. The generated vector modes was directed into two detection systems. On one hand, we distinguished between vector modes using a sorter, whereby the beam was passed through a second q-plate and a polarising beam splitter (PBS); the two acting as a correlation filter. The output of the correlation was measured at the Fourier plane using a Fourier lens (FL). On the other hand, we determined the vector quality factor by performing a series of polarisation projections using a polarisation grating (PG), and OAM projections using phase patterns encoded on the spatial light modulator (SLM). The outputs were measured in the Fourier plane of two Fourier lenses. BS: beam splitter, CCD: charge-coupled device 58
4.2 Sorting of radially and azimuthally polarised vector vortex beams. By measuring the on-axis intensity, the relative weightings of radially and azimuthally polarised vector modes were determined for both pure and superposition states. 59
4.3 Graphical depiction of the actual intensity measurements corresponding to those of Table 1, with the holograms shown in each column and the two polarisation measurements in the rows. We illustrate two examples, (a) a vector vortex mode and (b) a scalar vortex mode. The scalar mode has only one polarisation component and is separable, whereas the vector mode has both and is non-separable. 61
4.4 Evolution of the vector quality factor (V) with respect to the nature of the input state. Using a quarter-wave plate, the polarisation of the input Gaussian beam was varied from linear to circular, such that the vortex beam generated after the q-plate varied from vector to scalar, respectively. The purity was calculated from the 12 decomposition measurements (red dots) and plotted against the theoretical prediction (blue solid line) for each orientation of the quarter-wave plate. The experimental images show the relative intensities of the left- and right-circular polarisation states for different orientations of the quarter-wave plate. 62
4.5 Single shot measurement of the purity using demultiplexing holograms. Both the left- and right-circularly polarised arms are decomposed using the same set of holograms, such that the upper row of intensities corresponds to the left-circularly polarised arm and the bottom row to the right-circularly polarised arm. (b) and (c) show the intensity patterns of vector and scalar vortex beams on the CCD camera, respectively. 63

5.1 Schematic of a general solid state amplifier crystal. (a) shows the crystal positioned with its fast axis at an angle $\theta = 0$ with respect to the vertical. (b) shows the two field components relative to the c-axis when the crystal is rotated by an angle θ. 67

5.2 (a) The Vector Quality Factor, V_{out}, as a function of crystal angle, θ, for three cases: $\alpha = 0.5$ and $\eta_R = 2$ (blue), $\alpha = 0.8$ and $\eta_R = 0.1$ (orange), and $\alpha = 0.4$ and $\eta_R = 0.1$ (green). The 3D plots of the parameter space show the richness of the theory, with the input state fixed in (b) and (c) at $\alpha = 0.5$ and $\alpha = 0.7$, respectively. In (d) and (e) the amplification factor is fixed at $\eta_R = 0.2$ and $\eta_R = 1$, respectively. 70

5.3 Illustration of the experimental setup for the MOPA system. Generation: a fundamental Gaussian mode was converted into a HOPS beam by the combination of a polariser (Pol), quarter-wave plate (QWP) and a q-plate. In our experiment the q-plate had a topological charge $\ell = 2q = 1$. Amplification: either Nd:YAG (non-birefringent) or Nd:YLF (birefringent) crystals, with the ability to rotate the field relative to the crystal axes by the use of half wave plates (HWP) and Dove Prisms (DP). Quality Detection: a polarising beam splitter (PBS) separated the two polarisation components (horizontal and vertical) while the spatial light modulator (SLM) performed spatial projections to infer the vector purity using a quantum toolkit. The actual measurements were collected on a camera (CCD) in the far-field at the focal plane of a lens (FL). The beam insets show the evolution from the Gaussian mode through to an amplified vector beam (radially polarised in this example), finally measured by twelve projections at the camera. 71

5.4 Measured (data points) and theoretical (solid lines) amplification factors for each polarisation component for the two crystals as a function of the crystal angle. Nd:YLF is a strong birefringent medium resulting in the oscillating behaviour, while Nd:YAG is a weakly birefringent resulting in almost equal gain for both the horizontal and vertical components of the beam. No fitting parameters were used in the theoretical plots. 72

5.5 Purity of VV beams over the different orientation of Nd:YAG (red) and Nd:YLF (blue) amplifiers when the seed VV beam has purity $V_{\text{in}} = 1$. . . 73

5.6 Measured (data points) and calculated (solid lines) purity variation as a function of the crystal angle for two incident VV beams: $\tilde{U}_1 = 0.976\exp(i\ell\phi)\,\hat{\mathbf{e}}_{\mathbf{H}} + 0.267\exp(-i\ell\phi)\,\hat{\mathbf{e}}_{\mathbf{V}}$ and $\tilde{U}_2 = 0.267\exp(i\ell\phi)\,\hat{\mathbf{e}}_{\mathbf{H}} + 0.976\exp(-i\ell\phi)\,\hat{\mathbf{e}}_{\mathbf{V}}$, both having initial purity of $V_{\text{in}} = 0.5$. For Nd:YAG, the purity is predicted not to change, in agreement with measured data showing only a marginal oscillation about $V_{\text{out}} = 0.5$. For Nd:YLF the purity for $\tilde{U}_1$ (blue) and $\tilde{U}_2$ (red) oscillate predictably. At some angles the purity decreases ($\theta = 0$ for $\tilde{U}_2$) while at others it increases ($\theta = \pi/2$ for $\tilde{U}_2$). 74

5.7 Measured (data points) and calculated (solid lines) variation in purity after the amplifier with the crystal angle fixed at $\theta = 0$. For Nd:YLF, the blue dots represent the output purity for beams with $\alpha \in [0.5, 1]$ in Eq. 5.1. The red dots represent the output purity for beams with $\alpha \in [0, 0.5]$. For Nd:YAG, the purity does not change and equates to the purity of the incident seed beam. 74

5.8 The output power for a purely VV seed beam as a function of the amplifier pump power. The initial power of the seed beam was 164 mW. The experimental data (data points) for both Nd:YAG (red) and Nd:YLF (blue) amplifiers is in good agreement with theory (solid curves). Inset images indicate the beam intensity profiles with the corresponding output purity at three pump strengths: low (A), medium (B) and high (C). . . . 75

List of Tables

1.1 Examples of ray transfer matrices for a spherical mirror and beam propagation through free space. 3

2.1 Resonator parameters used to design fractal cavities of various magnifications. 37

3.1 Shows the different J-plates used inside the non-linear resonator with the corresponding output OAM mode when the incident polarisation on the J-plate are horizontal and vertical polarisation. 48

4.1 Designation of normalised intensity measurements 58

To Muhammad,

For his support, his patience, and his faith,
Because he always understood.

List of Publications

Peer-reviewed Journal Papers:

1. Bienvenu Ndagano, **Hend Sroor**, Melanie McLaren, Carmelo Rosales-Guzmán, and Andrew Forbes, "Beam quality measure for vector beams", *Optics Letters*, **41**(15), 3407 (2016).

2. **Hend Sroor**, Nyameko Lisa, Darryl Naidoo, Igor Litvin, and Andrew Forbes, "Purity of vector vortex beams through a birefringent amplifier", *Physical Review Applied* , **9**(4), 044010 (2018).

3. **Hend Sroor**, Darryl Naidoo, Steven W. Miller, John Nelson, Johannes Courtial, and Andrew Forbes, "Fractal light from lasers", *Physical Review A* , in press.

4. **Hend Sroor**, Igor Litvin, Darryl Naidoo, and Andrew Forbes, "Amplification of Higher-Order Poincaré beams through Nd:YLF and Nd:YAG crystals", *Applied Physics B*, submitted.

5. **Hend Sroor**, Antonio Ambresio, Yao-Wei Huang, Darryl Naidoo, Fredrico Capasso, and Andrew Forbes, "Metasurfaces J-plate laser", in preparation.

International Conference Papers:

1. **Hend Sroor**, Bienvenu Ndagano, Melanie McLaren, Carmelo Rosales-Guzman, and Andrew Forbes. "Vector quality measure for vector beams", Proc. SPIE **9950**, 99500F (2016)

2. Bienvenu Ndagano, **Hend Sroor**, Melanie McLaren, Carmelo Rosales-Guzman, and Andrew Forbes. "Measuring the non-separability of optical fields", Proc. SPIE **10120**, 101200W (2017).

3. **Hend Sroor**, Darryl Naidoo, Johannes Courtial, and Andrew Forbes. "Generation of fractal structured eigenmodes from lasers", Proc. SPIE **10549**, 105490B (2018).

4. **Hend Sroor**, Nyameko Lisa, Darryl Naidoo, Igor Litvin, and Andrew Forbes. "Generation and amplification of vector vortex beams", Proc. SPIE **10518**, 105181T (2018).

5. **Hend Sroor**, Darryl Naidoo, Johannes Courtial, and Andrew Forbes. "A novel laser resonator for fractal modes", Proc. SPIE **10518**,105181N (2018).

6. **Hend Sroor**, Nyameko Lisa, Darryl Naidoo, Igor Litvin, and Andrew Forbes. "Cylindrical vector beams through amplifiers", Proc. SPIE **10511**, 105111M (2018).

Chapter 1

Introduction

Laser beam shaping, structuring and tailoring light are different terms that describe the process of creating customised laser beams. This process was realised shortly after the invention of the laser in 1960 aiming to obtain a Gaussian beam at the output of a laser. This was achieved by inserting a circular aperture inside the cavity to limit the transverse extent of the beam [2, 3].

The Gaussian beam has been widely used for industrial manufacturing applications such as cutting, welding and drilling. However, there are many applications where the Gaussian beam is not ideally suitable for all applications at hand. For example, a laser beam with a flat-top intensity distribution provides a superior quality to a Gaussian beam in material processing applications. Optical vortex beams provide new degrees of freedom (channels) in which information can be encoded for optical communications. Accordingly, there has been an increase in the number of applications that demand customised laser beams with particular phase and intensity distribution, namely structured light modes. The majority of them are spatial modes with uniform polarisation, the so-called scalar modes. Recently, laser modes with non-uniform polarisation distribution, namely vector beams, have become topical due to the scope of their applications in topics as diverse as optical microscopy [4], optical tweezers [5–10], quantum memories [11, 12] and data encryption [13].

Many tools have been developed over the years for shaping the laser beam external to the cavity by modifying an existing laser beam to any desired transverse profile. Nonetheless intra-cavity laser beam shaping has more advantages over extra-cavity beam shaping such as higher output purity as the desired spatial structured mode is amplified after each round trip while the undesired modes fail to stabilise inside the cavity and thus end up vanishing inside the resonator [14].

In this chapter, we will start with a brief introduction covering the basic theory of laser resonators. We will explore the optical fields that form inside laser resonators. We will then focus on the optical fields that reproduce themselves after each round trip, the so-called eigenmodes of the laser resonator. We will classify these modes based on their vector nature from scalar to vector modes. This will be followed by a discussion of the fundamental Gaussian solution of a resonator as well as higher-order solutions. Finally, we will discuss the different approaches that have been developed for extra-cavity generation of structured modes as well as intra-cavity generation approaches.

1.1 Laser Resonators

A simple laser resonator, or laser cavity, consists of two mirrors that face each other and are separated by an optical distance. If the resonator's mirrors are planar, it is quite difficult to trap light unless they are perfectly parallel. One way to easily confine light between the mirrors is to add curvature to one or both of the mirrors [15] as shown in Fig. 1.1.

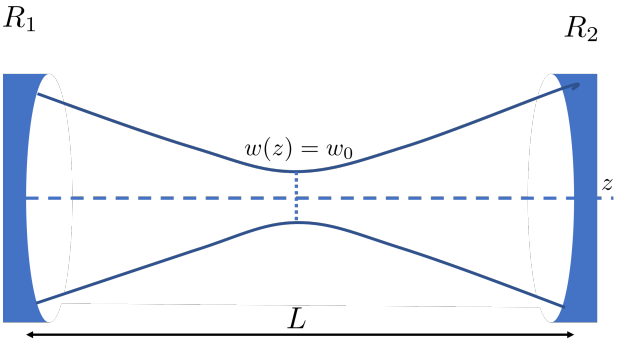


FIGURE 1.1: Schematic diagram shows a simple laser system consisting of two facing mirrors where w_0 represents the beam waist and z is the optical axis.

The basic properties of an optical resonator such as stability can be geometrically determined using the ray transfer matrix approach [15, 16]: assume an initial optical ray $X_0 = \begin{bmatrix} x_0 \\ y_0 \end{bmatrix}$ is passing through an optical system that is described by an ABCD transfer matrix. The output is then given by

$$X_1 = \begin{bmatrix} x_1 \\ y_1 \end{bmatrix} = \begin{bmatrix} A & B \\ C & D \end{bmatrix} \begin{bmatrix} x_0 \\ y_0 \end{bmatrix}, \tag{1.1}$$

where x_0 and x_1 are the positions of the initial and final optical rays, respectively. y_0 and y_1 are the angles of the initial and final optical rays, respectively. If the initial

optical ray is transformed through n-number of optical systems, then the final ray is represented by

$$X_f = \begin{bmatrix} x_f \\ y_f \end{bmatrix} = \begin{bmatrix} A_n & B_n \\ C_n & D_n \end{bmatrix} \begin{bmatrix} A_{n-1} & B_{n-1} \\ C_{n-1} & D_{n-1} \end{bmatrix} \ ... \begin{bmatrix} A_1 & B_1 \\ C_1 & D_1 \end{bmatrix} \begin{bmatrix} x_0 \\ y_0 \end{bmatrix} \tag{1.2}$$

$$= \begin{bmatrix} A_t & B_t \\ C_t & D_t \end{bmatrix} \begin{bmatrix} x_0 \\ y_0 \end{bmatrix}. \tag{1.3}$$

TABLE 1.1: Examples of ray transfer matrices for a spherical mirror and beam propagation through free space.

Optical element	Spherical mirror of radius R	Optical path of length L
Ray transfer matrix	$\begin{pmatrix} 1 & 0 \\ \frac{-2}{R} & 0 \end{pmatrix}$	$\begin{pmatrix} 1 & L \\ 0 & 1 \end{pmatrix}$

We apply this to a simple resonator consisting of two concave mirrors facing each other, separated by a distance L, as shown in Fig. 1.1. We define the path of the optical ray to start from the mirror R_1, propagating through free space distance L to mirror R_2, and reflecting back towards R_1, the plane where it started. The ABCD matrices that describe mirrors and free space propagation is represented in Table 1.1. Thus, the ray transfer matrix that describes one round trip is given by

$$M = \begin{bmatrix} 1 & 0 \\ \frac{-2}{R_2} & 0 \end{bmatrix} \begin{bmatrix} 1 & L \\ 0 & 1 \end{bmatrix} \begin{bmatrix} 1 & 0 \\ \frac{-2}{R_1} & 0 \end{bmatrix} \begin{bmatrix} 1 & L \\ 0 & 1 \end{bmatrix} \tag{1.4}$$

$$= \begin{bmatrix} 1 - \frac{2L}{R_1} & 2L - \frac{2L^2}{R_1} \\ \frac{-2}{R_1} - \frac{2}{R_2} + \frac{4L}{R_1 R_2} & \frac{-2L}{R_1} + 1 - \frac{2L}{R_2} - \frac{4L^2}{R_1 R_2} \end{bmatrix}. \tag{1.5}$$

We can simply express this process as a linear combination of eigenvalues ν and eigenvectors

$$M \begin{bmatrix} x_0 \\ y_0 \end{bmatrix} = \sum_i \nu_i \begin{bmatrix} x_i \\ y_i \end{bmatrix}. \tag{1.6}$$

The eigenvalues of Eq. 1.5 can be evaluated as

$$\nu = \frac{\mathrm{Tr}(M) \pm \sqrt{\mathrm{Tr}(M)^2 - 4}}{2}, \tag{1.7}$$

where $\mathrm{Tr}(M)$ is the trace of the operator matrix M and is equivalent to

$$\mathrm{Tr}(M) = 4\left[1 - \frac{L}{R_1}\right]\left[1 - \frac{L}{R_2}\right] - 2. \tag{1.8}$$

After n-round trips, the optical ray inside the resonator is expressed as

$$\begin{bmatrix} x_f \\ y_f \end{bmatrix} = M^n \begin{bmatrix} x_0 \\ y_0 \end{bmatrix} = \sum_i \nu_i^n \begin{bmatrix} x_i \\ y_i \end{bmatrix}. \tag{1.9}$$

For the optical ray to be confined inside the system for all n-round trips, the associated eigenvalues ν_i must not diverge (grow without limits). This necessitates $|\nu_i| \leq 1$ and thus $|\mathrm{Tr}(M)| \leq 2$ [17]. Therefore, the condition for the resonator to be stable is given by

$$0 \leq \left[1 - \frac{L}{R_1}\right]\left[1 - \frac{L}{R_2}\right] \leq 1. \tag{1.10}$$

For an optical resonator that follows Eq. 1.10, the optical ray will be periodically refocused and stay bounded inside. Such resonator is called a stable resonator. If the resonator does not follow Eq. 1.10, the optical ray will tend to converge and disperse after each round trip. Such a resonator is referred to as unstable resonator.

To show graphically which resonator is stable and which is unstable, we plot a stability diagram on where each resonator is represented by a point. This is shown in Fig. 1.2: the stability parameters $g_1 = 1 - (L/R_1)$ and $g_2 = 1 - (L/R_2)$ are illustrated as the coordinate axes; stable laser systems are represented by points on the shaded blue areas.

1.2 Analysis of Laser Resonators

In this section, we will discuss which optical field exists inside a resonator. We are mainly interested in the optical field that reproduces itself after each round trip, namely eigenmodes of the resonator. Geometrically for an optical field to be considered as an eigenmode, the curvature of the field's wavefront must match the curvature of the mirrors inside the resonator. However, this geometric treatment is an approximation and does not consider the spatial field distribution of the eigenmodes inside the resonator.

The exact description of the optical field propagating inside a resonator can be obtained using one of the two following approaches: 1) the diffraction effects of the resonator's

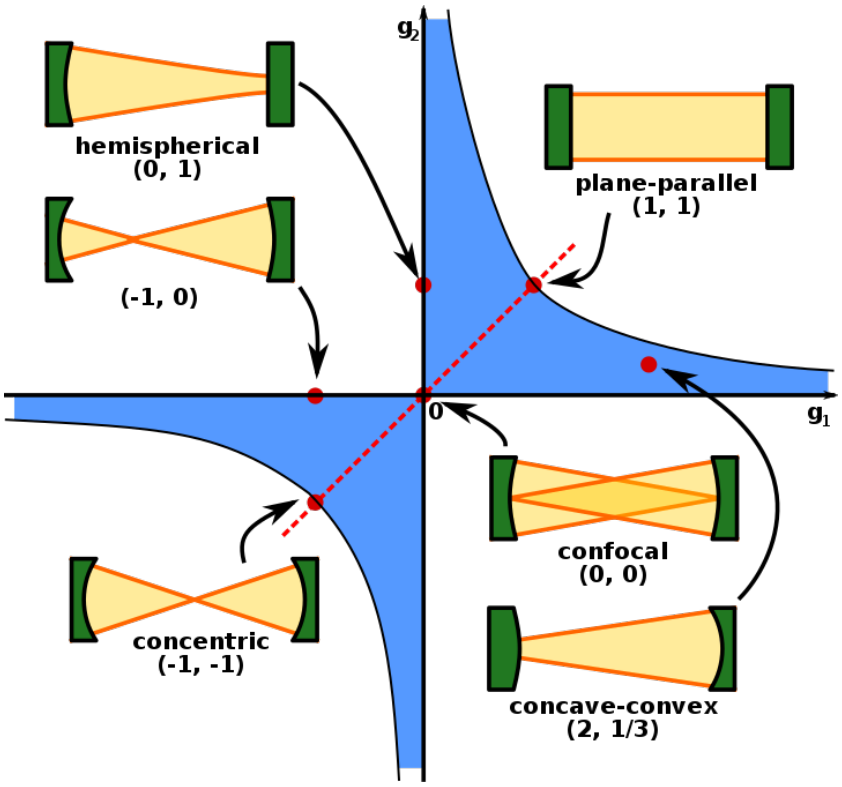


FIGURE 1.2: The stability diagram of optical laser resonators as a function of g_1(x-axis) and g_2 (y-axis). The blue shaded area represents stable resonators [1].

mirrors using Huygens' principle, 2) derive the wave equation of the optical field from Maxwell's equations.

1.2.1 Diffraction Effects of the Resonator

The optical field inside a resonator was first calculated by Fox and Li [18]. This method is based on the diffraction effects caused by the resonator's mirrors. To simplify the problem, we assume the dimension of the mirrors are finite but large in comparison to the wavelength [17, 18]. If the initial field at the first mirror is considered to be arbitrary, then the Fresnel-Kirchhoff formulation of Huygens' principle can be invoked to obtain the optical field at the second mirror which is given by

$$u_2(x_2, y_2) = \sqrt{\frac{i}{\lambda L}} \int\int u_1(x_1, y_1) \exp\left(-\frac{i\pi}{\lambda L}\left[(x_2 - x_1) + (y_2 - y_1)\right]^2\right) \mathrm{d}x_1 \mathrm{d}y_1, \quad (1.11)$$

where $u_1(x_1, y_1)$ and $u_2(x_2, y_2)$ are the relative optical field distributions at the first and second mirrors, respectively. λ represents the wavelength and L is the distance between

the mirrors. The optical field reflecting back onto the first mirror can be expressed in terms of the reflected field as

$$u_1(x_1, y_1) = \sqrt{\frac{i}{\lambda L}} \int\int u_2(x_2, y_2) \exp\left(-\frac{i\pi}{\lambda L}\left[(x_1 - x_2) + (y_1 - y_2)\right]^2\right) \mathrm{d}x_2 \mathrm{d}y_2. \quad (1.12)$$

Equation 1.11 and Eq. 1.12 represent the single transit equation. By combining the equations we obtain the optical field after one round trip. The optical field undergoes n-number of round trips till it settles down to a steady state. At this state, the optical field does not change its distribution, however it might experience a decrease in amplitude due to diffraction losses given by $\zeta = \frac{u_n}{u_{n-1}}$. This optical field is called the eigenmodes of the resonator.

The Fox-Li approach has been used to predict the lowest loss eigenmode inside laser resonators. However, this process is time consuming as one has to integrate Eq. 1.11 and Eq. 1.12 n-iterations to calculate the eigenmode at the mirrors, where n is the number of round trips required to reach the steady state. The Matrix Method approach overcomes this limitation. This approach is based on replacing the integral in Eq. 1.11 with a product of two matrices [19]. One matrix represents the initial field and the other represents the transformation of the field through the resonator. This can be accomplished by dividing the mirrors into N-parts, each with size $\Delta x_2 = 2h_2/N$ for second mirror of radius h_2. Similarly, the first mirror of radius h_1 is sub-divided into N-parts of size $\Delta x_1 = 2h_1/N$. If the segments Δx_1 and Δx_2 are small enough, the field across each segment can be considered as a constant. Thus Eq. 1.11 becomes

$$\begin{aligned} u_2(x_2, y_2) &= \sqrt{\frac{i}{\lambda L}} \int\int u_1(x_1, y_1) \exp\left(-\frac{i\pi}{\lambda L}\left[(x_2 - x_1) + (y_2 - y_1)\right]^2\right) \mathrm{d}x_1 \mathrm{d}y_1 \\ &= \sqrt{\frac{i}{\lambda L}} \sum_i^N \sum_j^N u_1\left(h_1 - i\Delta x_1, h_2 - i\Delta x_2\right) \\ &\int_{h_1 - i\Delta x_1}^{h_1 - (i+1)\Delta x_1} \int_{h_2 - j\Delta x_2}^{h_2 - (j+1)\Delta x_2} \exp\left(-\frac{i\pi}{\lambda L}\left[(x_2 - x_1) + (y_2 - y_1)\right]^2\right) \mathrm{d}x_1 \mathrm{d}y_1. \end{aligned} \quad (1.13)$$

We can express Eq. 1.13 in the matrix form as

$$u_2 = T u_1, \quad (1.14)$$

where

$$u_2 = \begin{bmatrix} u_2(x_{21}, y_{21}) \\ u_2(x_{22}, y_{22}) \\ . \\ . \\ . \\ u_2(x_{2N}, y_{2N}) \end{bmatrix}, \tag{1.15}$$

$$u_1 = \begin{bmatrix} u_1(x_{11}, y_{11}) \\ u_1(x_{12}, y_{12}) \\ . \\ . \\ . \\ u_1(x_{1N}, y_{1N}) \end{bmatrix}, \tag{1.16}$$

$$T = \begin{bmatrix} T_{11} & T_{12} & . & . & T_{1N} \\ T_{21} & T_{22} & . & . & . \\ . & . & . & . & . \\ T_{N1} & . & . & . & T_{NN} \end{bmatrix}, \tag{1.17}$$

and

$$T_{ij} = \sqrt{\frac{i}{\lambda L}} \int_{h_1 - i\Delta x_1}^{h_1 - (i+1)\Delta x_1} \int_{h_2 - j\Delta x_2}^{h_2 - (j+1)\Delta x_2} \exp\left(-\frac{i\pi}{\lambda L} \left[(x_2 - x_1) + (y_2 - y_1) \right]^2 \right) \mathrm{d}x_1 \mathrm{d}y_1. \tag{1.18}$$

This method drastically reduces the computational time since the operator matrix T is only evaluated once. To calculate the eigenmodes of the resonator, we simply calculate T for one round trip. We then express T as a linear combination of eigenvalues and eigenvectors (as in Eq. 1.6). The output of multiple round trips is achieved by raising the power of the eigenvalues to the number of round trips (as in Eq. 1.9).

Figure 1.3 shows the intra-cavity optical field calculated using the Matrix Method for an optical resonator consists of two mirrors ($R_1 = \infty$ and $R_2 = 800$ mm) separated by distance $L = 700$ mm. The initial optical field was given by a rectangular function as shown in Fig. 1.3 (a). The intensity distribution of the field $I = |u(x, y)|^2$ was observed at Mirror R_1. The eigenmode was reached after approximately 35 round trips. The radius of the lowest order eigenmode was measured to be 0.23 mm as theoretically expected.

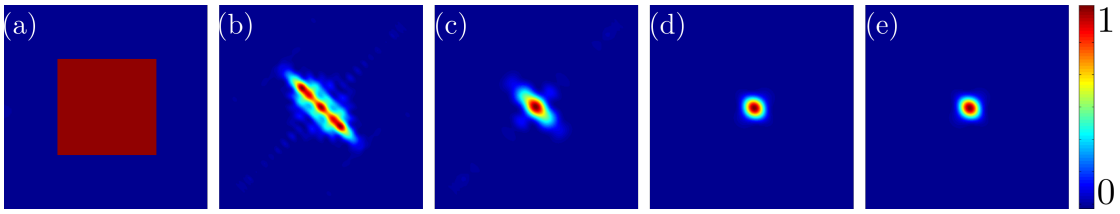


FIGURE 1.3: shows the simulated intensity distribution of the optical field at mirror R_1 inside a resonator consisting of two mirrors (R_1 is planar mirror and R_2 has radius of curvature of 800 mm) separated by optical distance $L = 700$ mm. The frames show the intensity (a) of the initial field (b) after one round trip, (c) 10 round trips (d) 35 round trips and (e) 40 round trips. The field reached steady state after 35 round trips as the spatial profile does not change. This simulation is calculated for light of wavelength 633 nm. The resonator mirrors were represented by a 1000×1000 matrix over a physical size of 10×10 mm. An aperture or radius 0.275 mm was placed in front of R_1 for the selection of the lowest eigenmode. Due to the absence of gain in our simulation, the intensity was normalised after each round trip.

1.2.2 The Wave Analysis of the Resonator

In the preceding section, we calculated the intra-cavity optical field based on the diffraction effects of the mirrors. In this section, we will only consider the wave nature of laser beams.

An optical field of a beam can be described in the form of Maxwell's equations in free space where

$$\nabla \cdot \hat{E} = 0, \tag{1.19}$$

$$\nabla \cdot \hat{B} = 0, \tag{1.20}$$

$$\nabla \times \hat{E} = -\frac{\partial \hat{B}}{\partial t}, \tag{1.21}$$

$$\nabla \times \hat{B} = \frac{1}{c^2}\frac{\partial \hat{E}}{\partial t}, \tag{1.22}$$

where $\hat{E}$ is the electric field component, $\hat{B}$ is the magnetic field component, c represents the speed of light and ∇ is the Laplacian operator. The wave equation is then obtained by taking the curl of Eq. 1.21 (Faraday's Law of Induction)

$$\nabla \times (\nabla \times \hat{E}) = \frac{\partial(\nabla \times \hat{B})}{\partial t} \tag{1.23}$$

$$\nabla(\nabla \cdot \hat{E}) - \nabla^2 \hat{E} = -\frac{\partial(\nabla \times \hat{B})}{\partial t}. \tag{1.24}$$

From Eq.1.19 and Eq.1.22, we can express Eq.1.24 as

$$\nabla^2 \hat{E} - \frac{1}{c^2}\frac{\partial^2 \hat{E}}{\partial t^2} = 0. \tag{1.25}$$

Equation 1.25 is the time-dependent Helmholtz wave equation. We can derive the time-independent Helmholtz equation by exploiting the method of separation of variables to reduce the complexity of the analysis, yielding

$$(\nabla^2 + \hat{k}^2)\hat{E}(x, y, z) = 0, \tag{1.26}$$

where $\hat{k}$ is the wave vector and is defined as $|k| = \frac{2\pi}{\lambda}$ with λ as the wavelength. Within the paraxial approximation (see [20]), an optical field $\hat{E}(x, y, z)$ is expressed as

$$\hat{E}(x, y, z) = \hat{u}(x, y, z)\exp(ikz), \tag{1.27}$$

where $\hat{u}(x, y, z)$ is a slowly varying complex function, and z is the axis of propagation. Substituting the above form of the electric field (Eq. 1.27) into the Helmholtz wave equation (Eq. 1.26) and approximate it in the paraxial regime where

$$\left|\frac{\partial^2 \hat{u}(x, y, z)}{\partial^2}\right| << k\left|\frac{\partial \hat{u}(x, y, z)}{\partial z}\right|, \tag{1.28}$$

one can obtain the paraxial approximation of the Helmholtz wave equation that is expressed as

$$\left(\frac{\partial^2}{\partial x^2} + \frac{\partial^2}{\partial y^2}\right)\hat{u}(x, y, z) + 2ik\frac{\partial \hat{u}(x, y, z)}{\partial z} = 0. \tag{1.29}$$

Equation 1.29 is used to describe the propagation of laser beams. If the electric field of the laser beam oscillates in a uniform direction, this represents a light beam with uniform polarisation, denoted as scalar beams. These beams possess a state of polarisation that is represented by a point on the surface of the Poincaré Sphere [21, 22]. The poles represent modes with left and right circular polarisation while the equator represents modes with linear polarisation as illustrated in Fig. 1.4. However, if the electric field of a beam oscillates in different directions in the transverse plane, then the solution of Eq. 1.29 is a vector beam and is given by

$$\hat{u}(x, y, z) = [\hat{\mathbf{u}}_1\hat{\mathbf{e}}_1 + \hat{\mathbf{u}}_2\hat{\mathbf{e}}_2]\exp(ikz), \tag{1.30}$$

where $\hat{\mathbf{e}}_1$ and $\hat{\mathbf{e}}_2$ represent the polarisation states associated to electric field components $\hat{\mathbf{u}}_1$ and $\hat{\mathbf{u}}_2$, respectively.

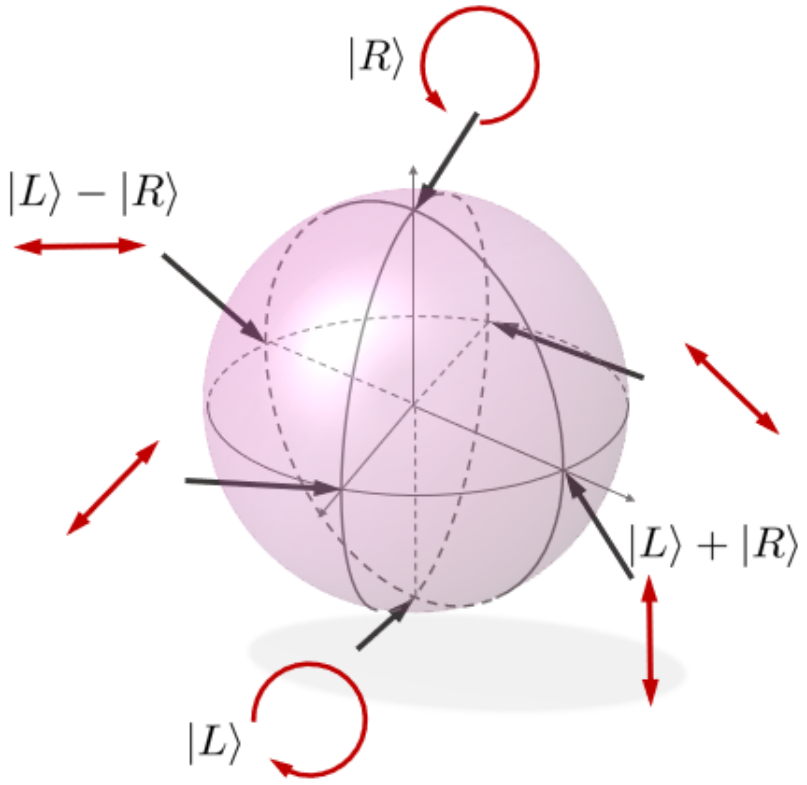


FIGURE 1.4: Graphical representation of the polarisation states of light on the Poincaré Sphere.

1.3 Eigensolutions of Laser Resonators

There are many solutions to Eq. 1.26 in the Cartesian (Hermite Gaussian) and cylindrical coordinate basis (Laguerre Gaussian, Bessel), however, we will not discuss all of these solutions; instead we will focus on the solutions which have been implemented in this thesis, namely Laguerre Gaussian solutions.

The Gaussian mode is the lowest order solution and it is perhaps the most important. The Gaussian mode is given by

$$u_G = u_0 \exp\left(\frac{-r^2}{w^2}\right) \tag{1.31}$$

where u_0 is the normalisation constant of the electric field, w is the radius at which the intensity of the field falls to $1/e^2$ of the maximum intensity, as shown in Fig. 1.5. The total intensity of the electric field is $I = |u_0|^2$ The Gaussian mode contracts to a minimum diameter of $2w_0$ at the beam waist where the wavefront phase is planar. At a distance z away from the waist, diffraction due to propagation causes the wavefront to acquire curvature as shown in Fig. 1.6. The curvature of the wavefront is given by

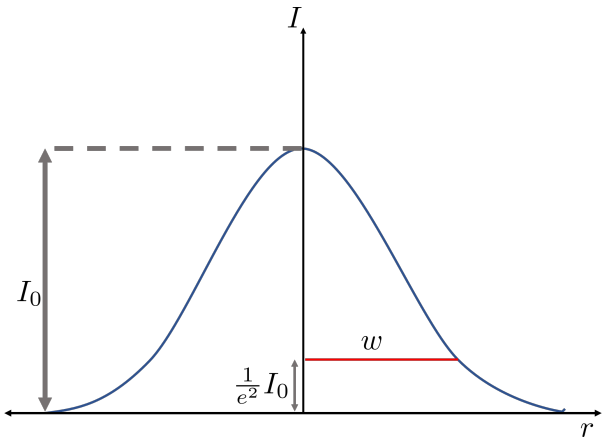


FIGURE 1.5: Schematic diagram shows a Gaussian beam profile with a beam radius w.

$$R(z) = z\left[1 + \left(\frac{\pi w_0^2}{\lambda z}\right)^2\right]. \tag{1.32}$$

In the far field ($z \to \infty$), the wavefront returns to an approximately planar phase. The size of the Gaussian mode at any spatial plane is expressed as

$$w(z) = w_0\left[1 + \left(\frac{\lambda z}{\pi w_0^2}\right)^2\right]^{\frac{1}{2}}. \tag{1.33}$$

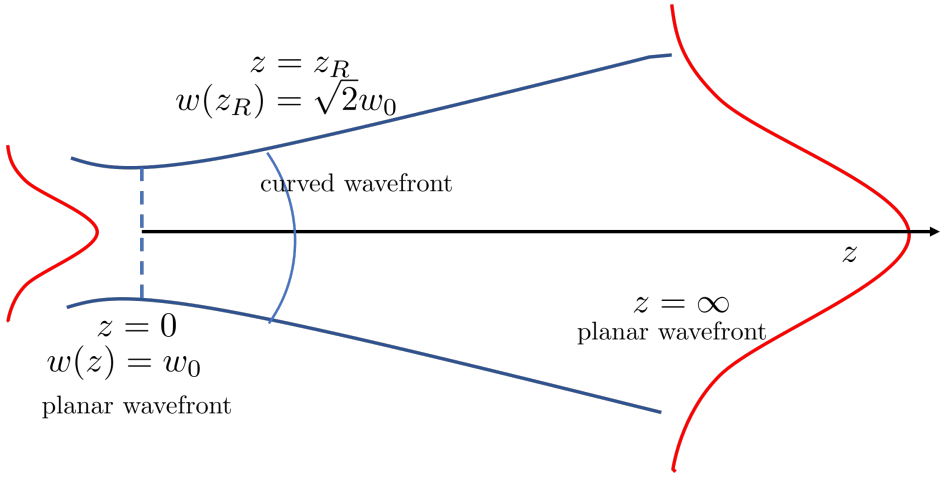


FIGURE 1.6: Schematic diagram shows the propagation of a Gaussian beam where z_R is the Rayleigh range where the Gaussian beam size is $\sqrt{2}$ of its size at the waist.

The Gaussian mode is not the only solution for the paraxial wave equation. There are many other solutions that exist, such as the Laguerre Gaussian (LG) modes whose

electric field can be represented as

$$\begin{aligned} \mathrm{LG}_{p,\ell}(r,\phi,z) = \sqrt{\frac{2p!}{\pi(p+|\ell|)!}}\frac{1}{w(z)}\exp\left[\frac{-r^2}{w^2(z)} - \frac{ikr^2}{2R(z)}\right] L_p^{|\ell|}\left[\frac{2r^2}{w^2(z)}\right] \\ \times \left[\frac{\sqrt{2}r}{w(z)}\right]^{|\ell|} \exp[i\ell\phi]\exp\left[-i(2p+|\ell|+1)\arctan\left(\frac{z}{z_R}\right)\right], \end{aligned} \tag{1.34}$$

where p and ℓ are the radial and azimuthal indices of the transverse mode, z_R is the Rayleigh range, $w(z)$ is the Gaussian beam width at propagation distance z, $R(z)$ is the radius of curvature of the beam wavefront at position z, ϕ is the azimuthal angle and $L_p^{|\ell|}$ is the Laguerre polynomial.

As $|\ell|$ increases, the azimuthally-varying phase factor $\exp(i\ell\phi)$ helically twists the wavefront around the optical axis. The number of twists in the wavefront is given by $|\ell|$. This azimuthally varying phase possesses a discontinuity on the optical axis of the beam, resulting in the formation of an optical vortex. This optical vortex manifests in the form of a null intensity at the centre of the beam. Laguerre Gaussian modes are characterised by intensity distributions that are radially symmetric. The intensity patterns of some $\mathrm{LG}_{p,\ell}$ beams are shown in Fig. 1.7. The azimuthal index ℓ controls the size of central vortex while the radial index p denotes the number of the concentric rings the mode possesses.

These modes possess quantised orbital angular momentum (OAM) $\ell\hbar$ per photon. Analogue to polarisation, the OAM carried by the beam can be represented by a higher OAM sphere as shown in Fig. 1.8. Here the poles correspond to orthogonal OAM states while the equator represents equally weighted superpositions of OAM states [21, 23–25].

Higher-order LG modes (i.e $\ell \neq 0$) have a radius $w_{p,\ell}$ that is related to the radius of the Gaussian (zero-order) mode w and is given by

$$w_{p,\ell} = w\sqrt{2p+|\ell|+1}. \tag{1.35}$$

The curvature of the wavefront $R(z)$ in Eq. 1.32 is the same for all resonator modes. However, the phase shift Φ is a function of the mode indices and can be obtained from

$$\Phi(p,\ell,z) = (2p+|\ell|+1)\arctan\left(\frac{\lambda z}{\pi w_0^2}\right). \tag{1.36}$$

If the resonator is limited by an aperture, only eigenmodes whose beam radius are smaller than the radius of the aperture can oscillate, and thus been observed. As a rule

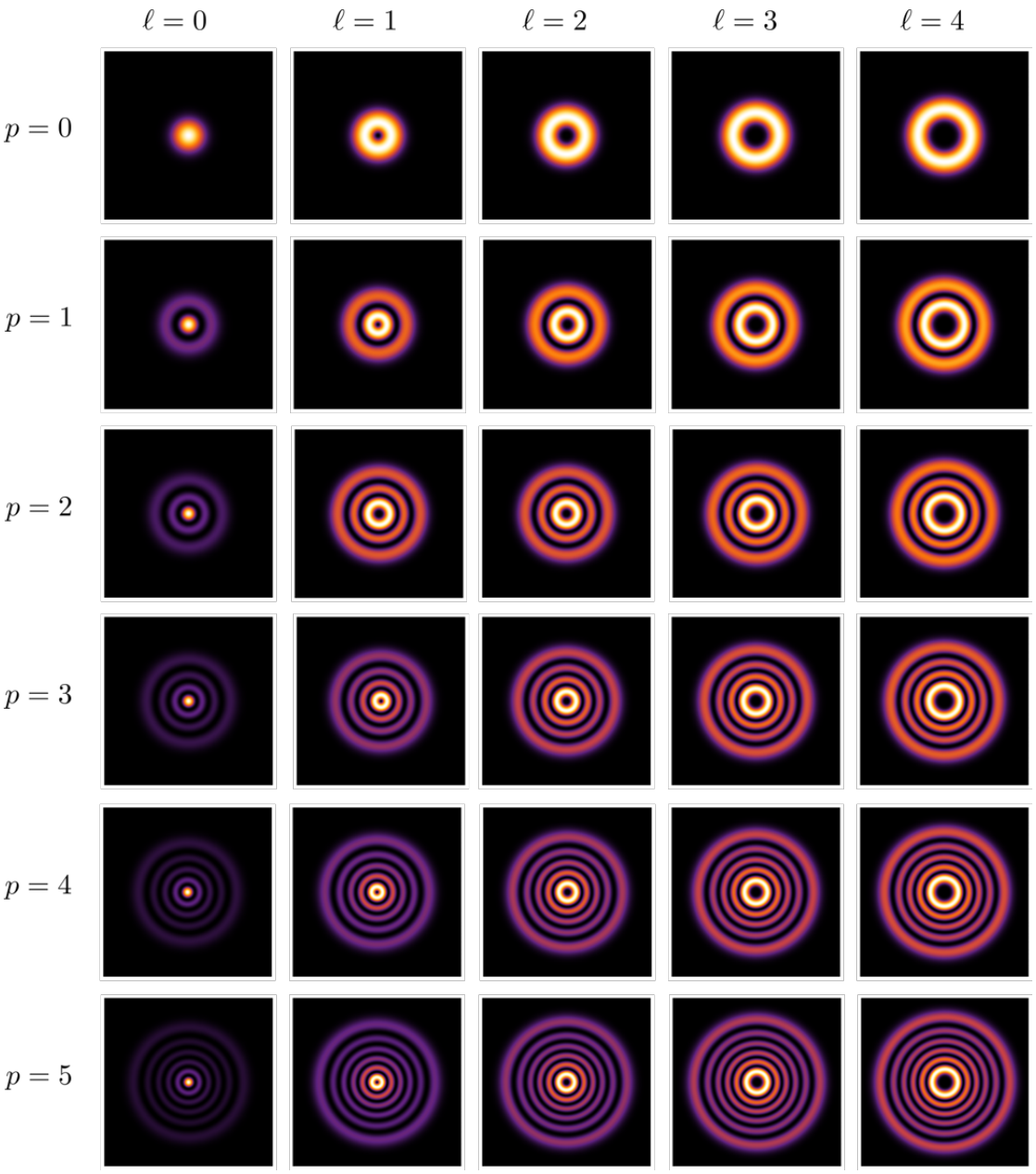


FIGURE 1.7: Transverse intensity profiles of higher order Laguerre Gaussian modes where ℓ and p are the azimuthal and radial indices, respectively.

of a thumb, the radius of the aperture must be greater than 0.9:1 of the beam radii. Only Gaussian modes require an aperture radius of 0.9:1.3 times the Gaussian radius. The upper and lower values of the aperture radius correspond to higher and lower gain, respectively [15].

All the above-proposed eigenmodes represent the scalar solutions of Eq. 1.26. Although vector modes are direct solutions of Eq. 1.30, they are usually generated as a superposition of two orthogonal scalar fields with two orthogonal states of polarisation. For example, we can write cylindrical symmetric vector vortex (VV) beams in terms of two

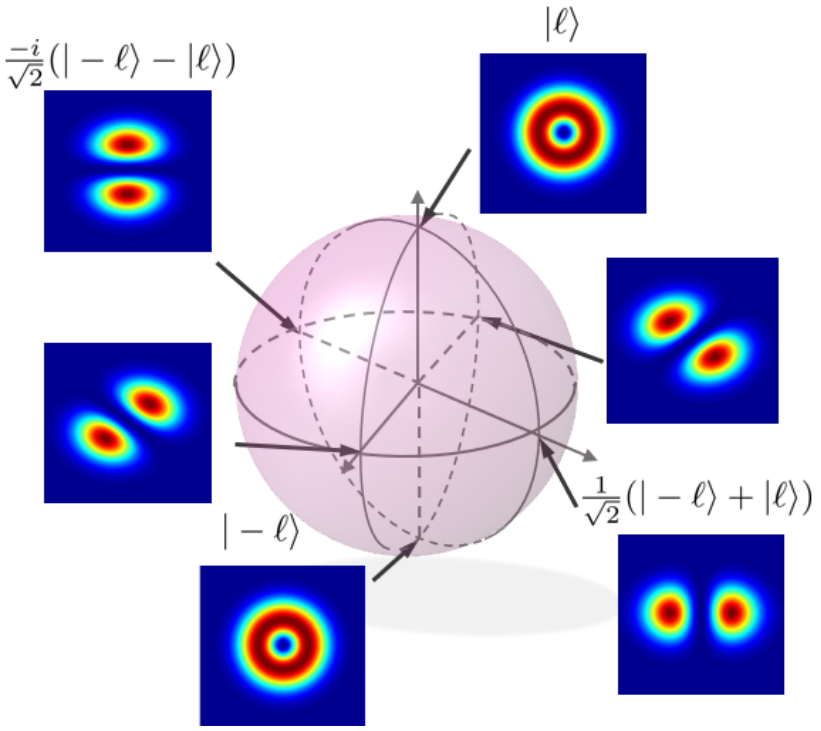


FIGURE 1.8: Graphical representation of the OAM states of light in a given subset $|\ell|$.

orthogonal LG modes as

$$U(r) = \mathrm{LG}_{p_1,\ell_1}\hat{\mathbf{e}}_{\mathbf{R}} + \gamma \mathrm{LG}_{p_2,\ell_2}\hat{\mathbf{e}}_{\mathbf{L}}. \tag{1.37}$$

where γ is the intermodal phase, $\hat{\mathbf{e}}_{\mathbf{R}}$ and $\hat{\mathbf{e}}_{\mathbf{L}}$ are vectors representing the right- and left-circular polarisation corresponding to the optical fields LG_{p_1,ℓ_1} and LG_{p_2,ℓ_2}, respectively. Although polarisation is limited to two orthogonal bases, VV modes are represented by an infinite set of solutions due to an infinite number of linear combinations of possible spatial modes [26].

Vector vortex beams can be theoretically mapped onto the surface of the Higher-Order Poincaré Sphere (HOPS) [27] which is a combination of the Bloch sphere and OAM sphere. The poles correspond to scalar orthogonal modes while the equator represents equally weighted superpositions of the two orthogonal scalar modes. Figure 1.9 illustrates a HOPS with $p = 0$, $\ell = \pm 1$. The radially and azimuthally polarised beams, as well as the two hybrid states, occupy the equator.

Scalar and vector modes form a complete and orthogonal set of functions and are called "modes of propagation". Every laser beam can be expanded in terms of these modes.

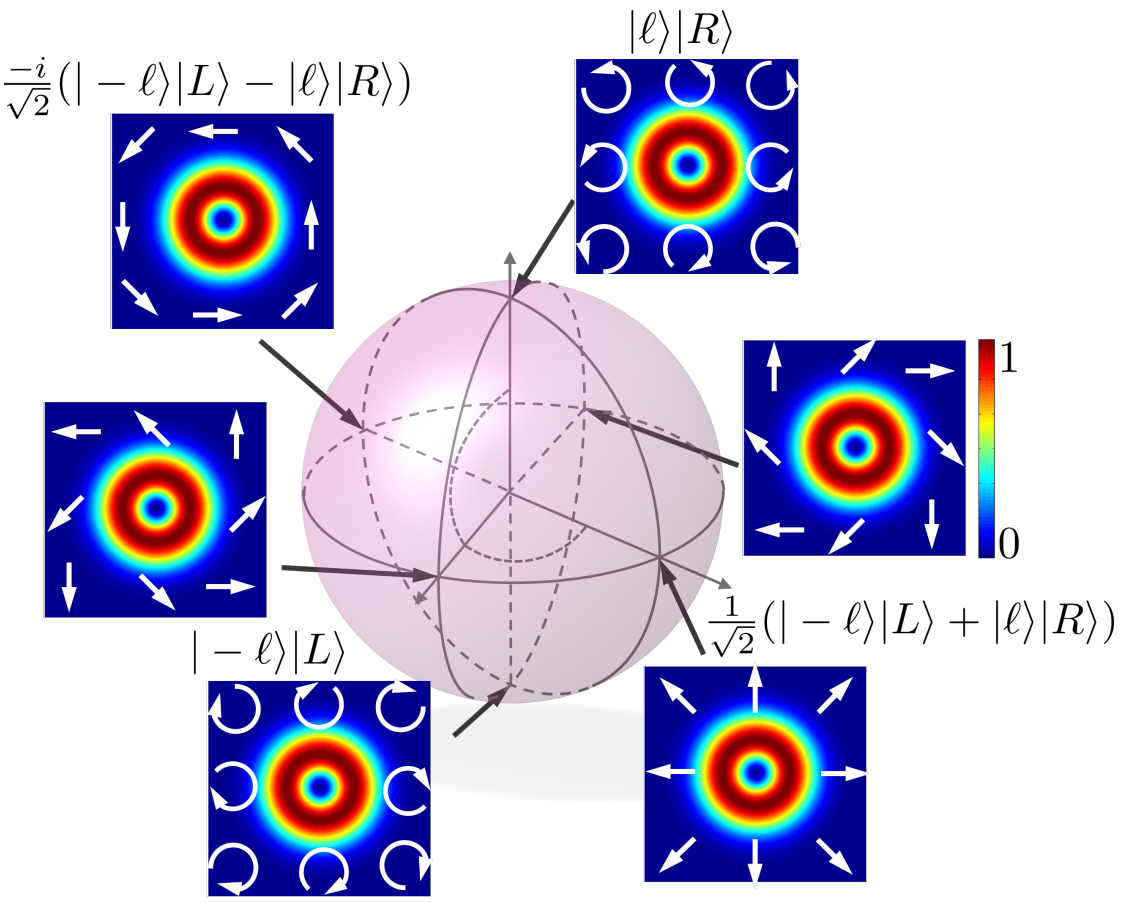


FIGURE 1.9: Higher order Poincaré sphere representing vector vortex beams of subset $|\ell| = 1$.

1.4 Modal Decomposition

Identifying a beam by measuring it's intensity profile is not a reliable method to characterise the beam. For example, a beam with an apparent Gaussian intensity profile does not mean that it is the fundamental Gaussian mode. There is also a probability that it is a sum of non-Gaussian modal components, which consequently will propagate differently to the Gaussian mode [28]. Therefore, it is essential to express the beam as a linear combination of basis modes [29]

$$U(x,y) = \sum_{n=0}^{\infty} c_n \Psi_n(x,y), \tag{1.38}$$

where $U(x,y)$ represents the output field and c_n represents the modal weighting of a specific basis mode $\Psi_n(x,y)$. The coefficients c_n can be found by executing an inner product that is given by:

$$c_n = \langle \Psi_n(x,y) | U(x,y) \rangle = \int\int U(x,y)\Psi_n^*(x,y)\mathrm{d}x\mathrm{d}y \tag{1.39}$$

where $*$ represents the complex conjugate. An arbitrary beam can be decomposed completely into the basis modes once the modal weighting of each mode is determined. These coefficients can be calculated by performing the inner product of the resultant field $u(r) = U(x,y)\Psi_n^*(x,y)$ at the Fourier plane to give

$$U_F(k_x,k_y) = \mathcal{F}(u(x,y)) = \int\int U(x,y)\Psi_n^*(x,y)\exp[-i(k_x x + k_y y)]\mathrm{d}x\mathrm{d}y, \tag{1.40}$$

Optically, these modal weightings are evaluated by measuring the on-axis intensity of the field in the Fourier plane by setting the propagation vectors $k_x = k_y = 0$ to get

$$I(0,0) = U_f(0,0) = \left| \int\int U(x,y)\Psi_n^*(x,y)\mathrm{d}x\mathrm{d}y \right|^2 = |c_n|^2 \tag{1.41}$$

1.5 Laser Beam Shaping

Laser beam shaping is the process of modifying an existing beam (extra-cavity beam shaping) or forcing a desired beam to exit a laser resonator (intra-cavity beam shaping). Since the intensity of the beam defines its spatial profile while the phase determines its propagation properties, laser beam shaping techniques mainly target controlling these two characteristics.

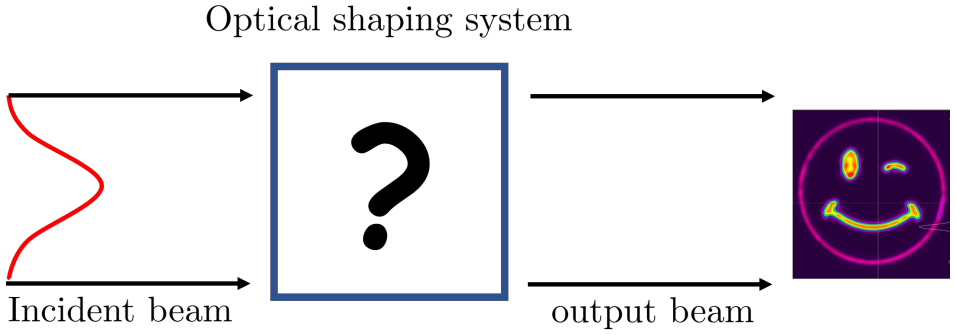


FIGURE 1.10: Illustration shows the general beam shaping problem where an input beam needs to go through some optical system to reshape it to a desired pattern.

The general beam shaping problem is illustrated in Fig. 1.10, where a beam is incident upon an optical system that must operate on it to produce a desired beam. This problem can be formulated as

$$u_1(x, y) = u_0(x, y)t(x, y), \tag{1.42}$$

where $u_0(x, y)$ is the input optical field, $u_1(x, y)$ is the output shaped field, $t(x, y)$ is the transmission function of the optical shaping system. This problem can be easily solved by calculating $t(x, y)$. All we need is to choose $u_1(x, y)$ and $u_0(x, y)$, then $t(x, y)$ will simply be $\frac{u_1(x,y)}{u_0(x,y)}$. In the following section we will discuss what approaches can be used to shape light into a desired beam.

1.5.1 Amplitude Modulation

The first approach to shape $u_0(x, y)$ to a desired field $u_1(x, y)$ is to modulate the beam's amplitude. In this case, the transmission function $t(x, y)$, in Eq. 1.42, would represent an amplitude mask function [30]. The reshaped beam can be observed in the near field after the mask. This approach has been widely used to select flattened intensity distribution beams from an input Gaussian beam by eliminating the extent of the input beam to a more uniform intensity profile as shown in Fig. 1.11 [31, 32]. Recently, the concept of amplitude modulation is achieved by reshaping an input beam within a pump-shaped amplifier. This provides regions of high and low gain on the profile of the input field and can thus function in a similar way to insert regions of loss [33].

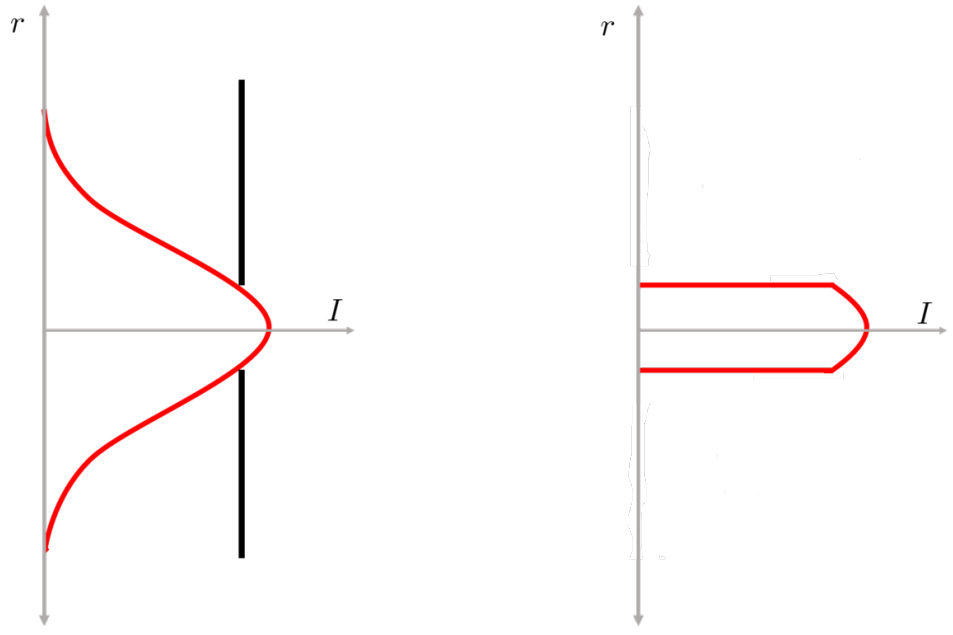


FIGURE 1.11: Shows an example of amplitude modulation by aperturing an input Gaussian beam to achieve a flattop beam

1.5.2 Phase Modulation

It is possible to shape a laser beam by controlling its phase. In this case, the transmission function $t(x, y)$ in Eq. 1.42 is replaced by a phase function $e^{i\theta}$. The wavefront and the spatial profile of both input and output beams are needed to be identified. Once they are determined, one can then establish an optical element with the phase function that can produce the output shaped beam. The output beam, however is only shaped in the far field [15, 31]. The field at the Fourier plane is given by

$$u_{1F}(k_x, k_y) = \mathcal{F}(u_0(x, y)e^{i\theta}) = \int\int u_0(x, y)e^{i\theta}\exp\left[-i(k_x x + k_y y)\right] \mathrm{d}x\mathrm{d}y, \tag{1.43}$$

where $e^{i\theta}$ is the phase function acquired by the phase shaping system. This approach has been implemented by modulating the dynamic phase of Gaussian beam to produce a desired output beam. The word dynamic refers to the phase that is acquired by a beam as a result of its propagation through an isotropic medium where

$$\theta = \hat{k} \cdot \hat{r} = \frac{2\pi}{\lambda}(n_p - n_0)d(x, y) \tag{1.44}$$

where $\hat{k}$ is the wave vector, $\hat{r}$ is the optical path, n_p and n_0 are the refractive indices of the phase plate and the air, respectively, $d(x, y)$ is the thickness of the phase plate. Different designs of dynamic phase plates are accomplished by either varying the thickness $d(x, y)$ or by varying the refractive index. Examples for these phase plates are refractive and diffractive optical elements and deformable elements [30, 34–41]. Figure 1.12 shows a spiral phase plate which is a transparent material with a gradually increasing thickness that works like a vortex lens to convert a Gaussian beam into a desired vortex mode [42].

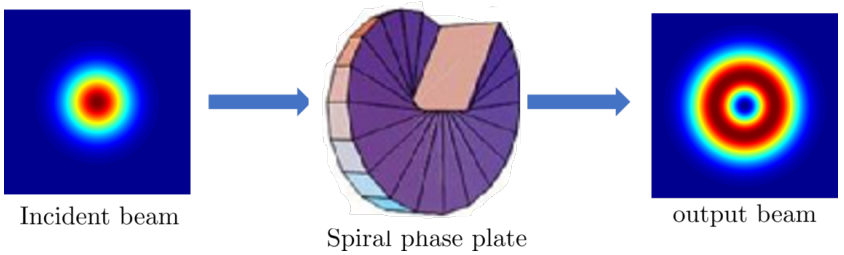


FIGURE 1.12: Dynamic phase modulation using a spiral phase plate. The plate causes an azimuthally varying phase which results in a beam having a helically twisted wavefront.

This concept has been exploited in liquid crystal technology in the form of spatial light modulators (SLM) to locally vary the refractive index rather than the depth, but again resulting in a spatially varying dynamic phase [43].

Recently, it has been discovered that when polarised light propagates through a birefringent medium, it experiences an additional phase component, namely geometric phase [44–46]. This phase, unlike the dynamic one, does not depend on the optical path length, but rather on the geometry (spatial variance) of birefrinegence. Controlling the geometric phase of light is executed by using liquid crystal q-plates and subwavelength gratings [47–53]. It is also possible that light could acquire a geometric phase component if it's excursion through an optical system corresponds to a closed loop [54]. All the above-proposed approaches have been extensively used to structure laser beams external to the cavity. By implementing one or a combination of these approaches, one can have control over light's degrees of freedom.

Although numerous advances have been devised for shaping light outside the laser resonator, structuring light inside the resonator lags behind and is still a growing research field. The laser process explained in section 1.1 implies that structured modes can be directly generated from a resonator if they are eigenmodes [15]. Selecting a particular desired mode can be accomplished by introducing losses to all the undesired modes. In such scenario, a custom optic is inserted into the cavity so that one particular mode has a lower loss than all of the rest. Since the resonator modes must repeat after each round trip, the small loss difference becomes significant after some number of round trips. Accordingly, the mode with the lowest loss is the first to lase.

One example of this approach is to use an amplitude filter, in which a bespoke aperture is inserted inside the cavity to select a mode. For instance, a circular aperture of an appropriate size is used to select a Gaussian beam, while other higher-order modes are clipped and experience higher loss [41, 55–57]. The same technique was exploited to select higher-order modes by placing wires near one of the end mirrors coinciding with the node lines which results in high losses to the Gaussian mode [55]. The amplitude shaping approach is also achieved by introducing gain to a particular mode using pump-shaping thereby selecting a desired spatial gain profile [58].

Phase modulation techniques can also be used to customise the light from laser resonators. This technique can be utilised using three main steps: firstly, specify the desired beam profile at the output coupler (OC); secondly, propagate the beam to the back reflecting mirror, then determine the phase at this mirror; finally, design your back reflector mirror to the conjugate of this phase. In this case the desired beam propagate to the back mirror, acquiring some phase change. After reflecting from the back reflector mirror, the beam acquires the conjugate of the phase it accumulated during the first

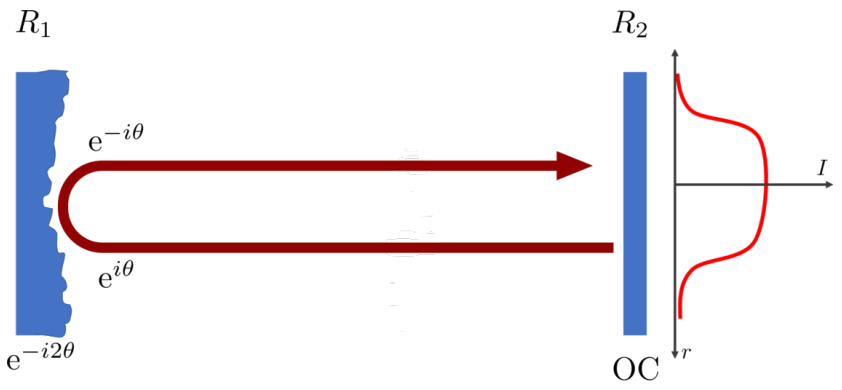


FIGURE 1.13: Schematic diagram illustrates the intra-cavity phase control where a desired flattop beam is selected at the output coupler (OC). The beam is propagated to mirror R_1 where we determine the phase of the beam $e^{i\theta}$. The mirror R_1 is designed to have phase $e^{-2i\theta}$. The reflected beam then carries phase $e^{-i\theta}$. Due to the reciprocity of light, the beam returns back after one round trip to what is was. This process repeats every round trip.

pass. Due to the reciprocity of light, when the beam return to the OC, its phase will unravel to return the beam to what it was [59, 60]. This repeats every round trip and thus the desired mode is now considered as an eigenmode of the resonator. Sometimes the design approach necessitates two custom mirrors rather than one (see [61, 62].

Although all these beam shaping techniques allows intra-cavity generation of many exotic structured modes, there are still some outstanding limitations. The first limitation is the selection of a degenerate mode. For example, $LG_{p,\ell}$ and $LG_{p,-\ell}$ modes have the same wavefront curvature and the same mode losses. This makes it difficult to select one without the other. Breaking the mode degeneracy by selecting a particular degenerate mode without the other one is overcome by using geometric phase elements such as q-plates and subwavelength gratings inside the resonators [63]. The second limitation is the power handling capability of the generation tools which restrains the generation to only low power beams. Subwavelength gratings shows promise to overcome this problem but to which limit, is still an open question.

1.6 Outline

In this chapter, we presented an introduction to the basic theory of optical laser resonators. We discussed the solutions of the optical field inside the resonator from the wave and diffraction perspective. We focused on exploring some of these solutions such as Gaussian and Laguerre Gaussian beams as will be utilised in this thesis. The approach to distinguish these modes by decomposing them into basis modes, known as modal decomposition, was presented. We investigated the general problem of shaping

the laser beams and showed the different approaches that can be exploited to structure exotic modes inside or outside laser resonators.

In Chapter 2 we will demonstrate the first fractal light from canonical unstable resonators. We will observe a variety of fractal shapes in transverse intensity cross-sections through the lowest-loss eigenmodes of unstable laser resonators, thereby demonstrating the controlled generation of a new family of structured light modes with fractal geometry from inside a laser cavity. We will show, quantitatively, that intensity cross-sections are most self-similar in the magnified self-conjugate plane. We will also advance the existing theory of fractal laser modes by showing that imaging and diffraction also occurs in the longitudinal direction, resulting in 3D self-similar fractal structure around the centre of the magnified self-conjugate plane. This work offers a significant advance in the understanding of a fundamental symmetry of Nature as found in lasers.

In Chapter 3 we will present a novel technique for the controlled generation of a family of structured light namely, Higher-Order Poincaré (HOPS) beams from inside the laser resonator by tailoring the geometric phase using metasurfaces. We will demonstrate the generation of pure OAM modes and superpositions thereof. Our laser system will show no limitation on the OAM value that can be created. We will demonstrate the generation of the largest pure OAM state $\ell = 100$ as well as the largest superposition state of net OAM $\ell = 110$. We will show that controlling light's different degrees of freedom such as wavelength, polarisation and azimuthal modes in one resonator is possible.

In Chapter 4, we will argue that traditional quality measurements can not apply for optical vector vortex beams. Over the past years, only qualitative techniques have been applied to these beams to distinguish the scalar and vector modes. However, there are no quantitative techniques that can tell how vector the modes is. In this chapter we will apply a quantum tool to quantify this quintessential property of vector modes, which we will call the vector purity. This tool will allow one to quantify the purity of any HOPS beam on a scale from 0 (pure scalar modes) to 1 (pure vector modes). We will demonstrate this tool on a variety of HOPS beams in a continuous range from purely scalar to purely vector to show the agreement between the experiment and theory.

In Chapter 5 we will highlight the need for high power HOPS beams in many applications. We will extensively study the question of how the purity of vector beams change under amplification. In this chapter we will employ a master-oscillator-power-amplifier (MOPA) approach and study the problem of purity of HOPS beams through non-birefringent and birefringent amplifiers. We will provide the theory and measurement toolbox for practical use and confirm its validity experimentally. Intriguingly, we will show that pure VV beams can maintain their vector purity regardless of the gain

medium, while general VV beams can have their purity improved by using a suitable birefringent amplifier.

Chapter 2

Fractal Light from Lasers

Fractals, complex shapes with structure at multiple scales, have long been observed in Nature: as symmetric fractals in plants and sea shells, and as statistical fractals in clouds, mountains and coastlines. More recently they have been theorised to exist as two-dimensional (2D) transverse structure in the modes of unstable laser resonators, but experimental verification has remained elusive. Here we observe a variety of fractal shapes in transverse intensity cross-sections through the lowest-loss eigenmodes of unstable laser resonators, thereby demonstrating the controlled generation of a new family of structured light modes with fractal geometry inside a laser cavity. We also advance the existing theory of fractal laser modes, first by predicting 3D self-similar fractal structure around the centre of the magnified self-conjugate plane, second by showing, quantitatively, that intensity cross-sections are most self-similar in the magnified self-conjugate plane. Our work offers a significant advance in the understanding of a fundamental symmetry of Nature as found in lasers.

2.1 Introduction

The allure of fractals lies not only in their aesthetic beauty and the mathematical beauty of their self-similarity, but also in that such complexity can be achieved by very simple chaotic equations. Nature seemingly utilises this as an engineering tool, with symmetric fractal structures appearing in many diverse forms, from romanesco broccoli to ammonite sutures and ferns, while statistical fractals are seen in salt flats, mountains, coastlines and clouds. Popularised by Benoit Mandelbrot [64], fractals can be thought of the the mathematical instance of "plus ca change, plus c'est la meme chose" ("the more things change, the more they stay the same").

Light can be fractal. The (dark) vortex lines in random light fields have fractal scaling properties [65], and light's spatial (and spectral [66]) distribution can be directly made fractal by interaction with a fractal object, for example by emitting it from a fractal antenna [67], by passing it through a fractal aperture [68, 69], or by resonating it in a cavity that contains a fractal scatterer [70]. Perhaps more surprisingly, due to the fractal Talbot effect the light field behind a (non-fractal) Ronchi grating illuminated by a uniform plane wave evolves, on propagation, into a fractal [71, 72].

A glance at intensity cross-sections through the eigenmodes of unstable canonical resonators (e.g. [16]) reveals complex and fractal-looking structure, but the first suggestion that these eigenmodes are fractals came only in 1998 [73, 74]. This is surprising, as canonical resonators are very simple, consisting of a pair of spherical mirrors and any apertures in the resonator. Initially, the discussion of the mechanism involved mostly the round-trip magnification due to geometrical imaging by the spherical mirrors, which leads to similar patterns to appear at a cascade of different length scales, one of the hallmarks of fractals, but it also hinted at the role of diffraction, which gives rise to the ripples in the pattern in the first place [75]. Clearly, without diffraction, successive magnifications would simply make any initial pattern increasingly uniform. Detailed theoretical studies of these intensity distributions found them to be statistical fractals [72–79]. Upon magnification, statistical fractals look like the same *type* of pattern, but not actually the same pattern. Like in all physical fractals, the range of length scales over which this scaling behaviour holds (the scaling range) is limited [80], here by diffraction. After magnification, a part of a self-similar pattern looks not just to be the same pattern type as a corresponding, unscaled, part the pattern, but *the same*. Note that, with all physical fractals, this is only true over a finite range of sizes, here limited by the smallest size allowed by diffraction and the overall size of the beam. Suitable choice of the resonator parameters has been predicted to lead to intensity distributions closely related to classic fractals such as the Weierstrass-Mandelbrot function, the Sierpinski gasket, and the Koch snowflake [81, 82].

Despite these early advances, experimental observations have been scarce. A pulse of light was injected into a passive canonical cavity and observed to evolve over a number of round trips into a fractal pattern [83]; curiously, that work was never published in a peer-reviewed journal. Very recently, small areas containing fractal structure were found in the eigenmode of a non-canonical resonator comprising an array of microspheres sandwiched between planar mirrors [84] — the first observation of fractal structure in the eigenmode of an (active) laser. These are the works that are most relevant to this study, but the relevance is limited as they either worked in a passive cavity and did not study the eigenmode in the magnified self-conjugate plane [83], or in a different laser configuration altogether [84]. Further, the discussion was entirely limited to the light structure in transverse planes, resulting in what we will refer to as 2D fractals[1]

2.2 Transverse Fractals

We start by reviewing the mechanism that leads to self-similar fractal structure at the self-conjugate plane in an unstable canonical resonator. Without loss of generality, we restrict ourselves to confocal resonators, as these are particularly simple but at the same time representative of all canonical unstable resonators (with the same round-trip magnification, M, and the same Fresnel number [16]).

Consider the example shown in Fig. 2.1. In such a resonator, each mirror is spherical and hence it images like a lens, but in reflection. During one round trip, i.e. reflection off both mirrors, the image produced by the first mirror is imaged again by the second mirror. In stable resonators this imaging explains the eigenmodes' structural stability [85]. In unstable canonical resonators, one round trip images two "self-conjugate" planes back to their original positions, one with (transverse) magnification M ($|M| \geq 1$), the other with magnification $1/M$ [81]. The former is the magnified self-conjugate plane, S, the latter the de-magnified self-conjugate plane, s. In a confocal resonator, these planes are a focal distance on either side of the two mirrors (see Fig. 2.1), and so the field in these planes form a Fourier pair. Geometrical imaging stretches, during every round trip through the resonator, the intensity distributions in the planes S and s by a factor M and $1/M$, respectively.

Any apertures in the resonator simply add some diffractive "decoration" to this image. After a number of round trips, the pattern is essentially unchanged between successive round trips (the complex amplitude cross-section is unchanged apart from complex factor

[1] Note that the dimension of the plane is, in general, different from the fractal dimension of such intensity distributions [76].

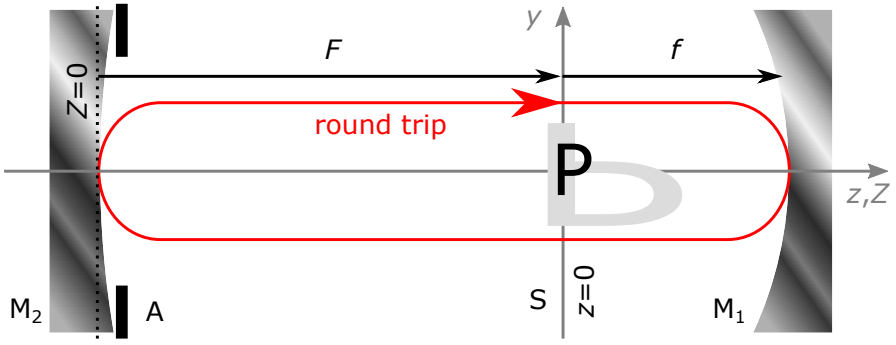


FIGURE 2.1: Imaging inside an unstable canonical resonator. The two spherical mirrors, M_1 (focal length f) and M_2 (focal length F), perform geometric imaging. We define two longitudinal coordinates, z and Z. Both the z and the Z axes coincide with the optical axis, but the $z = 0$ plane coincides with the plane S, the magnified self-conjugate plane, and the $Z = 0$ plane coincides with the plane of the mirror M_2. We use z in our theoretical analysis, Z in the experimental part. The transverse coordinates are x (not shown) and y. Three-dimensional imaging during one round trip is indicated by an object in the shape of the letter "P" (shown in black) and its image, which looks like a horizontally elongated letter "b" (shown in grey): the "P" has turned into a "b" because the transverse magnification, M, is negative, and so the image of the "P" is upside-down; the "b" is horizontally elongated because the longitudinal magnification, M_l, is positive and its magnitude is greater than that of the transverse magnification. A is an aperture immediately in front of M_2. The figure is drawn for a the particularly simple case of a confocal resonator (length $F + f$; the plane S then coincides with the common focal plane) with $M = -2$ and $M_l = +4$.

representing a uniform phase change and loss), which means the field has settled into an eigenmode.

2.3 Resonator Simulations

The simulations of the resonator were performed using our open-source package *Young TIM* [86]. This software represents a transverse cross-section through a monochromatic light beam on a rectangular regular grid of points covering a rectangular area in a transverse plane. At each point, the complex electric field is represented by a complex number u, enabling representation of a the amplitude, which is $|u|$; the phase, which is $\arg(u)$; and the intensity, which is $|u|^2$. For simplicity, the software assumes uniform polarisation across the beam, which is a good approximation in the paraxial limit, in which we operate here. The complexity of the simulation is limited by the memory requirements of calculating a new transverse beam cross-section while storing others.

Propagation from one transverse plane into another through empty space is performed using a standard Fourier algorithm [87] (but without using the Fresnel approximation to simplify the expression for the z component of the wave vector). This algorithm performs

a plane-wave decomposition of the beam, and calculates the sum of all individual plane-wave components in the new transverse plane. Transmission through optical elements such as apertures and lenses is simulated by multiplying the complex numbers that represent the beam by a position-dependent factor that represents a change in amplitude (in the case of apertures), a change in phase (in the case of lenses), or both.

Repeated propagation through a laser resonator is performed by treating each mirror like a lens of the same focal length, and — despite the fact that the propagation direction is reversed by reflection off a mirror — propagating the beam always through a positive distance.

In our case, the lowest-loss eigenmode is reached after approx. 20 round trips. Once the eigenmode has formed, the decoration pattern is the same during successive round trips as shown in Fig. 2.2. Once added, it gets magnified with the rest of the intensity distribution, which results in the presence of the decoration pattern in a number of sizes: the pattern added during the most recent round trip is at the original size; that added during the previous round trip is magnified by M; that added two round trips ago is magnified by M^2; and so on. The presence of a pattern on such a cascade of length scales is a hallmark of self-similarity. The mechanism outlined above is called the monitor-outside-a-monitor effect (MOM effect), named so because of analogies with video feedback [88, 89].

2.4 3D Fractals

For the same resonator, Fig. 2.3 shows a lateral intensity distribution around the centre of the self-conjugate plane S. This lateral intensity distribution shows some signs of self-similarity: if the pattern is stretched by M in the direction representing the transverse direction, and by a factor M^2 in the longitudinal direction, the pattern's centre (which is the point where the plane S intersects the resonator's optical axis) looks similar to what it was before magnification.

This self-similarity can be seen much clearer in Fig. 2.4, which was calculated for a strip resonator, i.e. a resonator that is invariant in one transverse direction. It can therefore be treated as a 2D resonator with only one transverse direction, which means that, along that transverse direction, the light field can be represented in computer simulations by a much greater number of grid points without increasing memory or complexity requirements. This in turn allows an increase in the Fresnel number by increasing the aperture size, resulting in a lateral intensity cross-section with significantly more detail.

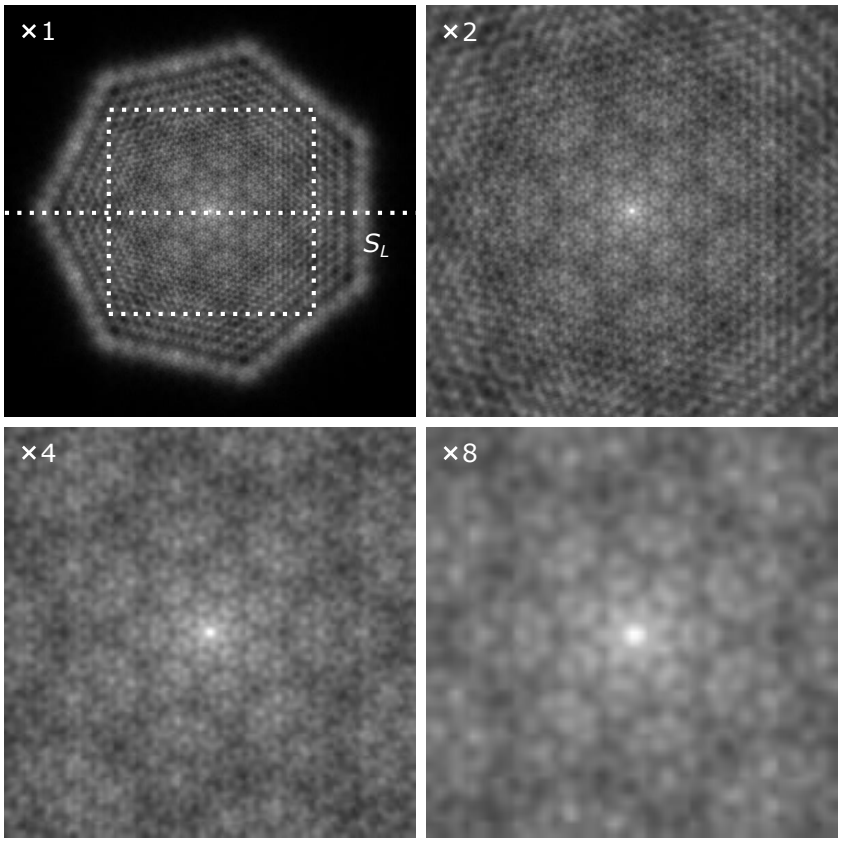


FIGURE 2.2: Self-similarity of the simulated lowest-loss eigenmode's intensity distribution in the magnified self-conjugate plane, S. The frames show the intensity after 20 round trips, starting with a uniform plane wave. The self-similarity of the pattern is demonstrated by showing its centre at different magnifications (×2, ×4, ×8), resulting in a similar pattern (rotated by 180° after each magnification by a factor 2 due to the resonator's transverse magnification, M, being negative); the dotted white square in the centre of the frame marked ×1 shows the outline of the area shown in the next frame. The horizontal dotted line is the orthographic projection of the lateral self-conjugate plane S_L, in which we demonstrate, below (see Fig. 2.3), the 3D self-similarity of the light. The figure is calculated for light of wavelength $\lambda = 632.8\,\text{nm}$ in a resonator of the type shown in Fig. 2.1 with $F = 16.5\,\text{cm}$, $f = 8.25\,\text{cm}$, $M = -2$, and a seven-sided regular polygonal aperture of circumradius $r_0 = 2.4\,\text{mm}$. The beam's transverse cross-sections were represented by a 1024×1024 array of complex numbers sampled over a physical area of size $1\,\text{cm} \times 1\,\text{cm}$. Further details of the way this simulation, and indeed all the other simulations in this chapter, was performed are given in Section 2.3.

For that same strip resonator, Fig. 2.5 compares the intensity cross-sections along the transverse direction in the plane S with that along the resonator's optical axis. The intensity cross-section along the optical axis is not symmetrical with respect to the position of the plane S, whereas that in the plane S is symmetric with respect to the position of the optical axis. Irrespective of this complication, both curves are strikingly self-similar.

This observation can be explained as follows. Spherical mirrors (and lenses) image not only any transverse plane into a corresponding transverse plane, they image any point

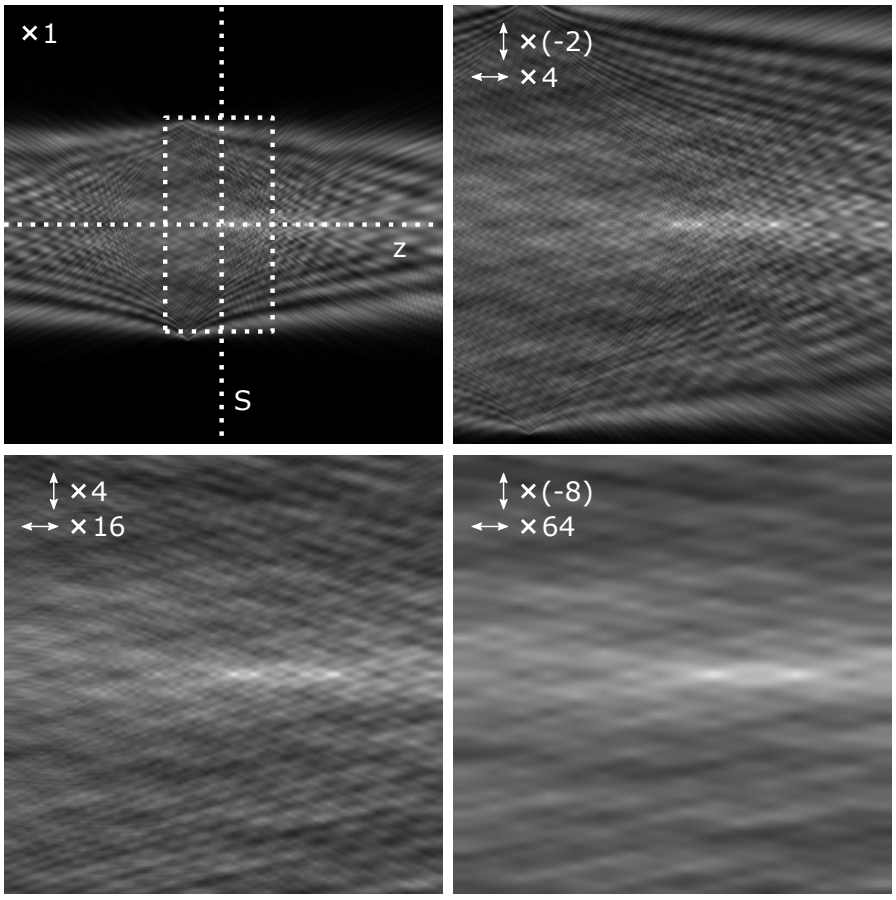


FIGURE 2.3: Self-similarity of the intensity distribution in a lateral self-conjugate plane, S_L, which contains the optical axis and intersects the plane S horizontally in Fig. 2.2. The vertical dotted line is the orthographic projection of the plane S. Vertically, the plots are centred on the optical axis, z. The beam is the same as that shown in Fig. 2.2. After each magnification horizontally by a factor 4 and vertically by -2, the pattern looks similar again, which is shown for different magnifications. The dotted box in the centre of the frame marked $\times 1$ marks the outline of the area shown in the next frame ($\times(-2)$ vertically, $\times 4$ horizontally). The $\times 1$ frame represents a physical area of size 2 m (horizontally) by 10 mm (vertically).

into a corresponding point. For light initially travelling to the right in the resonator shown in Fig. 2.1, any lateral plane that includes the optical axis is being imaged into itself, as is the magnified self-conjugate plane S; no other planes are being imaged into themselves (but other surfaces are, specifically the paraboloids $z = ar^2$, where z and r are cylindrical coordinates as shown in Fig. 2.1 and a is an arbitrary constant). One point is imaged into itself ("self-conjugate point"), namely the intersection of the self-conjugate plane S with the optical axis. The volume around this point is also imaged into itself, but the image is distorted as the longitudinal and transverse magnifications are different (the longitudinal magnification is the square of the transverse magnification) and both change with position. (Similar statements are true for light initially travelling to the left, but we do not consider these here.) Close to the self-conjugate point, the

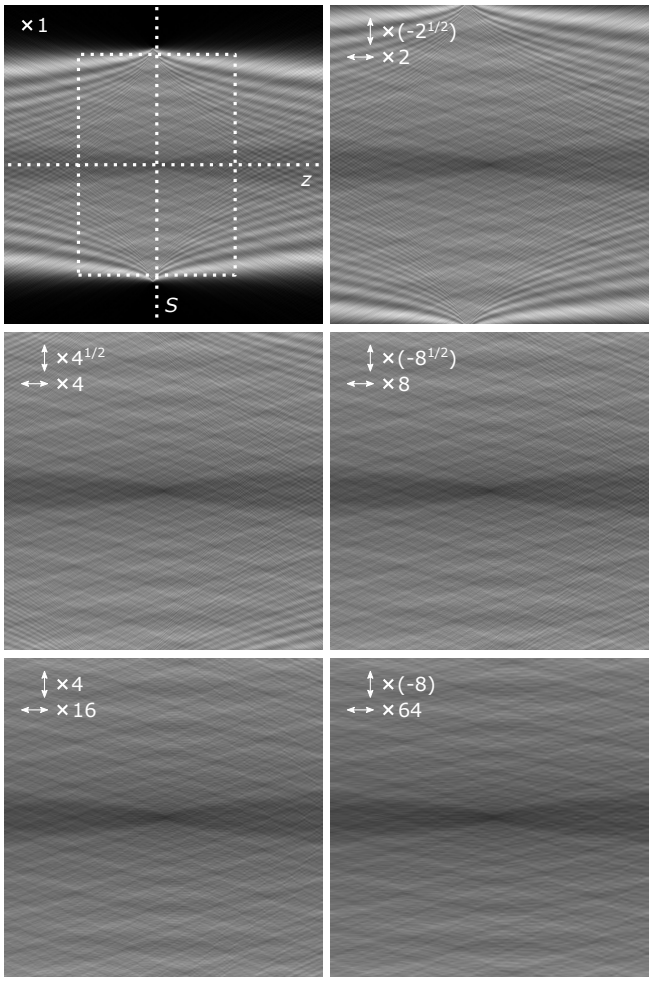


FIGURE 2.4: Self-similarity of the intensity distribution in the lateral plane of a strip resonator of the type shown in Fig. 2.1. The different frames show the centre of the intensity distribution, successively magnified by a factor M in the vertical direction and by M^2 in the horizontal direction. The $\times 1$ frame represents a physical area of size 20 m (horizontally) by 2.82 cm (vertically), centred on the magnified self-conjugate plane and the optical axis in the horizontal and vertical direction, respectively. The dotted box shown in the top left frame outlines the area shown in the top right frame. The figure was calculated for light of wavelength $\lambda = 632.8\,\text{nm}$, resonator parameters $F = 70.7\,\text{cm}$ and $f = 50\,\text{cm}$ (corresponding to transverse magnification $M = -\sqrt{2}$), and the aperture A was a slit of width 2.08 cm. Each beam cross-section was represented on 4096-element array of complex numbers, representing a physical width 4 cm.

longitudinal magnification is constant. This imaging of the volume around the centre of the plane S is indicated in Fig. 2.1.

As before, the effect of any apertures in the system is the addition of a diffractive decoration pattern, which is now 3D. In a 3D extension of the MOM effect, this pattern gets added to the field during each round trip and magnified during each subsequent round trip, again resulting in its presence on a cascade of length scales, complicated and enriched by the different characteristic stretch factors in the longitudinal and transverse directions.

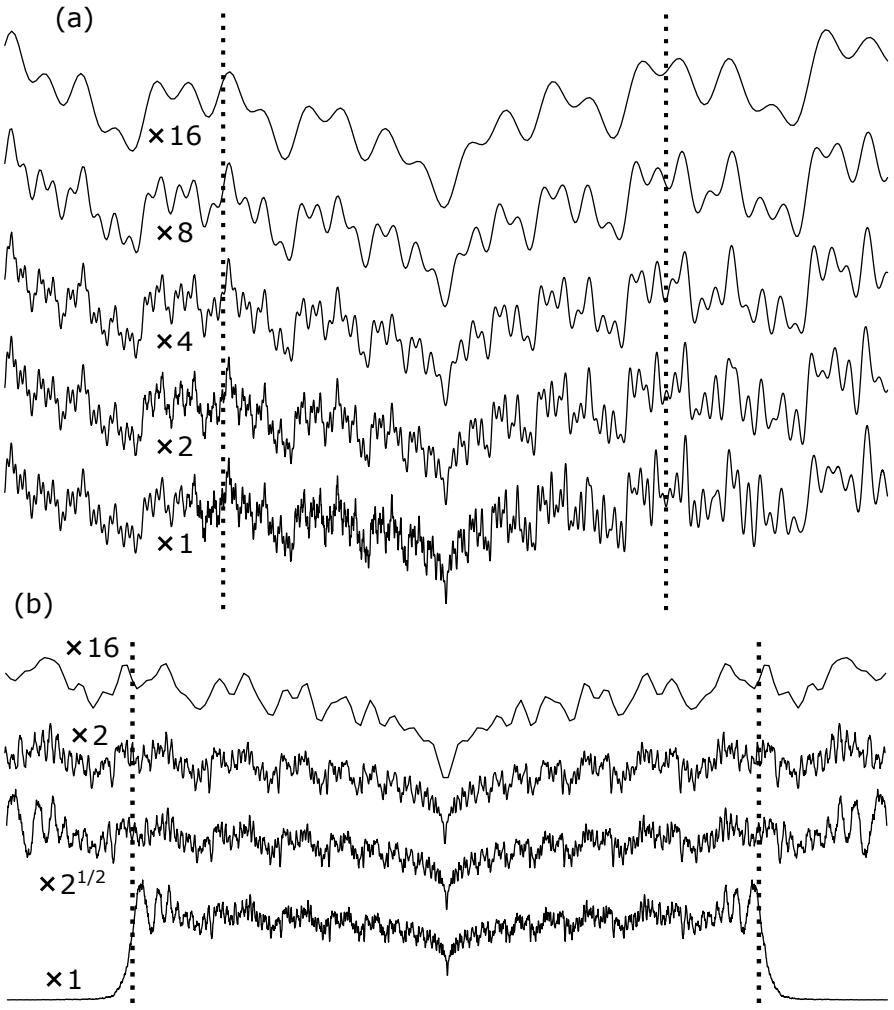


FIGURE 2.5: Axial (a) and transverse (b) intensity cross-section through the field around the self-conjugate point at the centre of the plane S in the strip resonator from Fig. 2.4. Like in Figs. 2.2, 2.3 and 2.4, the self-similarity is demonstrated by successive magnifications, each of which stretches the part of the curve between the vertical dotted lines to the full width. The width of the curves marked $\times 1$ represents a physical length of 2 m (a) and 2.08 cm (b). The intensity range represented by the different curves has been adjusted so that corresponding features in the curves have roughly the same vertical size.

2.5 Self-similarity of Transverse Fractals

The mechanism for the emergence of fractals in the transverse intensity cross-sections, described in section 2.2, suggests that the cross section is most self-similar in the magnified self-conjugate plane, but this has never been tested quantitatively.

Here we provide the first quantitative evidence for this argument. For the intensity cross-section in one transverse plane at a time we calculate the normalised squared Euclidean distance, d^2, between the centre of this intensity cross-section and the centre of the same intensity cross-section, stretched by a factor M. This is a measure of the

difference between the stretched and unstretched centre of the intensity cross-section, and $-d^2$ is therefore a measure of their similarity. If the two intensity distributions are $I_1(x_i, y_j)$ and $I_2(x_i, y_j)$, d^2 is defined as

$$d^2 = \frac{1}{2} \frac{\left|(I_1 - \overline{I_1}) - (I_2 - \overline{I_2})\right|^2}{\left|I_1 - \overline{I_1}\right|^2 + \left|I_2 - \overline{I_2}\right|^2}, \tag{2.1}$$

where $|I|^2 = \sum_{i,j} I(x_i, y_j)^2$, $\overline{I} = (\sum_{i,j} I(x_i, y_j))/(N_x N_y)$, and where all sums are over N_x by N_y values of x_i and y_j.

In all cases, the unstretched intensity distribution, I_1, was known on a discrete grid of points, and it was required to calculate the stretched (by a factor M, the transverse magnification) intensity distribution, I_2, on the same grid. For a particular grid position (x_i, y_j) we calculated the value of the stretched intensity distribution there as

$$I_2(x_i, y_j) = I_1(x_i/M, y_j/M), \tag{2.2}$$

whereby the stretching is relative to the origin. In general, the position $(x_i/M, y_j/M)$ does not coincide with one of the grid positions on which the unstretched intensity distribution was known; we used bilinear interpolation between the intensity at the four neighbouring represented positions [90] to approximate this value.

It is clear that stretching the unstretched and stretched intensity distributions are not similar far away from the centre, where the unstretched intensity is close to zero (compare, for example, the frames marked "×1" and "×2" in Fig. 2.2). For this reason, we sum only over the centre of each pattern, specifically the central rectangle of width and height 1/4 of the width and/or height of the area on which the unstretched intensity cross-section is represented.

We plot $-d^2$ as a function of the z coordinate of the transverse plane, defined as the Cartesian coordinate aligned with the optical axis such that the plane $z = 0$ is the magnified self-conjugate plane (Fig. 2.1). From the above argument we expect a peak at $z = 0$, that is, in the magnified self-conjugate plane S.

Figure 2.6 shows these curves, calculated for the two eigenmodes discussed earlier, namely that of a resonator with a heptagonal aperture and transverse magnification $M = -3$ (Figs. 2.2 and 2.3), and that of a strip resonator with transverse magnification $M = -\sqrt{2}$ (Figs. 2.4 and 2.5). The expected peak at $z = 0$ is clearly visible and, especially in the case of the strip resonator, reaches close to $d^2 = 0$, proving the near-exact — but diffraction-limited — self-similarity of the intensity cross-section in the magnified self-conjugate plane.

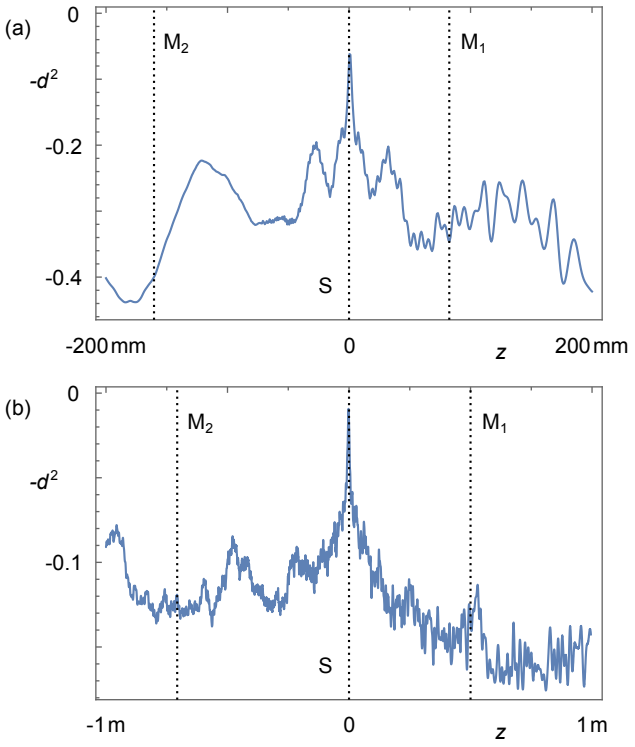


FIGURE 2.6: Evolution of the self-similarity of transverse intensity cross-sections upon propagation for the eigenmodes shown in Figs. 2.2 and 2.3 (a) and in Figs. 2.4 and 2.5 (b). The self-similarity is quantified here by $-d^2$, the negative of the normalised squared Euclidean distance between the central rectangle of the intensity cross-section in the transverse plane with the given z coordinate, and the central rectangle of the same size of the intensity cross-section after being stretched in the transverse directions by a factor M. The magnification was $M = -3$ in (a) and $M = -2$ in (b). The width and height of the central rectangle were arbitrarily chosen to be 1/4 of the width and height of the calculated intensity cross-section. The dotted vertical lines indicate the planes of the mirrors, M_1 and M_2, and the magnified self-conjugate plane, S.

Note that these results can be replicated with other measures of difference between images, and we did this with Euclidean distance and image Euclidean distance [91] (IMED, which we calculated only for the strip-resonator eigenmode). These gave a curve with a different shape to those shown in Fig. 2.6, but always produced a very prominent peak in the magnified self-conjugate plane.

2.6 Experiment

We constructed a laser, sketched in Fig. 2.7, consisting of a flash-lamp pumped Nd:YAG gain medium (6.35 mm × 76 mm) inside an L-shaped, confocal, unstable cavity comprising two concave, high-reflectivity, spherical end mirrors, M_1 and M_2, and a 45° output coupler positioned at the apex of the L. The radius of curvature of mirror M_1 is R_1, that of M_2 is R_2; their focal lengths are respectively $f = R_1/2$ and $F = R_2/2$. As the cavity

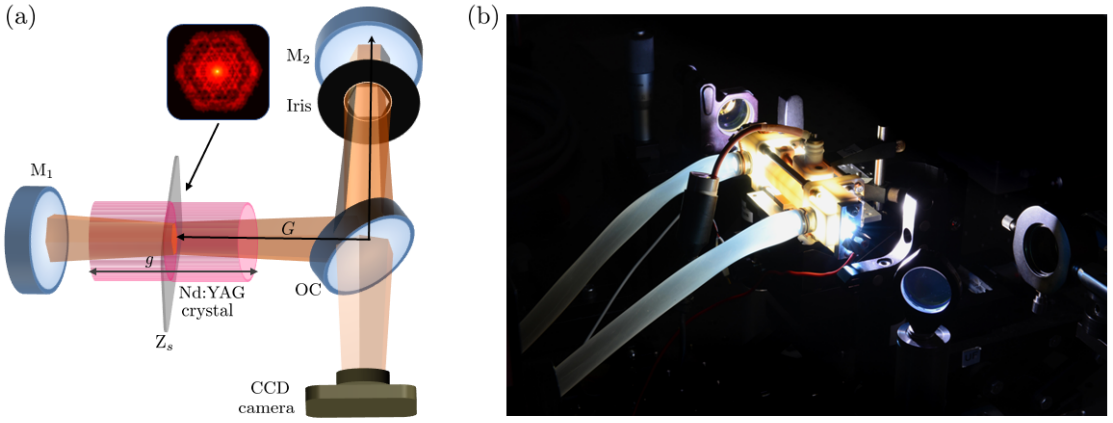


FIGURE 2.7: Experimental setup, (a) schematic and (b) photo with the laser running. (a) The cavity comprised two concave mirrors, M_1 (radius of curvature R_1, corresponding to focal length $f = R_1/2$) and M_2 (radius of curvature R_2, focal length $F = R_2/2$), and an output coupler (OC) angled at 45° with a 99.8% reflectivity. The geometrical length of the cavity was G, that of the Nd:YAG gain medium was g. S is the magnified self-conjugate plane. One out of a variety of polygonal apertures was positioned in front of M_2. The intensity cross-section in the self-conjugate plane S was captured outside the cavity at a distance $R_2/2$ from M_2 using a CCD camera. (b) Clearly visible is the gain-medium assembly (bright yellow; centre) and the mounts for the end mirrors and the output coupler. The two tubes (light blue; bottom left) connecting to the gain-medium assembly are cooling tubes for the gain medium.

is confocal (the cavity was set up to have length $f + F$), the plane S coincides with the common focal plane. In order to minimise unwanted aperture effects, the gain medium was centred on S. An aperture in the shape of a regular hexagon was positioned in front of the end mirror with the greater focal length, M_2.

Like that sketched in Fig. 2.1, our cavity is canonical and unstable, and as such it contains magnified and de-magnified self-conjugate planes. Unlike that sketched in Fig.2.1, our cavity was not confocal, and so the positions of the self-conjugate planes did not simply coincide with the focal planes, but their Z coordinate was calculated from the geometric-imaging properties of the cavity. The output beam was captured using a CCD camera (Spiricon SPU260 BeamGage), placed in an image plane of S. Note that, in apertured lasers (like ours), the field depends on the propagation direction [92], and the camera has been placed to record the image in the magnified self-conjugate plane, S, not the de-magnified self-conjugate plane, s, which corresponds to the opposite propagation direction.

One of the intensity cross-sections observed in the magnified self-conjugate plane is shown as part of Fig. 2.7 (a). It has the expected complex structure characteristic of a fractal. In almost all images we note an unexpectedly bright central intensity peak. We speculate that it is due to a low divergence mode that is also able to lase in the cavity.

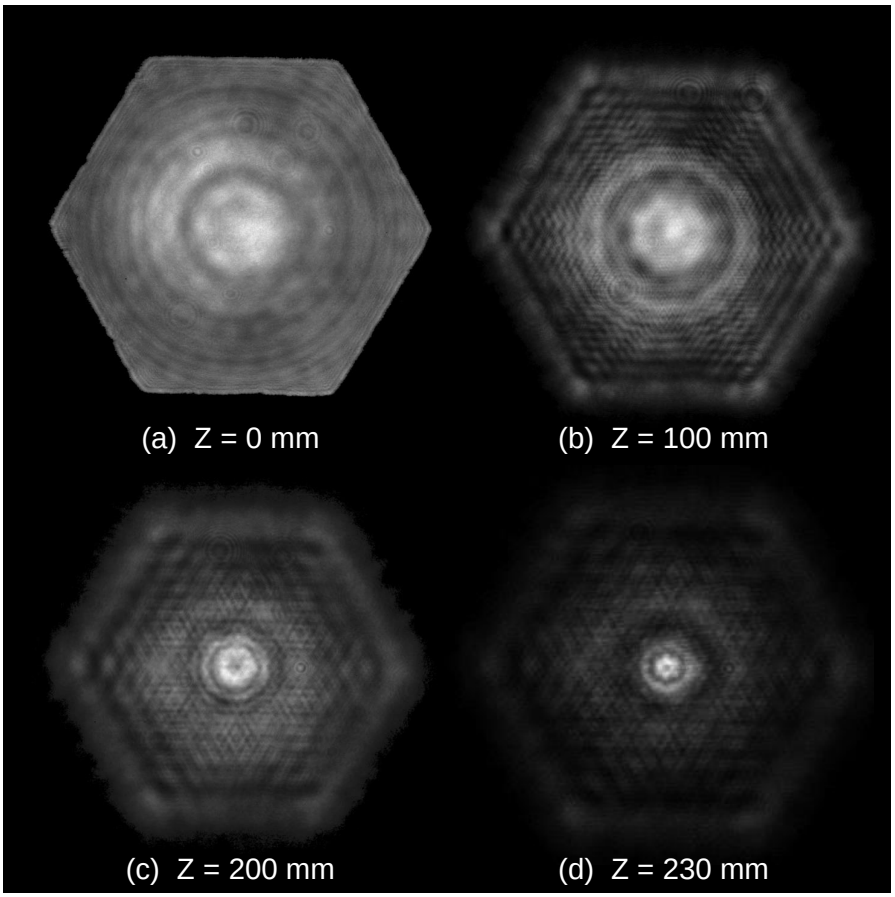


FIGURE 2.8: A few of the transverse intensity patterns recorded inside a resonator for parameters $F = 250\,\text{mm}$, $f = 75\,\text{mm}$, and $G = 343\,\text{mm}$. The self-conjugate plane S is positioned at $Z = Z_S = 231.8\,\text{mm}$.

For one set of parameters, namely $F = 250\,\text{mm}$, $f = 75\,\text{mm}$, $G = 343\,\text{mm}$, and a hexagonal aperture A of circumradius $r_0 = 2.5\,\text{mm}$ we recorded intensity cross-sections in a number of transverse planes across the resonator (see Sec. 2.8), with examples shown in Fig. 2.8. The magnified self-conjugate plane is located at $Z_S = 231.8\,\text{mm}$ (calculated using Eqn [2.11]), the round-trip transverse magnification is $M = -3.32$ (calculated from Eqn [2.12]).

Figure 2.9 allows visual assessment of the self-similarity of the intensity cross-sections recorded in three transverse planes near the self-conjugate plane S. When stretched by the transverse magnification M, the centers of the intensity cross-sections show some similarity to the unstretched intensity cross-sections; for example, dark, centered, hexagons or circles of approximately the same size are present in the stretched and unstretched intensity cross-sections, especially in the planes $Z = 230\,\text{mm}$ and $Z = 240\,\text{mm}$, which are closest to the self-conjugate plane S.

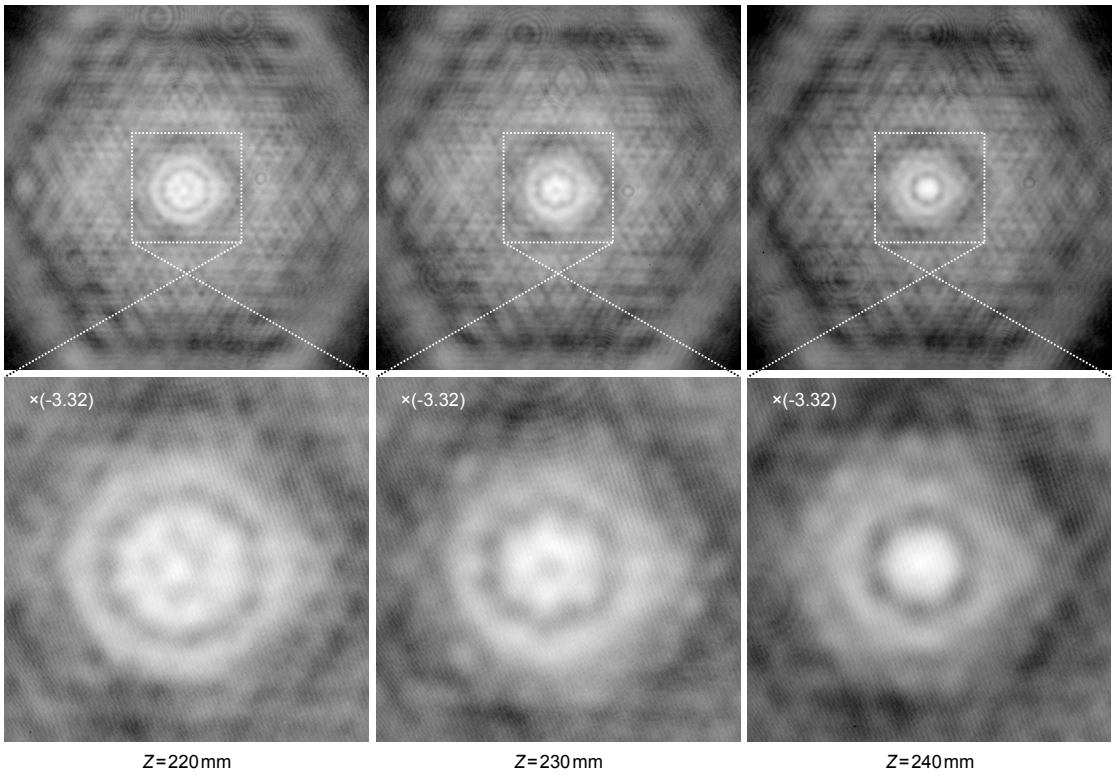


FIGURE 2.9: Self-similarity of the intensity cross-sections in different transverse planes near the predicted position of the self-conjugate plane, $Z = Z_S = 231.8\,\text{mm}$. The images in the top row show the central $\approx 4\,\text{mm} \times 4\,\text{mm}$ of the experimentally recorded intensity cross-sections in the transverse planes $Z = 220\,\text{mm}$ (left), $Z = 230\,\text{mm}$ (center), and $Z = 240\,\text{mm}$ (right). The images in the bottom row show the centers of the corresponding top-row images, stretched by a factor $M = -3.32$, that is, stretched by a factor 3.32 and rotated by 180°. To show structure over a wider intensity range, the brightness of each pixel is proportional to the logarithm of the recorded intensity.

We analysed the recorded intensity cross-sections quantitatively by evaluating their self-similarity and plotting the evolution of this self-similarity upon propagation — the experimental analog to the curves shown in Fig. 2.6. The result is shown in Fig. 2.10. The mirror planes are in no way special, which was also the case in the plot calculated from simulated data (Fig. 2.6). The self-similarity is greatest around the expected position of the plane S, but the sharp peak visible in the curves shown in Fig. 2.6 is absent. One possible explanation for the absence of this peak is that, due to the theoretical sharpness of the peak (Fig. 2.6), we did not record the intensity in a plane close enough to S despite sampling a plane only 1.8 mm from S. Another possible explanation is that the lack of the sharp peak is caused by experimental imperfections. One type of such experimental imperfections, including thermal effects and errors on mirror curvatures and distances, could have resulted in S being located further than expected from the nearest plane that was sampled. Another type, experimental imaging imperfections, most likely due to the effect of the gain medium (which images only in the paraxial limit), could have led to fine detail in the intensity cross-section missing.

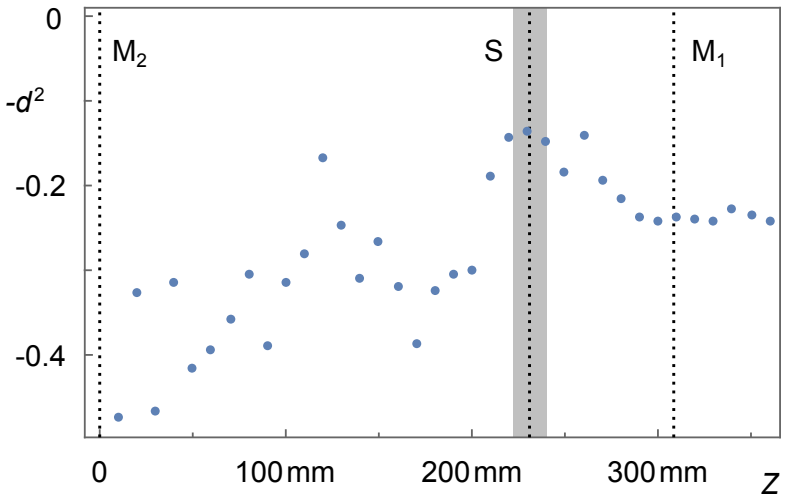


FIGURE 2.10: Evolution of the self-similarity upon propagation of measured transverse intensity cross-sections. Like in Fig. 2.6, the plot shows the negative normalised squared Euclidean distance, $-d^2$, as a function of axial coordinate Z. The predicted position of the self-conjugate plane S, $Z = Z_S = 231.8\,\text{mm}$, is indicated by a dotted black line surrounded by a grey area representing experimental uncertainties. The planes of the mirrors, M_1 and M_2, and the self-conjugate plane, S, are indicated by vertical dotted lines.

Finally, we investigated the generation of these fractal modes in several laser resonator configurations of differing magnification factors and Fresnel number, as detailed in Table 2.1, with the results shown in Fig. 2.11. Most of the lasers had hexagonal apertures, but we also experimented with an aperture in the shape of the 3rd iteration of the Koch-snowflake, a shape approximating a fractal. We do not analyse the intensity cross-sections in the laser with the Koch-snowflake aperture in any detail here, but note that it is not surprising that the resulting diffraction patterns are fractals [93] as there are *several* mechanisms[2] at work that all simultaneously shape the eigenmode intensity cross-sections into fractals.

TABLE 2.1: Resonator parameters used to design fractal cavities of various magnifications.

	Cavity 1	Cavity 2	Cavity 3	Cavity 4
R_1	200 mm	200 mm	150 mm	100 mm
R_2	400 mm	500 mm	500 mm	500 mm
M	2.0	2.5	3.3	5.0

[2]Here there are two mechanisms, specifically the MOM effect and diffraction behind a fractal aperture. This could easily be extended to *three* by periodically repeating the fractal aperture shape across the aperture plane, thereby adding the fractal Talbot effect [71] to the mix.

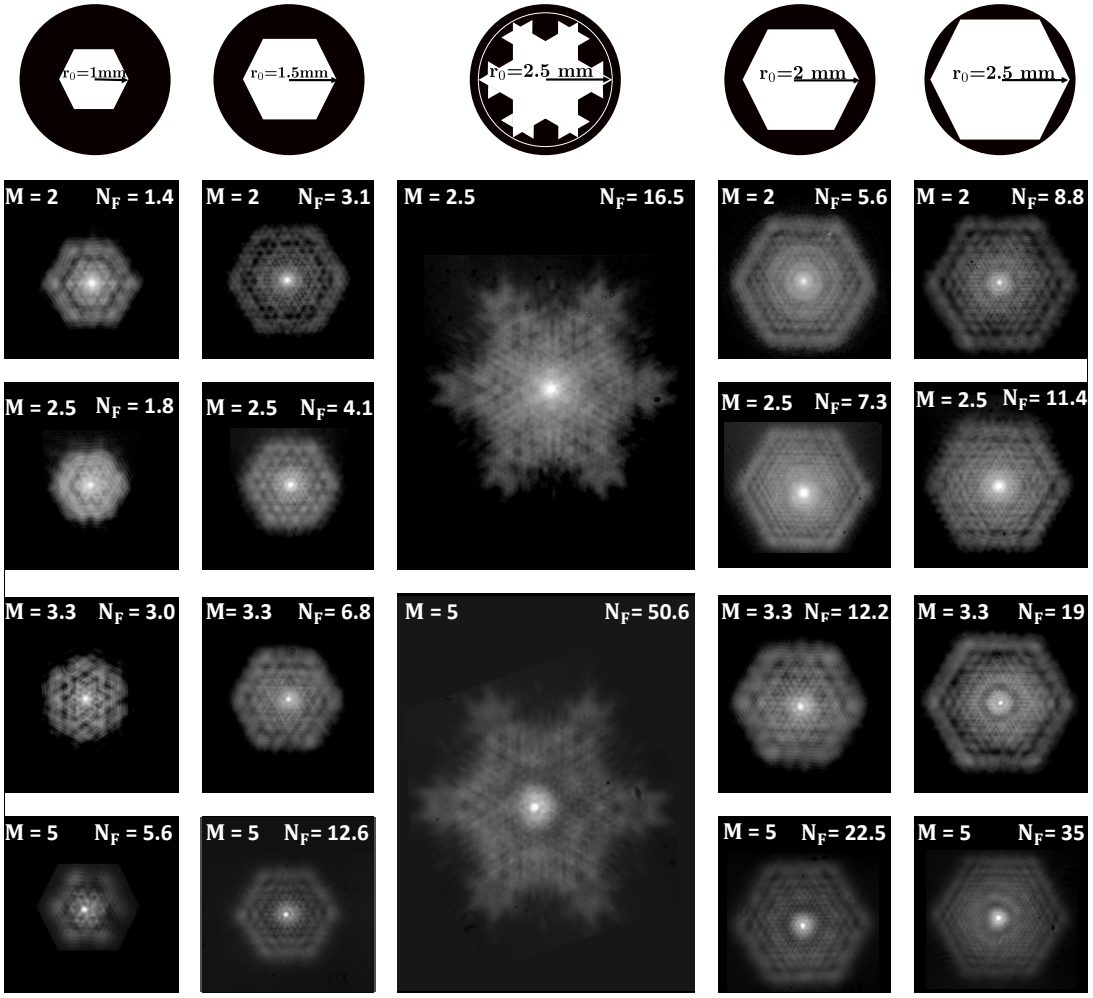


FIGURE 2.11: Collage of experimentally obtained intensity cross-sections measured close to the self-conjugate plane S inside a variety of laser cavities. The edge of the aperture in the central column is that of the 3rd iteration of the Koch snowflake (the first iteration being an equilateral triangle), the other apertures are regular hexagons. r_0 is the circumradius of the apertures, M is the approximate transverse round-trip magnification, and N_F is the Fresnel number. Like in Fig. 2.9, brightness is proportional to the logarithm of intensity.

2.7 Calculation of the Parameters of the Magnified Self-conjugate Plane

Here we calculate the Z coordinate of the magnified self-conjugate plane S, Z_S, and the transverse round-trip magnification, M, for the non-confocal cavities used in our experiment.

Our cavities contain a gain medium with refractive index n and geometrical length g. When seen from a paraxial direction, this gain medium *appears* to be of length g/n, so it appears to be a distance $g - g/n$ shorter than it actually is. The cavity itself therefore appears to be shorter by the same distance, so the presence of the gain medium has the

effect that the cavity has an effective length

$$L = G - \left(g - \frac{g}{n}\right) = G - \left(1 - \frac{1}{n}\right) g. \tag{2.3}$$

From now on, all lengths considered are effective (that is, apparent) lengths.

To calculate the position of the plane S, we consider successive imaging of the self-conjugate plane S due to mirror M_1 and due to mirror M_2. Imaging of S by M_1 into the intermediate image plane $Z = Z_i$ follows the equation

$$\frac{1}{L - Z_S} + \frac{1}{L - Z_i} = \frac{1}{f}, \tag{2.4}$$

where $L - Z_S$ and $L - Z_i$ are the object and image distances, respectively; the transverse magnification is

$$M_{T,1} = -\frac{L - Z_i}{L - Z_S}. \tag{2.5}$$

Similarly, M_2 images the intermediate image plane to the final image plane $Z = Z_f$ according to the equation

$$\frac{1}{Z_i} + \frac{1}{Z_f} = \frac{1}{F} \tag{2.6}$$

with transverse magnification

$$M_{T,2} = -\frac{Z_f}{Z_i}. \tag{2.7}$$

The overall transverse magnification of the final image is then

$$M = M_{T,1} M_{T,2}. \tag{2.8}$$

As it is conjugate to itself, the image of S must be in the plane S again, and so

$$Z_f = Z_S. \tag{2.9}$$

It is straightforward to show that, in the confocal case ($L = F + f$),

$$Z_S = F, \quad M = -\frac{F}{f}. \tag{2.10}$$

In the non-confocal case,

$$Z_S = \frac{2fL - L^2 + \sqrt{d}}{2(f + F - L)}. \tag{2.11}$$

and

$$M = \frac{2fF}{2fF - 2fL - 2FL + L^2 + \sqrt{d}}, \tag{2.12}$$

where

$$d = L(L - 2f)(L - 2F)(L - 2f - 2F). \tag{2.13}$$

2.8 Evolution of the Intensity Distribution over the Length of the Resonator

Fig. 2.12 shows measured intensity cross-sections in a number of transverse planes in the resonator. The self-conjugate plane S corresponds to $Z \approx 231.8\,\text{mm}$, the mirrors were located at $Z = 0$ and $Z = 325\,\text{mm}$.

2.9 Discussion and Conclusion

When not considered in the context of resonators, the existence of 3D self-similar fractal light fields is surprising: the 3D intensity distribution of any light field is fully determined by any transverse cross-section, and so the lowest-loss eigenmode is fully determined by its cross-section in the magnified self-conjugate plane. The existence of self-similar transverse cross-sections whose corresponding beams — their 3D diffraction patterns — are also self-similar is far from obvious. While we have attempted to observe this the experimental requirements on imaging is at present prohibitive. In the 2D case, we have been able to confirm the emergence of fractal light from carefully constructed lasers. We have shown experimentally that fractals can be created directly from such laser cavities, confirming a theoretical prediction of some decades. While the experimental confirmation of 2D fractals reported here concludes an open question in the community, the extension of the theory to 3D opens new exciting avenues for further exploration.

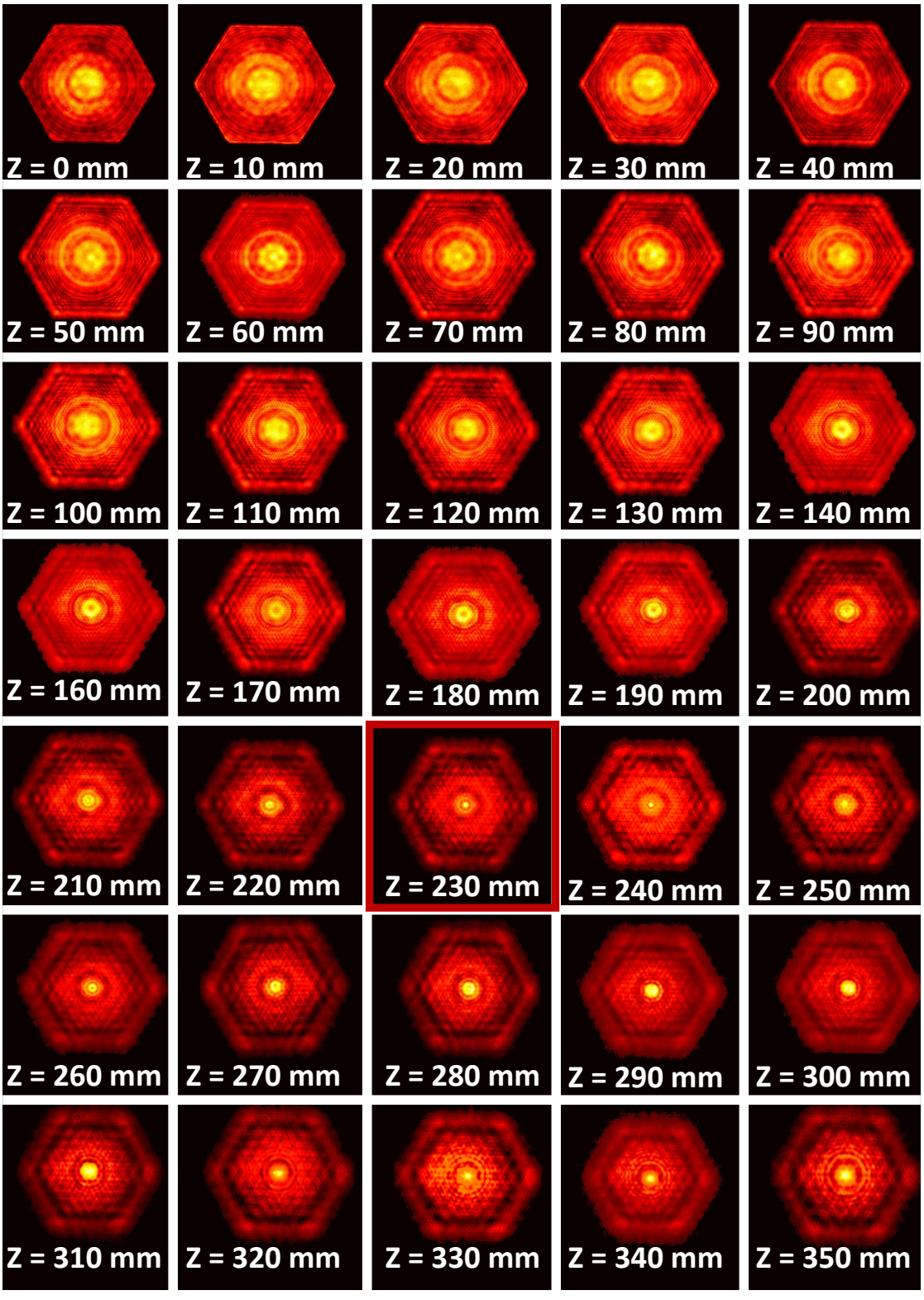


FIGURE 2.12: Evolution of the eigenmode intensity cross-section between mirrors M_2 ($Z = 0\,\text{mm}$) and M_1 ($Z = 350\,\text{mm}$). The magnification was $M = 3.32$ ($F = 250$ mm, $f = 75\,\text{mm}$) with an aperture of circumradius $r_0 = 2\,\text{mm}$. The geometrical length of the cavity was $G = 350\,\text{mm}$, corresponding to an effective length of $L = 308.5\,\text{mm}$ due to the refractive index of the gain medium.

Chapter 3

Higher-Order Poincaré Beams from Lasers

Laser modes with spatially inhomogeneous polarisation and orbital angular momentum (OAM) states, so-called vector vortex beams are highly topical of late[94]. These beams can be mapped over the Higher-Order Poincaré Sphere (HOPS), as shown in Fig. 3.1 (a). The poles of the HOPS represent scalar beams of homogeneously polarised OAM modes, while the equator describes the cylindrical vector vortex modes. The latter are beams with cylindrical symmetry in polarisation and can be decomposed into two vortex beams of opposite handedness and orthogonal polarisation, left and right circularly polarised. More recently, the concept of the HOPS has been extended to represent a general form of vector beams, namely hybrid vector vortex beams with states of polarisation consisting of linear, elliptical and circular polarisation, i.e. spatial variant polarisation states [95, 96]. Such beams are represented by the Generalised HOPS as shown in Fig. 3.1(b).

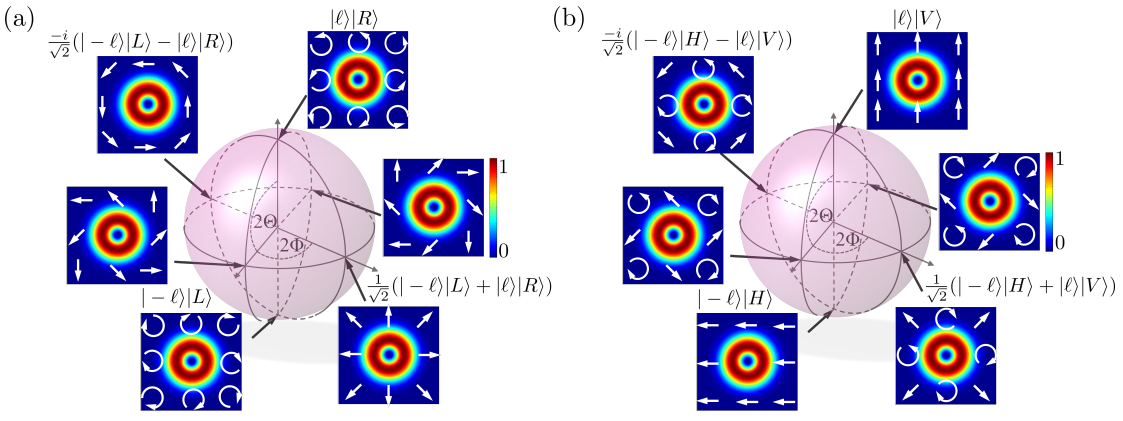


FIGURE 3.1: Illustration of (a) a HOPS representing vector vortex modes in the left and right polarisation basis and (b) a Generalised HOPS representing the vector vortex modes in the horizontal and vertical basis. The output beam profile is displayed at different positions on the sphere with arrows indicating polarisation distribution.

Many advances have been achieved to create and manipulate HOPS beams. Generally, these techniques rely on introducing a phase singularity in the wavefront so as to generate beams with desired OAM. This can be experimentally realised by coherently interfering two orthogonally polarised OAM modes of different azimuthal orders [97, 98] which are produced using dynamic phase manipulation approaches [43, 99–101]. These methods did not consider the possible interaction between polarisation and phase which are believed to be two relatively independent degrees of freedom that show little interaction. Nevertheless, under specific conditions, polarisation also enables manipulation of optical OAM through spin-to-orbital-conversion (SOC) which can be achieved using spatially distributed polarisation converters to introduce a geometric phase, which is also called Pancharatnam-Berry phase [46, 102–104]. These SOC techniques allowed the generation of HOPS using patterned liquid crystal elements (q-plates) and subwavelength gratings (metasurface phase elements) [47–49, 105–110].

Recently, HOPS beams were generated in a controlled fashion inside the laser cavity by inserting a q-plate to convert circularly polarised Gaussian modes into OAM modes and vice verse, assisting with a quarter-wave plate for polarisation control [63]. More recently, subwavelength metasurface gratings have been implemented inside lasers for the generation of HOPS beams. This necessitated physically changing the resonator design for the generation of different HOPS beams. Yet, this generation technique was mostly limited to low order HOPS beams with maximum OAM $\ell = \pm 3$ [111, 112].

These previous methods suffer from two inherent limitations. Firstly, the output HOPS beam can not possess arbitrary paired OAM states. They are constrained to being conjugate OAM values ($\pm\ell$) of each other. Secondly, they are limited to only using circular polarisation as the control for the generation of pure OAM states, only two of an infinite set of possible polarisation states [113].

In this chapter, we demonstrate intra-cavity selection of HOPS beams by implementing, for the first time, an approach for polarisation controlled OAM generation from arbitrary polarisation states. We show that with the aid of a metamaterial geometric phase plate, called a J-plate, we generated pure OAM ($\mathrm{LG}_{0,\ell}$) beams with OAM as high as $\ell = 100$ from inside the laser. Experimental selection of conjugate and hybrid OAM states are presented here for different HOPS.

3.1 Metasurface J-plate for Intra-cavity Conversion of Arbitrary Polarisation to OAM States

The metasurface J-plate device used in the laser cavity is a dielectric metasurface made of amorphous TiO_2 nano-posts with rectangular shape on a quartz substrate. Each post has a height of 600 nm while width and length change in order to impart a different phase delay to the propagating visible light at 532nm [114]. Through it's subwavelength structure, the J-plate enables substantial geometric phase manipulation of light by allowing the transformation of any polarisation to generate arbitrary paired OAM states. There is no restriction on the input polarisation state or the output OAM states of the J-plate. This is in contrast to q-plates, which are only sensitive to circular polarisation for the generation of pure conjugate OAM. Accordingly, the J-plate assigns OAM to the transmitted light based on the polarisation incident on it[113].

The J-plate action can be described in terms of Jones matrix in the linear basis [113] as

$$\mathrm{J} = \begin{pmatrix} \exp(i\ell_1\phi) & 0 \\ 0 & \exp(i\ell_2\phi) \end{pmatrix}, \tag{3.1}$$

where ℓ_1 and ℓ_2 are two independent OAM values that are acquired by different input polarisation states, ϕ is the azimuthal angle. Incident horizontal polarisation, $|H\rangle = \begin{bmatrix} 0 \\ 1 \end{bmatrix}$, then gains the helical phase $\exp(i\ell_1\phi)$, resulting OAM of $\ell_1\hbar$ per photon. Similarly, vertical polarisation, $|V\rangle = \begin{bmatrix} 1 \\ 0 \end{bmatrix}$, then acquires the helical phase $\exp(i\ell_2\phi)$, resulting OAM of $\ell_2\hbar$ per photon.

Let's consider the most general case that the input polarisation $|u_{\mathrm{in}}\rangle$ can be any polarisation state which is neither $|H\rangle$ or $|V\rangle$ but can be composed of both polarisation. since these two polarisation are orthogonal, i.e. $\langle H|V\rangle = 0$, then the output state $|u_{\mathrm{out}}\rangle$ can be given, from Eq.3.1, as

$$\begin{aligned} |u_{\mathrm{out}}\rangle &= \mathrm{J}\ |u_{\mathrm{in}}\rangle && (3.2)\\ &= \mathrm{J}\,|H\rangle\langle H|u_{\mathrm{in}}\rangle + \mathrm{J}\,|V\rangle\langle V|u_{\mathrm{in}}\rangle && (3.3)\\ &= e^{i\ell_1\phi}\langle H|u_{\mathrm{in}}\rangle|H\rangle + e^{i\ell_2\phi}\langle V|u_{\mathrm{in}}\rangle|V\rangle && (3.4)\\ &= \sqrt{\alpha}e^{i\ell_1\phi}|H\rangle + \sqrt{\beta}e^{i\ell_2\phi}|V\rangle, && (3.5) \end{aligned}$$

where $\sqrt{\alpha} = \langle H|u_{\mathrm{in}}\rangle$ and $\sqrt{\beta} = \sqrt{1-\alpha} = \langle V|u_{\mathrm{in}}\rangle$ are the relative modal weightings of the two azimuthal phases $e^{i\ell_1\phi}$ and $e^{i\ell_2\phi}$, respectively. The converse process, however,

is also true. The OAM state may be collapsed when the transmitted conjugate OAM beam returns through the J-plate.

Mapping all the states on the Generalised HOPS can be accomplished by varying the polarisation incident on the J-plate. The incident polarisation can be controlled using wave plates such as a half-wave plate (HWP) that is presented in the Jones formalism by

$$\mathrm{HWP}(\theta) = \begin{pmatrix} \cos(2\theta) & \sin(2\theta) \\ \sin(2\theta) & -\cos(2\theta) \end{pmatrix}. \tag{3.6}$$

Incorporating the J-plate inside the laser resonator thus provides full control of the polarisation and OAM state with higher fidelity and flexibility than q-plates. This is illustrated in Fig. 3.2 where we unfold the cavity to display conversion of OAM during one round trip. At mirror M_1 we start with a linearly polarised Gaussian beam. Here polarisation was controlled by passing the beam through a HWP. Upon transmission through the J-plate, the beam acquires OAM according to the polarisation input. The beam reflected from M_2 then reverses the OAM charge due to the reflection operation. Thus when passing back through the J-plate, the acquired charge cancels the OAM carried to give a Gaussian back. Accordingly, the state from the output coupler M_2 may be dynamically altered by simply changing the incident polarisation through alteration of the HWP's fast axis. This then allows one to generate all the states on the HOPS. The output state is consistently represented by an intensity distribution that has a central null, independent of its position on the Generalised HOPS.

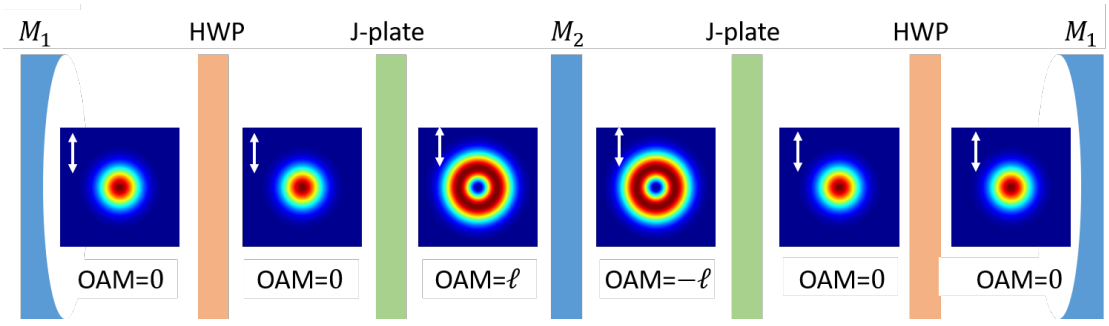


FIGURE 3.2: Schematic shows the transverse modes inside an unfolded cavity around the output coupler M_2 during one round trip. For some linear polarisation state represented by a double side arrow, the purity of the polarisation state is controlled by a half-wave plate HWP. Upon transmission through the J-plate, the beam acquires OAM of topological charge ℓ. Acting in reverse the OAM state is suppressed while maintaining the initial polarisation state and self repeating mode.

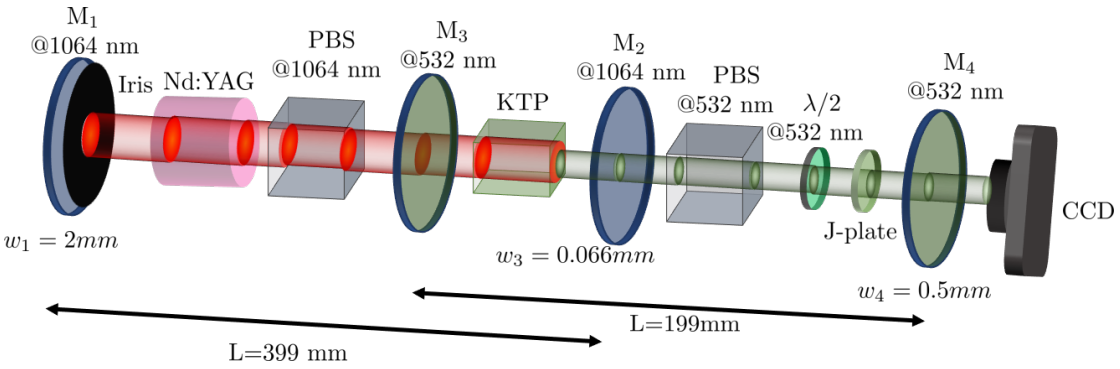


FIGURE 3.3: Experimental schematic of a nonlinear overlapped IR/green laser resonator for the intra-cavity generation of HOPS beams. The IR resonator consists of two mirrors M_1 and M_2 with Nd:YAG gain medium. The IR resonator serves as a pump for the second harmonic generation resonator. The overlapped green cavity comprised mainly of a KTP crystal that is placed in the resonators overlapped region and two mirrors M_3 and M_4 (green output coupler). A polarising beam splitter (PBS) is used to set the intra-cavity polarisation to the horizontal. The HWP is rotatable at some angle θ for controlling the polarisation states incident on the J-plate resulting in the active selection of arbitrary vector vortex modes.

3.2 Experimental Implementation of the J-plates

The J-plate was designed to efficiently modulate green light of wavelength 532 nm. Incorporating the J-plate directly inside a solid state laser was performed by constructing a nonlinear double cavity laser. Here, an Nd:YAG resonator operates as a pump (primary) resonator for the overlapped secondary resonator, allowing efficient second harmonic generation, as illustrated in Fig. 3.3. The pump resonator consists of a flash-lamp pumped cylindrical Nd:YAG rod (76 mm long × 6.35 mm diameter, 1.1% doping) inside a cavity comprised of two reflective mirrors, M_1 and M_2. The radius of curvature of output coupler mirror M_1 was 400 mm with 98% reflectivity at 1064 nm while mirror M_2 was a high reflective (HR@1064 nm) plane mirror (R = ∞). The two mirrors were separated by an effective length of $\approx$ 400 mm. The pump cavity was routinely operated at a repetition rate of 8 Hz, however this could be increased to 20 Hz. The cavity was oscillating on a single Gaussian mode with output pulse duration of 20 ns and diameter of $\approx$ 2 mm at M_1. It was possible to extract 2% of the system energy from M_1 yielding an average energy of 6.5 mJ.

For second harmonic generation, a type-I KTP crystal (3×3×5 mm^3) was used. The input (output) faces of the KTP crystal were anti-reflection (AR) coated for wavelength 1064 nm (532 nm). The KTP was placed inside the secondary overlapped cavity that is constructed by mirrors M_3 and M_4. For efficient coupling between the pump and the second harmonic cavities, it was essential for the fundamental mode size to closely match at the position of KTP crystal. Therefore, the KTP crystal was positioned around 390 mm from the mirror M1. The spot size of the 1064 nm beam at the crystal input surface

was measured to be 81 μm (close to the calculated value 82.3 μm), while the spot size of the output green beam was 62 μm at the KTP crystal. This ensured that the green cavity only sustained a Gaussian resonant mode.

The back mirror (M_3) was HR-coated at the second harmonic wavelength (532 nm) and was highly transmitive (HT) at 1064 nm. To guarantee isolation of only 532 nm output from the secondary cavity, M_4 was highly reflective at 1064 nm while coupling 0.8 % of the intra-cavity green light outside the cavity. The resonant mirrors were spaced by an effective distance of $\approx$ 199 mm. A combination of a polarising beam splitter (PBS) and HWP was employed for selecting the polarisation state inside the secondary resonator. Finally, different J-plates were implemented inside the cavity, adjacent to M_4 for intra-cavity generation of HOPS beams. Table 3.1 describes the various J-plates that have been implemented inside the resonator shown in Fig. 3.2.

3.3 Results

The performance of the second harmonic generation of the KTP crystal was examined under a single pass configuration by placing it inside the pump cavity and then measuring the 532 nm output energy. With an incident pump energy of 318 mJ, only 16 mJ average energy was obtained through single-pass frequency doubling. The average output energy enhanced to 194 mJ (more that 12 times higher) when M_4 was positioned to form the secondary cavity (as shown in Fig. 3.2). The conversion efficiency of the KTP crystal is illustrated in Fig. 3.4 under a single pass and cavity configurations. Figure 3.4 shows an increase in the conversion efficiency of the KTP from 18% (single pass) to 61% by placing M_4 to form a cavity.

3.3.1 Generation of HOPS Beams with Conjugate OAM States

For intra-cavity generation of HOPS beams, J-plate 1, given in Table 3.1, was implemented inside the green resonator and positioned close to M_4. We initially analysed the output of the resonator by varying the angle of the HWP's fast axis (θ) from 0 to $\pi/4$. Here, the output was persistently a doughnut-shaped intensity beam independent of the HWP angle. The output state may be described as $u_{\text{out}} = a_1 |H, -1\rangle + a_2 |V, 1\rangle$, where a_1 and a_2 are the relative modal weightings for the pure OAM states represented on the poles of the HOPS.

Next we demonstrated modal decomposition measurements to measure the output OAM state by performing an azimuthal inner product using a spatial light modulator (SLM).

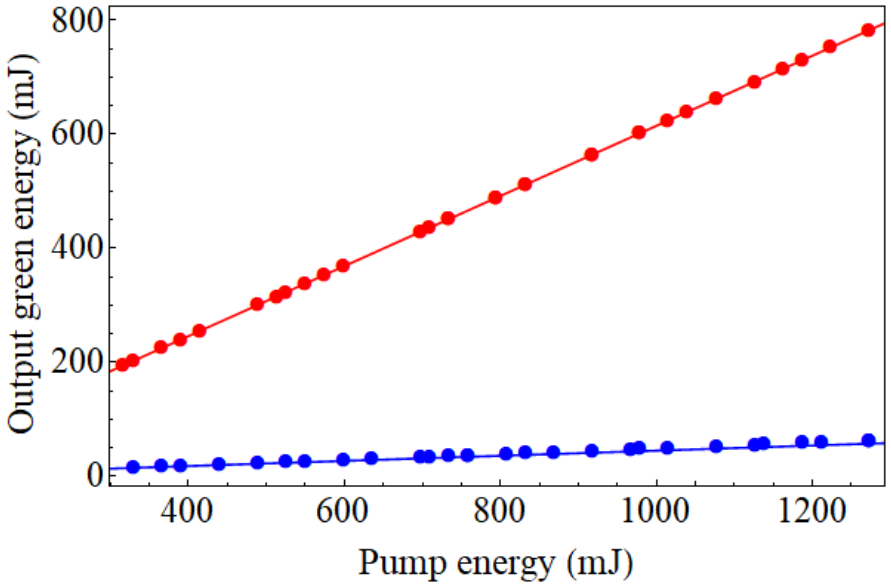


FIGURE 3.4: Shows conversion efficiency of the second harmonic generation beam through a single pass (blue data points) and within a cavity configuration (red data points) together with their fitting curves (solid line).

TABLE 3.1: Shows the different J-plates used inside the non-linear resonator with the corresponding output OAM mode when the incident polarisation on the J-plate are horizontal and vertical polarisation.

incident state	$\|H, \ell = 0\rangle$	$\|V, \ell = 0\rangle$
J-plate 1	$\|H, \ell = -1\rangle$	$\|V, \ell = 1\rangle$
J-plate 2	$\|H, \ell = 1\rangle$	$\|V, \ell = 5\rangle$
J-plate 3	$\|H, \ell = 10\rangle$	$\|V, \ell = 100\rangle$

We digitally encoded the SLM with spatial field $\exp(i\ell\phi)$ with ℓ varying for -2 to 2 in unit steps. A pure OAM state of $\ell = -1$ for HWP angle $\theta = 0$ was detected with 94% purity as shown in Fig. 3.5 (a) with the corresponding modal decomposition channel. By rotating the angle of the HWP $\theta = \pi/4$, the modal decomposition confirmed that the output beam tuned to a pure $\mathrm{LG}_{0,-1}$ mode with purity of 96%.

This is represented in Fig. 3.5 (a) with the images of the raw data for the modal decomposition channels in Fig. 3.5 (b). Here the on-axis intensity indicates the existence of the mode and on-axis null intensity indicates the absence of the mode at the plane of measurement.

The modes generated from the cavity are not limited to pure $\mathrm{LG}_{0,\pm1}$ modes but also any superposition of these two modes. These superpositions can easily be selected by simply rotating the HWP angle. For example, we experimentally generated a pure vector vortex mode, i.e. $u_{\mathrm{out}} = \sqrt{0.5}\,|H, -1\rangle + \sqrt{0.5}\,|V, 1\rangle$, by simply adjusting the HWP angle at $\theta = 22.5°$. The output mode was qualitatively identified by passing

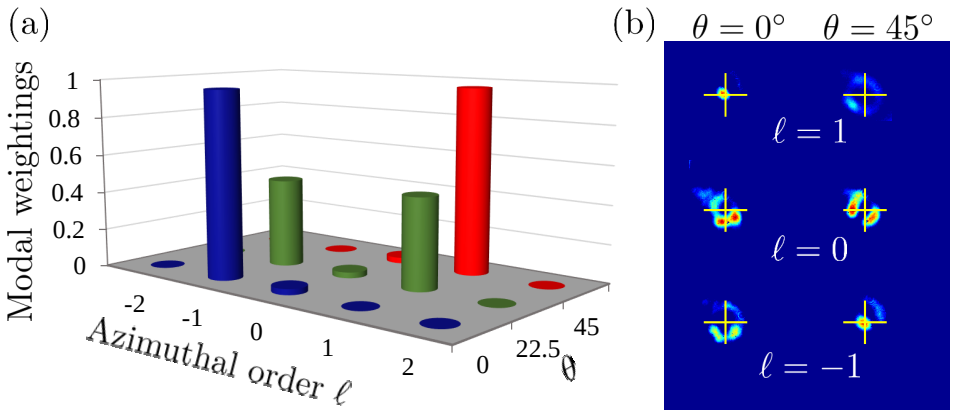


FIGURE 3.5: Modal decomposition measurements are executed on the output mode to evaluate the modal weightings when the HWP angle $\theta = 0°$, 22.5° and 45°. (b) shows the raw data where on-axis intensity (as indicated by the cross-hairs) means existence of the mode while no intensity indicates the mode's absence.

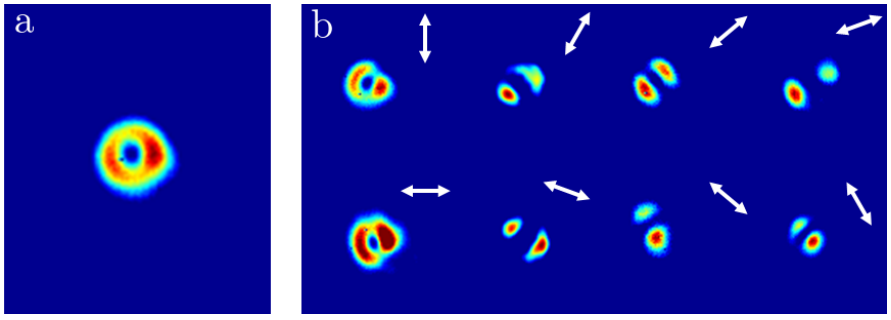


FIGURE 3.6: (a) Shows a pure vector vortex mode selected by propagating a diagonally polarised light through the J-plate. (b) shows a qualitative test of the vector vortex mode by passing it through a linear polariser. The orientation of the polariser is depicted by double side arrows

through a linear polariser. Accordingly, the mode splitted into two lobes that rotated when changing the polariser orientation (represented by double side arrows) as shown in Fig. 3.6. Decomposing the state quantatively confirmed the generation of equally weighted $\mathrm{LG}_{0,\pm1}$ modes as shown in Fig. 3.5.

3.3.2 Generation of HOPS Beams with Independent OAM States

Our cavity was not only limited to the generation of Generalised HOPS beams with conjugates OAM states, i.e. $\mathrm{LG}_{0,\pm1}$ modes and their superpositions. Independent pure LG modes and superposition with net OAM modes were also realised from the cavity. By switching J-plate 1 to J-plate 2, we demonstrated the generation of hybrid states $u_{\mathrm{out}} = a_1\mathrm{LG}_{0,1} + a_2\mathrm{LG}_{0,5}$, without any physical changes to the cavity.

We have verified that the cavity was generating two independent OAM states by executing modal decomposition measurements with digitally encoded field $\exp(i\ell\phi)$ with

ℓ varies in unit step from -6 to 6 as shown in Fig. 3.7. We identified OAM states of magnitude $\ell = 1$ with purity of 91% and $\ell = 5$ with purity of 88% corresponding to HWP angles $\theta = 0°$ and $\theta = 45°$, respectively.

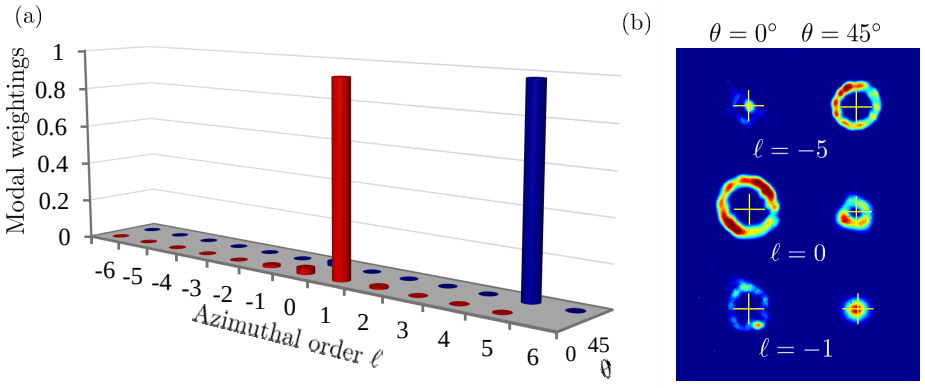


FIGURE 3.7: Shows azimuthal inner product measurements executed to evaluate the modal weightings of the output state. The measurements confirm the existence of pure $LG_{0,1}$ at HWP angle $\theta = 0°$ while pure $LG_{0,5}$ at $\theta = 45°$. (b) shows the raw data for the measurements at the Fourier plane where on-axis intensity means mode exists, null intensity means absence of the mode.

Different HOPS beams have been selected by introducing a phase shift into the incident polarisation. This was achieved through changing the HWP angle θ to map all the possible states on the corresponding HOPS. The output beam was evolving from pure $LG_{0,1}$ mode ($\theta = 0°$) to a pure $LG_{0,5}$ ($\theta = 45°$) with a superposition of the states in-between. Figure 3.8 shows the continuous evolution from $LG_{0,1}$ state to $LG_{0,5}$ state as a function of changing input polarisation to the J-plate. These superposition states are vector vortex modes with a net OAM equivalent to $\ell = 6$.

In principal, there is no limit to the OAM that can be created from inside the laser cavity. We confirmed this by implementing J-plate 3 where OAM= 10 was acquired by horizontal polarised input beam and OAM= 100 by vertical polarised beam. The output mode thus had two concentric modes with different OAM orders.

We confirmed the output OAM state by performing modal decomposition measurements as stated earlier. Our measurements recognised an OAM signal of order $\ell = 10$ with purity 89% and $\ell = 100$ with purity of 78% for HWP orientation $\theta = 0°$ and $\theta = 45°$, respectively. The raw data for the measurements are depicted in Fig. 3.9 for the HWP angles $\theta = 0°, 45°$ with their corresponding measurements channels.

The hybrid states on the HOPS were selected by varying the HWP angle from $\theta = 0°$ to $\theta = 45°$, the output beam thus evolve from pure $LG_{0,10}$ to a pure $LG_{0,100}$, respectively, with superpositions state in-between, as illustrated in Fig. 3.10.

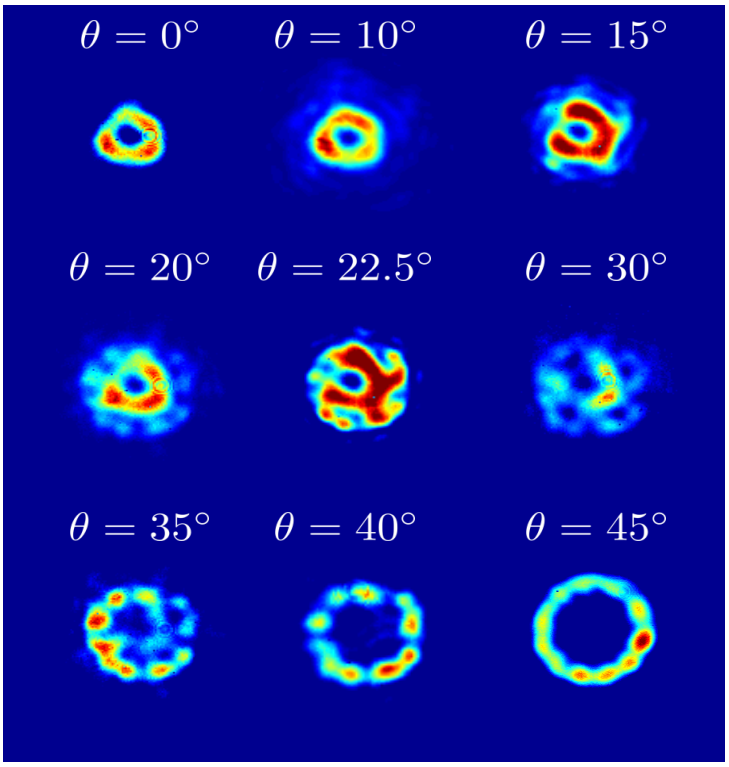


FIGURE 3.8: The output intensity profile of the laser after placing the J-plate 2. The output mode evolves from pure $LG_{0,1}$ at HWP angle $\theta = 0°$ mode to pure $LG_{0,5}$ at $\theta = 45°$ with superposition state in between.

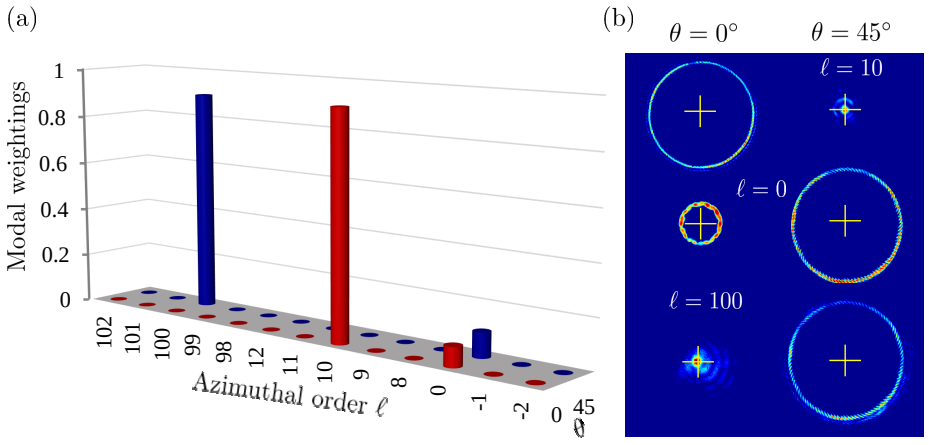


FIGURE 3.9: Shows azimuthal inner product measurements executed to evaluate the modal weightings of the output state. The measurements confirm the existence of pure $LG_{0,10}$ at HWP angle $\theta = 0°$ while pure $LG_{0,100}$ at $\theta = 45°$. (b) shows the raw data for the measurements at the Fourier plane where on-axis intensity means the mode exists, null intensity means absence of the mode.

One should mention that the Gaussian beam size in the green cavity is an important factor when implementing the J-plates inside the cavity. If the beam size is much bigger that the size of the active area of the J-plate (i.e. the area of the modulating fins), no modulation of light would occur due to diffraction. Instead, we can see the nanostructure

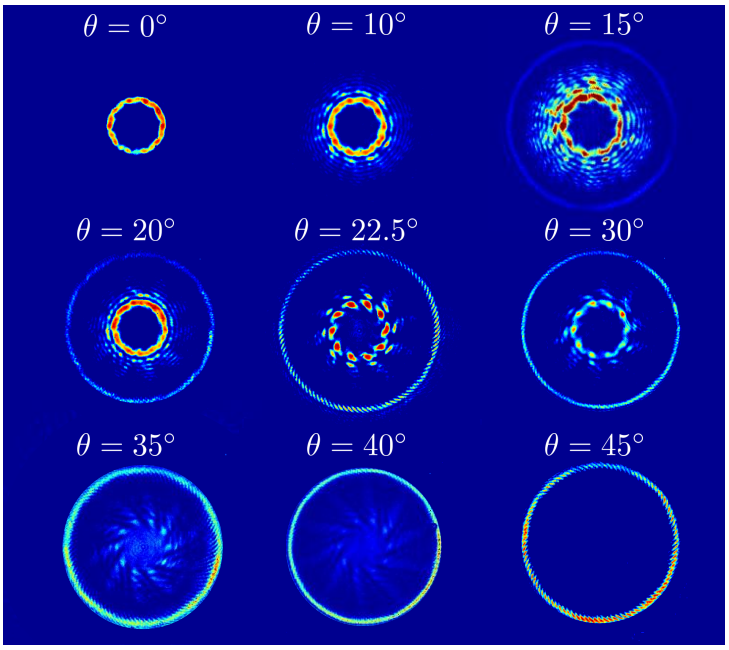


FIGURE 3.10: The output intensity profile of the laser after placing the J-plate 3. The output mode evolves from pure $LG_{0,10}$ at HWP angle $\theta = 0$ mode to pure $LG_{0,100}$ at $\theta = 45°$ with superposition state in between.

fins of the metasurface directly on the CCD camera as shown in Fig. 3.11. This drawback comes from the fact that the performance of any phase elements deteriorate with the variation in the initial beam size.

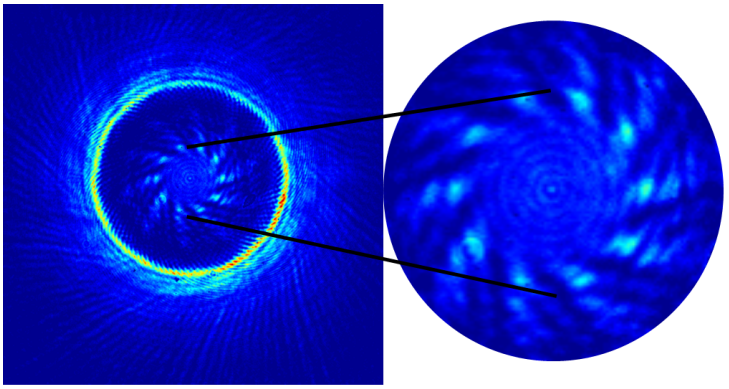


FIGURE 3.11: Shows the nano-antennas diffract light with no modulation when the incident beam size is bigger that metasurface active area. The incident beam was 3.2 mm in diameter while the active area of the metasurface was 2 mm in diameter.

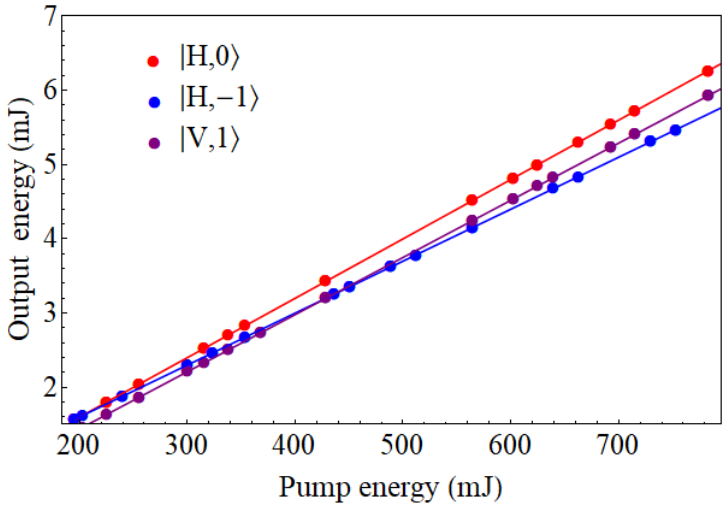
Finally, we tested the slope efficiency measurement for the pure OAM output modes. Figure 3.12 illustrates the average output energy of each pure OAM mode for the indicated J-plates in comparison to the Gaussian power. The slope efficiency for $LG_{0,\pm1}$ modes were approximately similar to the Gaussian which reveal that the J-plate 1 does not lead to high losses inside the cavity. Figure 3.12 (b) and (c) disclose that higher-order modes generated by J-plate 2 and J-plate 3 introduce higher losses and thus require a

higher threshold comparing with J-plate 1 modes. For comparison the power handling capability of the J-plates and liquid crystal elements, the J-plates showed increase in the power handling capability 6 times higher than the q-plates and SLM.

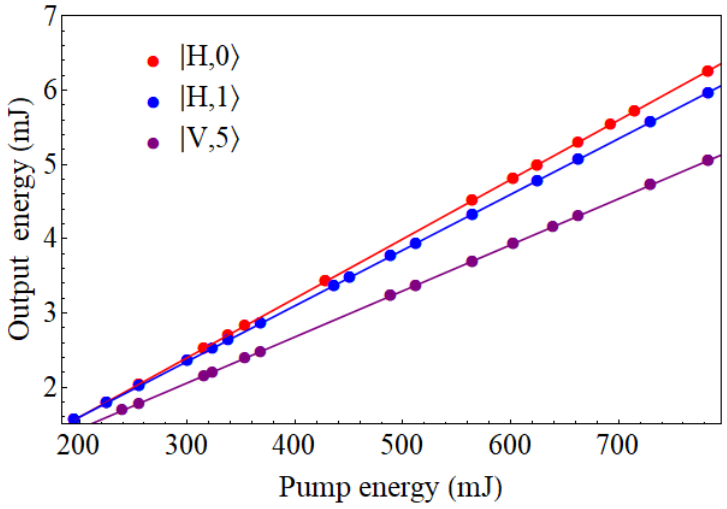
It is worth mentioning that the slope efficiency was low due to the low transmission of mirror M_4 which was 0.8%. Therefore most of the cavity power has been locked inside. This was for the analysis of the power handling capability of the metasurface J-plates which in return showed a potential to be used for the generation of high power HOPS beams. Nevertheless, the output coupler could be replaced by another with lower reflectivity in case higher output power is needed.

3.4 Conclusion

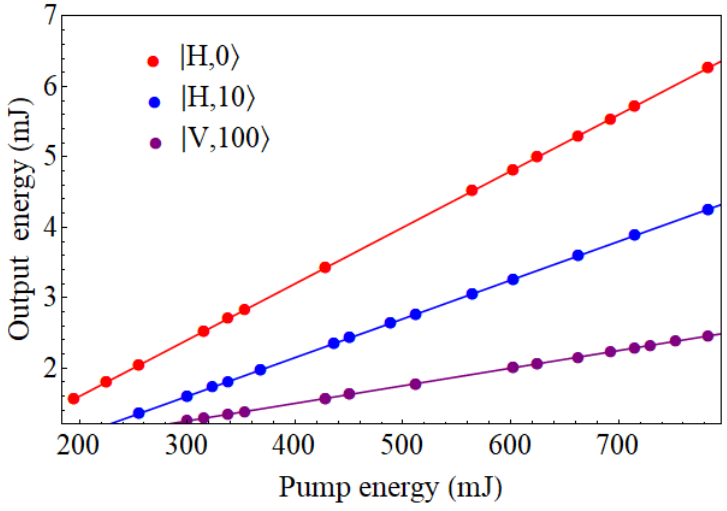
In this chapter, we investigated the design of a novel laser for active selection of HOPS beams of different orders from inside the laser cavity by controlling the light's different degrees of freedom such as polarisation, OAM state and wavelength all in one cavity. It was very clear that generation of intra-cavity pure OAM modes was limited to output conjugate values $\pm\ell$ and specific input polarisation states. In this chapter, we overcame these restrictions and succeeded for the first time to perform spin-orbital conversion with any input polarisation into arbitrary OAM states with the aid of the geometric metasurface J-plate. We have controlled the polarisation and the OAM state inside the laser system in a completely effortless way. We showed that through judicious control over the orientation of the HWP, any HOPS can be mapped. These results were affirmed by executing modal decomposition measurements to confirm the output of our cavity. We have demonstrated generation for HOPS beams without changing the physical cavity. We succeeded to generated an OAM state of order OAM = 100, which is the highest state generated from inside the cavity. The system showed power handling capability at least 6 times higher than what was previously achieved which paves the way for more advances toward high brightness vortex lasers.



(a)



(b)



(c)

FIGURE 3.12: Average output energy of the secondary cavity for the fundamental Gaussian mode (red data points) of the resonator versus corresponding HOPS beams generated using (a) J-plate 1 ; (b) J-plate 2; and (c) J-plate 3, with the fitting curve of the measurements.

Chapter 4

A Beam Quality Measure for Vector Beams

Vector beams are usually differentiated from scalar beams by qualitative measures, e.g. visual inspection of beam profiles after a rotating polariser. In this chapter, we introduce a quantitative beam quality measure for vector beams, which we demonstrate on cylindrical vector vortex beams. We show how a single measure can be defined for the vector purity, ranging from 0 (purely scalar) to 1 (purely vector).

4.1 Introduction

Since the invention of the laser and the definition of its transverse modes, many studies have considered the question of a beam quality factor for arbitrary laser modes [28]. In the early 1990s tools traditionally associated with statistics were applied to laser beams with uniform polarisation (scalar beams), exploiting the analogous behaviour between probability density functions and laser beam intensity profiles [115]. Viewing the latter as a probability of finding the light, statistical moments were used to define beam and divergence widths as second moments of the intensity, ultimately giving rise to a beam quality factor, M^2, as a single measure of any scalar mode [116]. This measure has since been extensively studied, with novel digital measurement techniques [117], and is incorporated into the ISO standards for measuring and defining laser beams.

Despite the many advances in generating them, the means to detect them lags behind. Such detection techniques include the use of rotating analysers together with interferometers [118], as well as geometric phase plates with single-mode fibres [119]. Importantly, no quantitative measure exists to define the quality of a vector mode: i.e. to differentiate

them from scalar modes. Presently this is done by qualitative means, e.g. measuring the profile change after a polariser, or by averaging the degree of polarisation across the beam.

In this chapter, we demonstrate a technique to generate and measure, quantitatively, the state of "vectorness" of an arbitrary vector beam. We generate vector vortex beams by modulating the geometric phase of light using a liquid crystal q-plate. Because vector beams can be viewed as "entangled" or non-separable in their spatial and polarisation degrees of freedom, we apply entanglement measures to quantify this quintessential property of vector modes, which we call the vector quality (purity). We demonstrate this technique on a variety of beams in a continuous range from purely scalar to purely vector. This work offers a new tool for laser beam characterisation of vector modes.

4.2 Theory

To begin, let's start with a fundamental Gaussian beam u_0 that is given by

$$u_0 = A \exp\left(\frac{-r^2}{w^2}\right), \tag{4.1}$$

where A is the total field intensity at the source, w is the beam size and r is the radial distance from the center axis of the beam. If such beam has a polarisation component along the horizontal axis then, it is described in the Jones formalism as

$$U = u_0 \begin{pmatrix} 1 \\ 0 \end{pmatrix}. \tag{4.2}$$

For the selection of different input polarisation, a quarter-wave plate ($\lambda/4$) is required. A rotating quarter-wave plate with some angle θ can be represented in the Jones form as

$$\lambda/4 = \begin{pmatrix} \cos^2(\theta) + i\sin^2(\theta) & (1-i)\sin(\theta)\cos(\theta) \\ (1-i)\sin(\theta)\cos(\theta) & \sin^2(\theta) + i\cos^2(\theta) \end{pmatrix}, \tag{4.3}$$

We pass this beam through a q-plate. The q-plate couples the polarisation into OAM state. The q-plate sets the OAM of the incident field U into one or two OAM values depending on the handedness of the incident polarisation [47–49]. The q-plate can be described in Jones matrix form as

$$Q = \begin{pmatrix} \cos\ell\phi & \sin\ell\phi \\ \sin\ell\phi & -\cos\ell\phi \end{pmatrix}, \tag{4.4}$$

where ℓ is the topological charge of the q-plate and ϕ is the q-plate azimuthal angle. The beam after the q-plate may be expressed as

$$U = u_0 \left[\cos(\theta) \exp(-i\ell\phi) \begin{pmatrix} 1 \\ i \end{pmatrix} + \sin(\theta) \exp(i\ell\phi) \begin{pmatrix} 1 \\ -i \end{pmatrix} \right]$$

or

$$= u_0 \left[\cos(\theta) \exp(-i\ell\phi)\mathbf{e_L} + \sin(\theta) \exp(i\ell\phi)\mathbf{e_R} \right], \tag{4.5}$$

where $\mathbf{e_L}$ and $\mathbf{e_R}$ represent left- and right-handed polarisation states with associated spatial modes $\exp(-i\ell\phi)$ and $\exp(i\ell\phi)$, respectively. The parameter θ determines whether the transverse mode U is purely vector ($\theta = (n+1)\,\pi/4$), purely scalar ($\theta = n\pi/4$) or some partially vector mode, where n is a positive even integer. We pose the questions: given only the left-hand side of Eq. (4.5), what should a suitable measure be to determine whether the beam is vector or not, and how can this be measured? We would like a vector quality factor that maps purely scalar through purely vector beams on a scale from 0 to 1.

To achieve this, we elect to draw a similarities between the entangled quantum states and classical vector beams, both sharing the property of nonseparablity. Indeed, this is the quintessential property of the entangled system with the classical analogue sometimes referred to as classical entanglement and beyond a purely mathematical analogue, has been shown to have physical significance. Applying quantum tools to our vector modes allows us to quantify their vector purity, since the vector purity is precisely the degree of nonseparablity of the mode. Here we use the concurrence C [120] (a quantum tool to measure the degree of entanglement in quantum mechanics), as a measure to define the vector purity (V) of classical vector beams as

$$V = \mathrm{Re}(C) = \mathrm{Re}\left(\sqrt{1 - s^2}\right) = |\sin(2\theta)|\,, \tag{4.6}$$

where s is the length of the Bloch vector, defined as:

$$s = \left(\sum_i \langle \sigma_i \rangle^2 \right)^{1/2}. \tag{4.7}$$

Here $i = 1, 2, 3$ and σ_i are the expectation values of the Pauli operators, which represent a set of normalised intensity measurements. Optically, s corresponds to the degree of polarisation of the averaged polarisation state that can be obtained from the density matrix ρ of the state with $|U\rangle\langle U|$, where a detailed derivation can be found in [121].

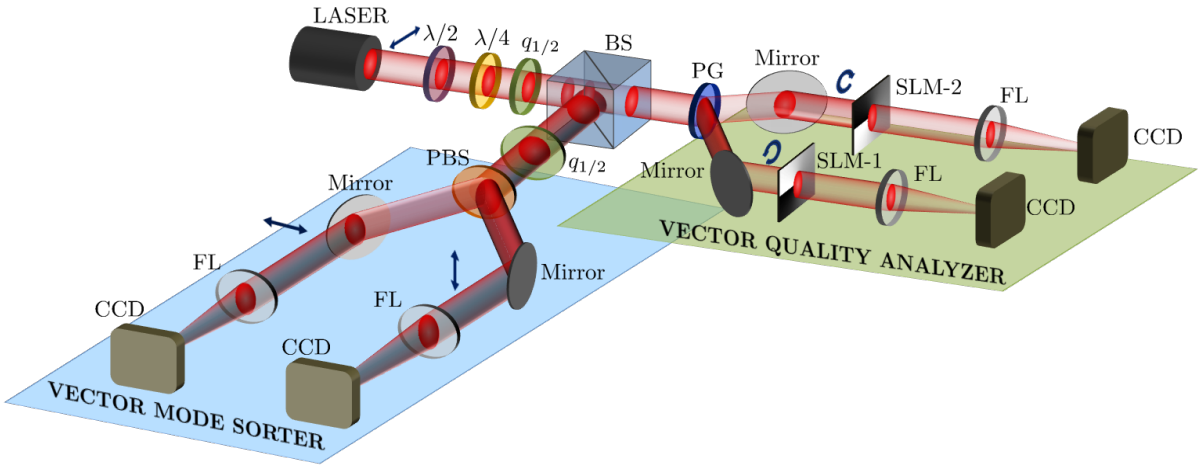


FIGURE 4.1: Experimental generation and analysis of vector modes. Using a half-wave plate ($\lambda/2$) to adjust the polarisation of the fundamental Gaussian mode, we generated cylindrical vector modes with a q-plate of topological charge $q = 1/2$. The q-plate is aligned such that its global phase is zero with respect to the horizontal axis. The generated vector modes was directed into two detection systems. On one hand, we distinguished between vector modes using a sorter, whereby the beam was passed through a second q-plate and a polarising beam splitter (PBS); the two acting as a correlation filter. The output of the correlation was measured at the Fourier plane using a Fourier lens (FL). On the other hand, we determined the vector quality factor by performing a series of polarisation projections using a polarisation grating (PG), and OAM projections using phase patterns encoded on the spatial light modulator (SLM). The outputs were measured in the Fourier plane of two Fourier lenses. BS: beam splitter, CCD: charge-coupled device

To calculate s, only twelve normalised, on-axis intensity measurements are required: six identical measurements performed for two different basis states. The intensities I_{ij}, normalised to the maximum of I, are defined by the chosen measurement basis i, and six projection measurements j. If circular polarisation is chosen as the measurement basis, i.e. $i = \{L, R\}$, then the projection measurements are represented by two pure OAM modes, $\ell, -\ell$, and four superposition states, $\exp(i\ell\phi) + \exp(i\alpha)\exp(-i\ell\phi)$, defined by the intermodal angle $\alpha = 0,\ \pi/2,\ \pi,\ 3\pi/2$. Table 4.1 shows how each intensity is assigned to its respective basis state and projective measurement for a first-order vector vortex mode.

TABLE 4.1: Designation of normalised intensity measurements

Basis state	$\ell = 1$	$\ell = -1$	$\alpha = 0$	$\pi/2$	π	$3\pi/2$
L	I_{11}	I_{12}	I_{13}	I_{14}	I_{15}	I_{16}
R	I_{21}	I_{22}	I_{23}	I_{24}	I_{25}	I_{26}

These six OAM measurements map the higher-order Poincaré sphere [122]. This technique is an adaptation of a full-state tomography that is more commonly used for quantum entangled states, where an over-complete set of measurements is used to describe

the full density matrix and compute the degree of entanglement [123]. The expectation values of the Pauli operators are computed from I as follows:

$$\langle\sigma_1\rangle = (I_{13} + I_{23}) - (I_{15} + I_{25}), \tag{4.8}$$

$$\langle\sigma_2\rangle = (I_{14} + I_{24}) - (I_{16} + I_{26}), \tag{4.9}$$

$$\langle\sigma_3\rangle = (I_{11} + I_{21}) - (I_{12} + I_{22}). \tag{4.10}$$

These expectation values resemble the Stokes parameters used in recovering the polarisation distribution [124], but are in fact fundamentally different: they do not represent a series of polarisation measurements but rather a series of holographic measurements of the spatial field (i.e. the OAM state), and result in a measure of the degree of non-separability of vector beams.

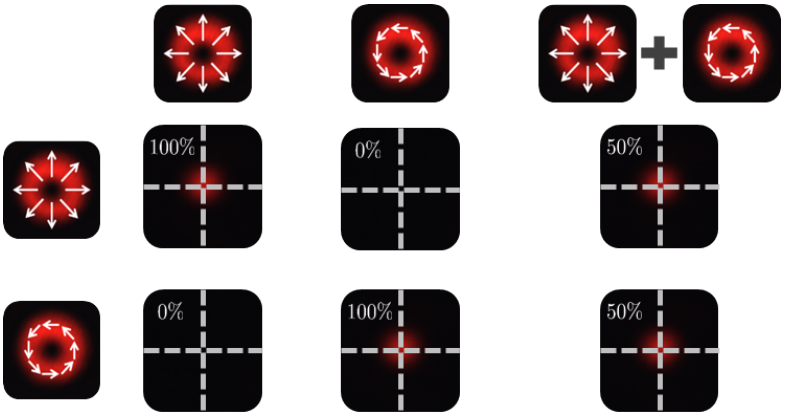


FIGURE 4.2: Sorting of radially and azimuthally polarised vector vortex beams. By measuring the on-axis intensity, the relative weightings of radially and azimuthally polarised vector modes were determined for both pure and superposition states.

4.3 Experiment

We implement this experimentally by employing a combination of geometric and dynamic phase control. Figure 4.1 shows the generation of a vector vortex beam using a q-plate [47–49], which follows the selection rules (written in bra-ket notation): $|\ell, L\rangle \rightarrow |\ell + Q, R\rangle$ and $|\ell, R\rangle \rightarrow |\ell - Q, L\rangle$. The azimuthal charge introduced by the q-plate is $Q = 2q = 1$. Note that the polarisation of the incident beam determines the generated vector mode.

The generated vector mode can be analysed in two different systems: a vector quality detection scheme and a vector mode sorter. The latter distinguishes between different vector modes, while the former provides a quantifiable measure of the quality of the vector mode. Both systems make use of a modal decomposition technique [43], where

an inner product of the incident field with a matching filter is used to determine the weighting coefficients of the modes. Here, an input field $U(\mathbf{r})$ is decomposed into basis states $u_p(\mathbf{r})$, such that $U(\mathbf{r}) = \sum_p a_p u_p(\mathbf{r})$. The modulus of the modal weighting coefficients a_p can be determined by the inner product of the incident field with a matching filter: $|\langle u_p|U\rangle| = |a_p|$. Optically, the inner product is performed by directing the incident beam onto a matching filter and viewing the Fourier transform, with the use of a lens (FL), on a CCD camera [43].

In the case of the mode sorter, which distinguishes between radially and azimuthally polarised vector beams, a q-plate of charge $q = 1/2$ together with a polarising beam splitter (PBS) formed the match filter for the modal decomposition. The q-plate converts a radially (azimuthally) polarised vector vortex beam into a Gaussian mode with homogeneous polarisation. A Fourier lens (FL) was placed in each polarisation arm and the on-axis intensity was recorded on the CCD camera. That is, if a radially (azimuthally) polarised vector vortex beam is directed into the mode sorter, a non-zero on-axis intensity will only be detected in the horizontal (vertical) polarisation arm. The experimental results are shown in Fig. 4.2, where a radially and an azimuthally polarised vector vortex beam were both detected with 100% certainty in each case. If the incident beam consists of a mixture of azimuthal and radial vector modes Fig. 4.2, the decomposition technique allows the relative weightings to be accurately determined as shown in [125].

The vector quality factor does not depend on the type of vector beam and can be determined by performing measurements on both the polarisation and OAM degrees of freedom, in principle in any basis. This is a consequence of the fact that entanglement does not change with a change of basis. The polarisation component was measured using a polarisation grating (PG), which uses geometric phase to diffract light into two beams in the $+1$ and -1 orders such that the two output beams have opposite circular polarisations [126]. Each polarisation arm was directed onto a spatial light modulator (SLM) encoded with a digital phase pattern that acts as the azimuthal match filter for the decomposition. SLMs are polarisation sensitive in that the desired beam reflected from the screen consists of only horizontally polarised light. As such, there is no need to place an additional quarter-wave plate before the SLMs to convert circular polarisation to linear. In order to satisfy Eqs. (4.8 - 4.10), the on-axis intensity for six different OAM states were measured in each polarisation arm. Figure 4.3(a) and 4.3(b) show the twelve normalised intensity measurements for a vector and scalar vortex beam, respectively. In this case, the circular polarisation basis was chosen and six different OAM projections were made for both the left- and right-circular polarisation states. Phase-only holograms were encoded onto the SLM to detect the azimuthal component of the vortex modes.

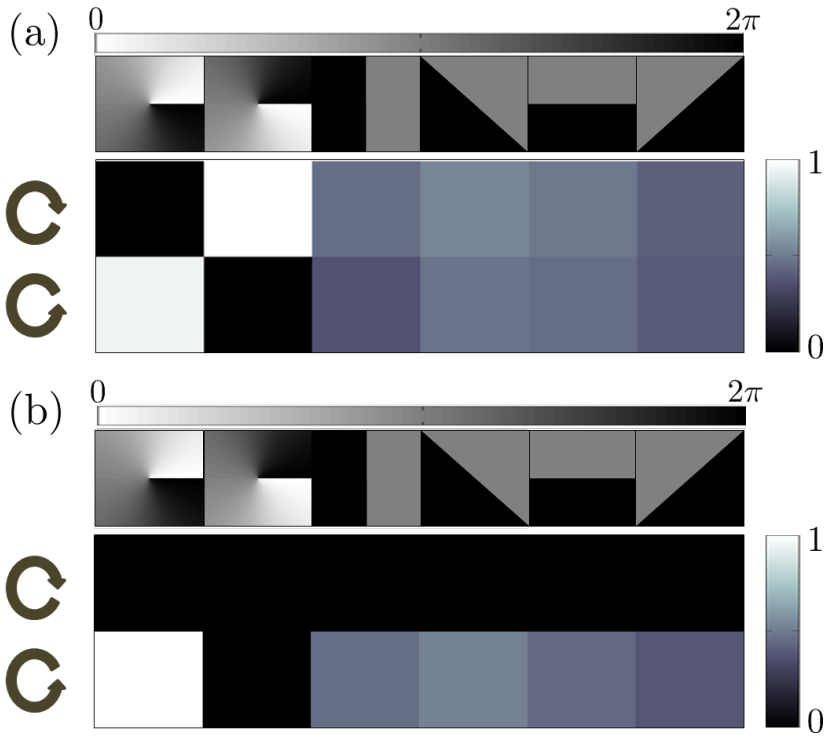


FIGURE 4.3: Graphical depiction of the actual intensity measurements corresponding to those of Table 1, with the holograms shown in each column and the two polarisation measurements in the rows. We illustrate two examples, (a) a vector vortex mode and (b) a scalar vortex mode. The scalar mode has only one polarisation component and is separable, whereas the vector mode has both and is non-separable.

Using Eq. 4.6, the purity V was calculated to be 0.98 ± 0.01 for a radially polarised vector vortex beam and 0 for a scalar vortex mode. By simply rotating the quarter-wave plate, $(\lambda/4)$, before the first q-plate in the generation section, the state of the beam created can be varied continuously from purely vector to purely scalar; this amounts to varying θ in Eq. 4.5. As such, the purity V was measured for different orientations of the quarter-wave plate and the results, graphically illustrated in Fig. 4.4, show that this measurement of the vector quality maps purely scalar through to purely vector beams with the range 0 through 1. The small deviation of the experimental results from the theory is due to experimental errors.

Moreover, the intensity measurements necessary to compute the purity can, equally, be obtained in real-time with a single measurement by multiplexing all the required holograms into one single hologram displayed on the SLM [127]. A superposition of the six previously used match filters, each having a transmission function $t_n(\mathbf{r})$ and a unique carrier frequency K_n, were encoded on two halves of a single SLM. The transmission function of each half is thus given by

$$T(\mathbf{r}) = \sum_{n=1}^{6} t_n(\mathbf{r}) \exp(iK_n r), \tag{4.11}$$

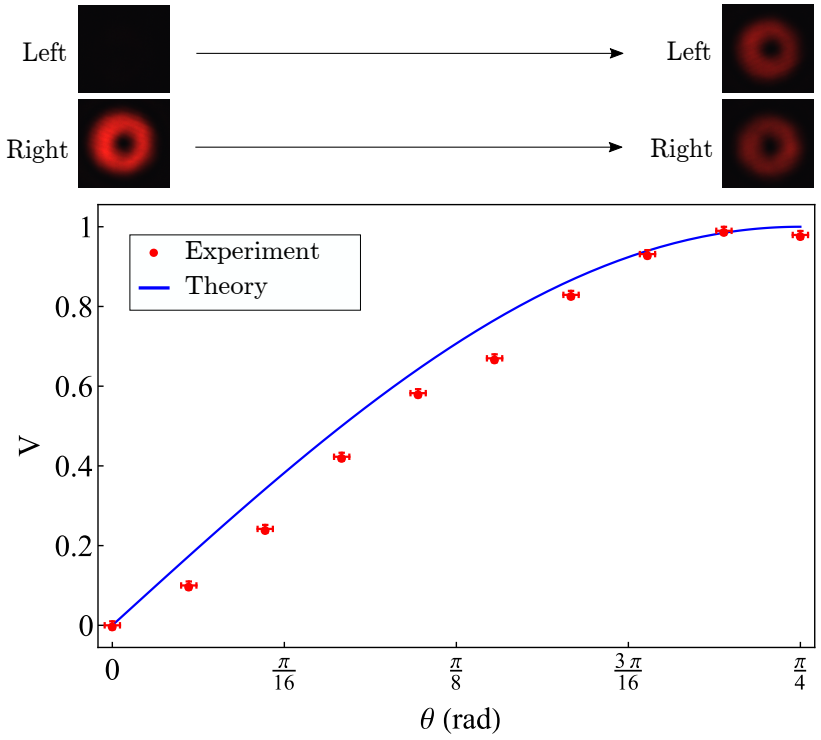


FIGURE 4.4: Evolution of the vector quality factor (V) with respect to the nature of the input state. Using a quarter-wave plate, the polarisation of the input Gaussian beam was varied from linear to circular, such that the vortex beam generated after the q-plate varied from vector to scalar, respectively. The purity was calculated from the 12 decomposition measurements (red dots) and plotted against the theoretical prediction (blue solid line) for each orientation of the quarter-wave plate. The experimental images show the relative intensities of the left- and right-circular polarisation states for different orientations of the quarter-wave plate.

resulting in a total of 12 outputs on the CCD camera as shown in Fig. 4.5(a). The intensities of the modes detected by each of the 12 match filters, as well as the detector positions for the entries I_{ij}, for both vector and scalar vortex beams, are shown in Fig. 4.5(b) and Fig. 4.5(c), respectively.

We point out here that while our implementation has been based on vector vortex beams, this is for convenience only. The concept and definition of a vector beam quality factor is independent of the type of vector beam under study, and only the optical elements in the measurement setup would require change (we anticipate that many users will require a measure for a known form of vector beam). Moreover, this approach produces a single number that immediately indicates how vector the mode is, i.e. a quantitative measure. In contrast, the degree of polarisation produces a number for every point on the field, and thus while this is quantitative for a particular point, it does not determine the vector quality of the mode as a whole. Note also that the vector mode sorter step in the experiment is not necessary to determine the vector quality factor, but serves as a secondary confirmation of the mode being analysed. Thus the real-time measurement

of the twelve parameters with a single hologram makes the set-up comparatively as easy as performing a Stokes measurement.

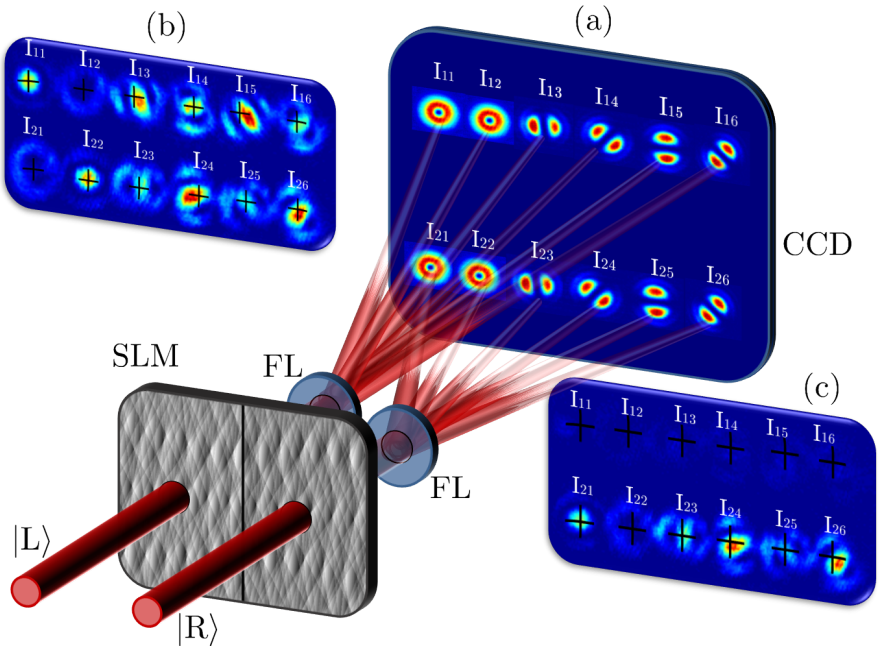


FIGURE 4.5: Single shot measurement of the purity using demultiplexing holograms. Both the left- and right-circularly polarised arms are decomposed using the same set of holograms, such that the upper row of intensities corresponds to the left-circularly polarised arm and the bottom row to the right-circularly polarised arm. (b) and (c) show the intensity patterns of vector and scalar vortex beams on the CCD camera, respectively.

4.4 Conclusion

In this chapter, we explore the extra-cavity generation of vector vortex beams by manipulating the geometric phase of light using a liquid crystal q-plate. We have introduced a new laser beam characterisation tool for quantifying the quality of arbitrary generated vector beams by borrowing concepts from quantum mechanics. We have demonstrated the concept on cylindrical vector vortex beams with varying degree of vector quality, from purely scalar (OAM modes) to purely vector (radially polarised light as an example), and shown excellent agreement between the predicted and measured vector quality factors. Our vector quality factor offers a quantitative measure of the quality of a vector mode, which we believe will be a useful tool in the analysis of such beams in both laboratory and industrial applications.

Chapter 5

Amplification of Higher-Order Poincaré Beams

In this Chapter, we employ a master-oscillator-power-amplifier (MOPA) approach and study the problem of purity of HOPS beams in general through vector beam amplifiers. The gain media, Nd:YAG and Nd:YLF, were selected to cover both non-birefringent and birefringent conditions, respectively, which we show is of paramount importance for maintaining or improving the vector purity after the MOPA system. We execute this study both theoretically and experimentally, showing excellent agreement between the two. Intriguingly, we show that pure vector vortex (VV) beams maintain their vector purity regardless of the gain medium, while general VV beams may have their purity improved by the use of a suitable birefringent amplifier. We model the system holistically from first principle rate equations through to vector orientation. The theory, experimental techniques and results outlined here is a useful tool for advances toward high brightness vector beams where power and quality are simultaneously increased.

5.1 Introduction

The current tools used to generate HOPS beams are limited by low-damage thresholds, preventing high power applications of such beams. However, there is significant interest in high power HOPS beams. To date approaches have included using grating mirrors inside lasers achieving few kilowatts of power [128–130]. While some impressive power levels have been achieved for specific beams types, HOPS beams have not been considered nor the final vector beam purity.

It is self-evident that if the vector nature is needed in a particular application, for example, radially polarised light in laser materials processing or azimuthally polarised light for optical trapping and tweezing, then the vector quality (purity) will play a significant role in the efficacy of the beam for that application. Thus we propose the question: how does the vector purity of the VV beam change with amplification? Analogous to scalar beams, where amplification tends to increase the power at the expense of the mode quality, here we consider if the vector quality likewise changes during amplification.

5.2 Theory

To begin, let us consider a HOPS beam of the form

$$U(r,\phi) = \sqrt{\alpha}\exp(i\ell\phi)\hat{\mathbf{e}}_{\mathbf{R}} + \exp(i\gamma)\sqrt{1-\alpha}\exp(-i\ell\phi)\hat{\mathbf{e}}_{\mathbf{L}}. \tag{5.1}$$

where the vectors $\hat{\mathbf{e}}_{\mathbf{R}}$ and $\hat{\mathbf{e}}_{\mathbf{L}}$ represent the right-circular and left-circular polarisation states that are associated to the complex helical spatial fields $\exp(i\ell\phi)$ and $\exp(-i\ell\phi)$, respectively, and γ is an intra-modal phase. For example, when $\alpha = 0.5$ we have the cylindrical vector vortex (CVV) beams: For $\gamma = 0$ we have radially polarised light, while for $\gamma = \pi$ we have azimuthally polarised light. Of course, when $\alpha = 1\,\text{or}\,0$, the beam is scalar and clearly then partially vector for intermediate states. The quality of the beam represented in Eq. 5.1 may be expressed as

$$V = 2\left|\sqrt{\alpha(1-\alpha)}\right|, \tag{5.2}$$

with the range of 0 (scalar) through 1 (vector). Thus the parameter α defines the transverse mode structure, from purely scalar ($\alpha = 1$ or 0) to purely vector ($\alpha = 0.5$), otherwise it is partially vector. The phase (γ) only produces a rotation and thus does not affect vector purity. For this reason we will neglect it in the rest of this treatment.

Note that this is a special form of the factor V for the case of the state given by Eq. 5.1, which we generalise to arbitrary modes. Nevertheless, it is general in the sense that Eq. 5.1 describes any HOPS beam, from CVV beams to circularly polarised OAM beams, and thus Eqs. 5.1 and 5.2 describe our initial beam to be amplified as well as the initial purity. It is more convenient to express the polarisation vectors in terms of horizontal and vertical states $\hat{\mathbf{e}}_\mathbf{H}$ and $\hat{\mathbf{e}}_\mathbf{V}$, respectively. Strictly speaking, this removes the cylindrical symmetry, so that the study is of a more general vector beam beam represented by a point on the Generalised HOPS. Our beam is then

$$U(r,\phi) = \sqrt{\alpha}\exp(i\ell\phi)\hat{\mathbf{e}}_\mathbf{H} + \sqrt{1-\alpha}\exp(-i\ell\phi)\hat{\mathbf{e}}_\mathbf{V}, \tag{5.3}$$

Now we wish to amplify the beam in Eq. 5.3 through a general amplifier. To specify the fast axis we introduce an angle θ to denote the angle of the fast axis relative to the vertical, as shown in Fig. 5.1. Each polarisation component of our vector field will experience an amplification factor that is dependent on the orientation of the field relative to the crystal. We define the initial amplification factors for the $\theta = 0$ case in Jones matrix form as

$$M = \begin{pmatrix} \sqrt{\eta_{h0}} & 0 \\ 0 & \sqrt{\eta_{v0}} \end{pmatrix}, \tag{5.4}$$

where η_h and η_v are the amplification factors for both horizontal and vertical polarisation.

Without any loss of generality we imagine the case where the amplifier is orientated to have initial amplification factors η_{h0} and η_{v0} for horizontal and vertical polarisation, respectively (defined at $\theta = 0$). Now when the amplifier crystal is rotated through an angle θ, as depicted in Fig. 5.1 (b), the state alters and is given by

$$\tilde{U} = R(\theta)\cdot M \cdot R(-\theta)\cdot U,$$

where $R(\theta)$ is the rotation matrix for the linear basis. Thus

$$\tilde{U} = \begin{pmatrix} \cos\theta & -\sin\theta \\ \sin\theta & \cos\theta \end{pmatrix}\begin{pmatrix} \sqrt{\eta_{h0}} & 0 \\ 0 & \sqrt{\eta_{v0}} \end{pmatrix}\begin{pmatrix} \cos\theta & \sin\theta \\ -\sin\theta & \cos\theta \end{pmatrix}\cdot U,$$

or

$$\tilde{U} = \begin{pmatrix} a_1\exp(i\ell\phi) + a_3\exp(-i\ell\phi) \\ a_2\exp(i\ell\phi) + a_4\exp(-i\ell\phi) \end{pmatrix}, \tag{5.5}$$

This is a pure state but not always separable. Now the new modal weighting coefficients are determined from

$$a_1 = \sqrt{\alpha}\left(\sqrt{\eta_{h0}}\cos^2\theta + \sqrt{\eta_{v0}}\sin^2\theta\right), \tag{5.6}$$

$$a_3 = \sqrt{1-\alpha}\cos\theta\sin\theta\left(\sqrt{\eta_{h0}} - \sqrt{\eta_{v0}}\right), \tag{5.7}$$

and

$$a_2 = \sqrt{\alpha}\cos\theta\sin\theta\left(\sqrt{\eta_{h0}} - \sqrt{\eta_{v0}}\right), \tag{5.8}$$

$$a_4 = \sqrt{1-\alpha}\left(\sqrt{\eta_{v0}}\cos^2\theta + \sqrt{\eta_{h0}}\sin^2\theta\right). \tag{5.9}$$

To calculate the purity we first normalise the coefficients so that $\sum_i |a_i|^2 = 1$ and then calculate the purity from the density matrix of the state, ρ, following $V = \sqrt{1 - \mathrm{Tr}(\rho)}$ with $\rho = |\tilde{U}\rangle\langle\tilde{U}|$ and where Tr is the trace operator. This results in an analytical expression given by

$$V = \frac{2|a_1a_4 - a_2a_3|}{\sum_i |a_i|^2}. \tag{5.10}$$

Thus,

$$V = \left|\frac{2\sqrt{\eta_h\eta_v}}{\eta_h + \eta_v + (\eta_h - \eta_v)(2\alpha - 1)\cos(2\theta)}\right| V_{\mathrm{in}}. \tag{5.11}$$

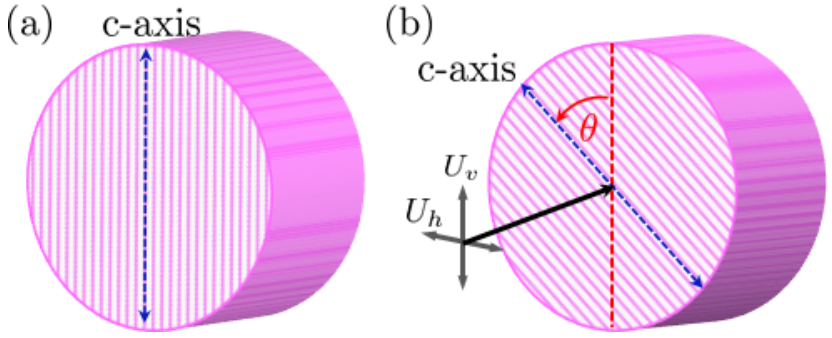


FIGURE 5.1: Schematic of a general solid state amplifier crystal. (a) shows the crystal positioned with its fast axis at an angle $\theta = 0$ with respect to the vertical. (b) shows the two field components relative to the c-axis when the crystal is rotated by an angle θ.

Equation 5.10 implies that the purity of the amplified VV beam is dependent on the modal weighting α of the input seed beam, the amplifier orientation θ as well as the amplification factors η_h and η_v. The former are parameters determined from the beam to be amplified while the latter can be obtained from the rate equations of the gain media. Once η_h and η_v are known, the behaviour of any beam on the Generalized HOPS through

an arbitrary gain can be predicted. To find these parameters we consider the case where the crystal is end-pumped by an unpolarised beam of intensity I_p, so that the absorption of the pump beam is denoted by

$$\frac{\partial I_p\left(x,y,z\right)}{\partial z} = -\sigma_a n_1\left(x,y,z\right) I_p\left(x,y,z\right), \tag{5.12}$$

while the amplification of the seed at any point in the gain medium is given by

$$\frac{\partial\left(I_{sh}\left(x,y,z\right)+I_{sv}\left(x,y,z\right)\right)}{\partial z} = n_2\left(x,y,z\right)\left(\sigma_{eh} I_{sh}\left(x,y,z\right)+\sigma_{ev} I_{sv}\left(x,y,z\right)\right) \tag{5.13}$$

where I_{sh} and I_{sv} are the intensities for the horizontal and vertical components of the seed beam, respectively. σ_a is the absorption cross-section of the active ions in the ground energy level (n_1), while σ_{eh} and σ_{ev} are the emission cross-sections of the upper laser energy level (n_2) for the horizontal and vertical polarisations, respectively, with a lifetime of τ_2.

For such a system the rate equation is

$$\frac{\partial n_2\left(x,y,z\right)}{\partial t} = \sigma_a n_1\left(x,y,z\right)\frac{I_p\left(x,y,z\right)}{h\nu_p} - n_2\left(x,y,z\right) \left(\frac{\sigma_{eh} I_{sh}\left(x,y,z\right)+\sigma_{ev} I_{sv}\left(x,y,z\right)}{h\nu_s} - \frac{1}{\tau_2}\right), \tag{5.14}$$

where $h\nu_p(h\nu_s)$ is the energy per photon at the pump (seed) wavelength.

From Eq. 5.13 we can derive how each polarisation competes for upper level electrons (gain):

$$\frac{\partial I_{sh}\left(x,y,z\right)}{\partial I_{sv}\left(x,y,z\right)} = \frac{\sigma_{eh} I_{sh}\left(x,y,z\right)}{\sigma_{ev} I_{sv}\left(x,y,z\right)}. \tag{5.15}$$

The number of photons generated for a given polarisation state is proportional to the intensity of the polarisation state multiplied by the emission cross section of the polarisation and inversely proportional to the competing polarisation. Assuming steady-state (when the pump and seed beams have no temporal change in intensity) and the small signal gain operation regime of the amplifier ($\sigma_a I_p >> \sigma_{eh} I_{sh} + \sigma_{ev} I_{sv}$), these coupled equations simplify to

$$\sigma_a \frac{I_p(x,y,z)}{h\nu_p}\left[n_{\text{tot}} - n_2(x,y,z)\right] = \frac{n_2(x,y,z)}{\tau_2}, \tag{5.16}$$

where conservation of ions ($n_1 = n_{\text{tot}} - n_2$) has been assumed. From Eq. 5.16 we can derive the equation for the pump intensity I_p as a function of the upper level population

density n_2,

$$I_p\left(x,y,z\right) = I_p(x,y,z_0)\exp\left(-\sigma_a[n_{\text{tot}} - n_2(x,y,z)]z\right), \tag{5.17}$$

provided that $z\frac{\partial n_2}{\partial z}$ is small compared to $n_{\text{tot}} - n_2$.

In order to obtain the population density of the ions in the upper level we assume the case of low gain amplifier (i.e. the gain medium is not saturated by the pump), namely that $n_{\text{tot}} >> n_2$. This assumption yields a solution for the upper level population n_2, namely,

$$n_2\left(z\right) = \frac{I_p\left(z_0\right) n_{\text{tot}}\sigma_a\tau_2}{h\nu_p\exp(-\sigma_a n_{\text{tot}}z) + \sigma_a\tau_2 I_p\left(z_0\right)}. \tag{5.18}$$

Based on the above we can determine the maximum intensity for which this approach is valid,

$$I_p^{\max}\left(z_0\right) = \frac{\delta}{\left(1-\delta\right)}\frac{h\nu_p}{\sigma_a\tau_2}, \tag{5.19}$$

where $\delta = n_2^{\max}/n_{\text{tot}}$ is the ratio of the density of ions in the upper laser level to the total density of ions. Based on the zero order equation for n_2 (see Eq. 5.13 and Eq. 5.18) we can find the analytical connection between the intensity profiles of the seed and pump beams for both polarisation states by integrating Eq. 5.13,

$$I_{sv}\left(x,y,L\right) = I_{sv}\left(x,y,z_0\right)\left(1+\frac{\sigma_{ev}}{\sigma_a}\xi\right) \tag{5.20}$$

$$I_{sh}\left(x,y,L\right) = I_{sh}\left(x,y,z_0\right)\left(1+\frac{\sigma_{eh}}{\sigma_a}\xi\right), \tag{5.21}$$

where

$$\xi = Ln_{\text{tot}}\sigma_a + \log\left[\frac{h\nu_p + \tau_2\sigma_a I_p\left(x,y,z_0\right)}{h\nu_p\exp(Ln_{\text{tot}}\sigma_a) + \tau_2\sigma_a I_p\left(x,y,z_0\right)}\right]. \tag{5.22}$$

Here z_0 and L represent the incident and output amplifier crystal planes, respectively, and $I_p(x,y,z_0)$ is the intensity profile of the pump beam.

Thus the amplification factors η_h and η_v are given by

$$\eta_h = 1+\frac{\sigma_{eh}}{\sigma_a}\xi \tag{5.23}$$

$$\eta_v = 1+\frac{\sigma_{ev}}{\sigma_a}\xi. \tag{5.24}$$

For isotropic amplifiers, the emission cross-section is independent of polarisation, so $\eta_{h0} = \eta_{v0} = \eta_0$. In this special case the output vector state is identical to the input (purity remains the same) but with an increase in power, i.e. $\tilde{U} = \sqrt{\eta_0}U$.

In contrast, birefringent amplifiers generally have different emission cross-sections for each polarisation due to the difference in the refractive indices of the crystal axes and

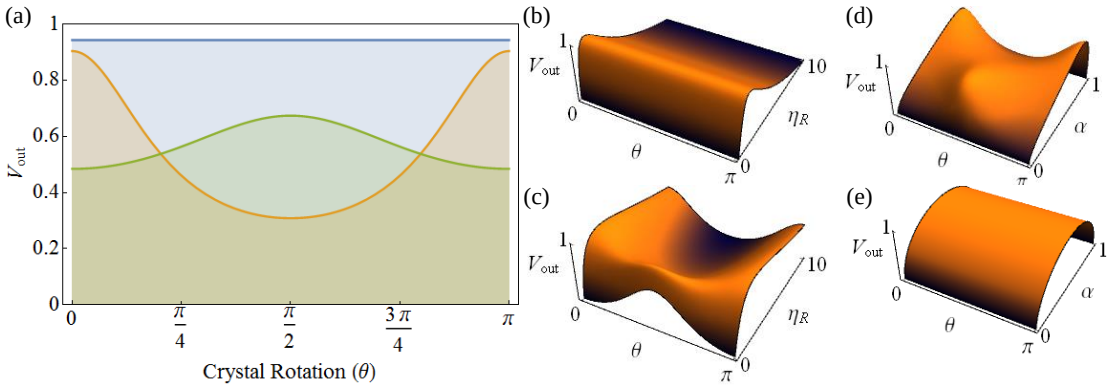


FIGURE 5.2: (a) The Vector Quality Factor, V_{out}, as a function of crystal angle, θ, for three cases: $\alpha = 0.5$ and $\eta_R = 2$ (blue), $\alpha = 0.8$ and $\eta_R = 0.1$ (orange), and $\alpha = 0.4$ and $\eta_R = 0.1$ (green). The 3D plots of the parameter space show the richness of the theory, with the input state fixed in (b) and (c) at $\alpha = 0.5$ and $\alpha = 0.7$, respectively. In (d) and (e) the amplification factor is fixed at $\eta_R = 0.2$ and $\eta_R = 1$, respectively.

thus $\eta_{h0} \neq \eta_{v0}$. Here, each component of the vector state is amplified differently so that the vector nature (purity) itself changes along with the power content. Some examples of the effect of a birefringent amplifier are shown in Fig. 5.2, where the output purity V_{out} is plotted against the the crystal rotation angle θ, the initial amplification ratio $\eta_R = \eta_{h0}/\eta_{v0}$ at $\theta = 0$, and α controls the input purity V_{in}.

We see From Eq.5.11 when the input VV beam is pure ($V_{\text{in}} = 1$), the output vector purity is not a function of the crystal rotation angle and is always less than or equal to the input, as seen in the blue line of Fig. 5.2 (a). This is understandable as a special case where the beam's polarisation structure is rotationally symmetric and thus invariant to the crystal rotation. When $\alpha \neq 0.5$ this is no longer true, and we note that the vector purity may increase and/or decrease depending on the initial purity and amplification terms. For example, when the vertical component is initially larger and has higher amplification than the horizontal, shown in the orange curve of Fig. 5.2 (a), the output purity is always less than the input. Conversely, when the vertical component is initially smaller than the horizontal but has higher amplification, the purity increases as the power weighting of the modes equalise (green curve). Note that whether or not the purity can be returned to $V_{\text{out}} = 1$ depends on the amplification ratio being sufficient to overcome the initial modal mismatch (in power weighting). This behaviour is further explored in Figs. 5.2 (b) - (e).

When the initial state is symmetric in polarisation or the amplification ratio is unity, then the purity is independent of the crystal angle, as shown in Figs. 5.2 (b) and (e). However, when this is not the case the purity can be increased to a maximum of $V_{\text{out}} = 1$ or decreased according to the parameters of the initial beam and the medium, illustrated in Figs. 5.2 (c) and (d). It is this evolution in purity that we wish to uncover experimentally.

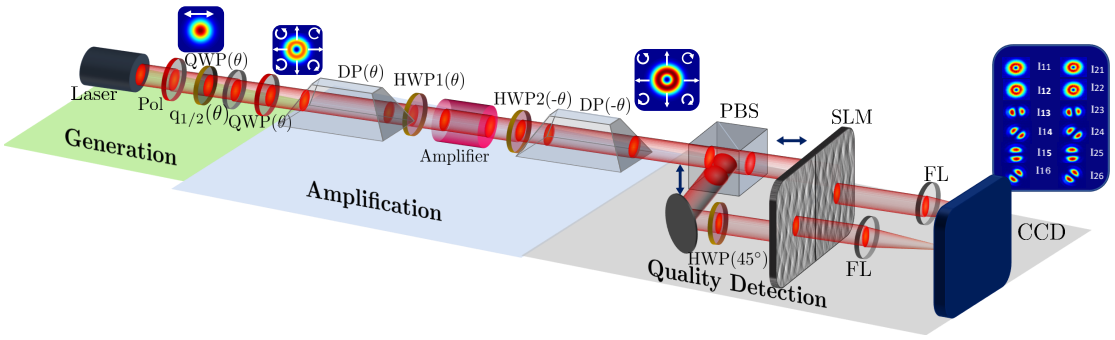


FIGURE 5.3: Illustration of the experimental setup for the MOPA system. Generation: a fundamental Gaussian mode was converted into a HOPS beam by the combination of a polariser (Pol), quarter-wave plate (QWP) and a q-plate. In our experiment the q-plate had a topological charge $\ell = 2q = 1$. Amplification: either Nd:YAG (non-birefringent) or Nd:YLF (birefringent) crystals, with the ability to rotate the field relative to the crystal axes by the use of half wave plates (HWP) and Dove Prisms (DP). Quality Detection: a polarising beam splitter (PBS) separated the two polarisation components (horizontal and vertical) while the spatial light modulator (SLM) performed spatial projections to infer the vector purity using a quantum toolkit. The actual measurements were collected on a camera (CCD) in the far-field at the focal plane of a lens (FL). The beam insets show the evolution from the Gaussian mode through to an amplified vector beam (radially polarised in this example), finally measured by twelve projections at the camera.

5.3 Experimental Setup

The experiment is divided into three parts: generation, amplification and quality measurement of arbitrary VV beams, as illustrated in Fig. 5.3. The master oscillator was a diode pumped solid state laser with either a gain medium of Nd:YAG for an output wavelength of 1.064 μm, or Nd:YLF for an output wavelength of 1.053 μm. Both oscillators were set to produce fundamental modes of high purity, while the initial polarisation was controlled by a combination of a polariser (Pol) and a quarter-wave plate (QWP). The desired state on the HOPS was prepared by passing this beam through a custom geometric phase element, a q-plate with geometric charge $\ell = 1$ then a QWP. It is evident that any state on the HOPS could be produced, from OAM scalar modes on the poles to hybrid vector vortex beams on the equator, all by control of the polarisation states incident on the q-plate.

The amplifier consisted of either Nd:YAG or Nd:YLF crystals (length 48 mm and diameter 7 mm) maintained at room temperature and end-pumped by fiber delivered diode laser (25 W at $\lambda = 808$ nm). The two gain media were chosen to cover both non-birefringent and birefringent gain conditions. Together with the generation stage the entire system represents the well-known master oscillator power amplifier (MOPA) arrangement. The experiment requires the gain media to be rotated in order to study the impact of θ, which can be viewed as the alignment of the vector beam polarisation states to the optical axis of the crystal; this influences the gain for each component of the field.

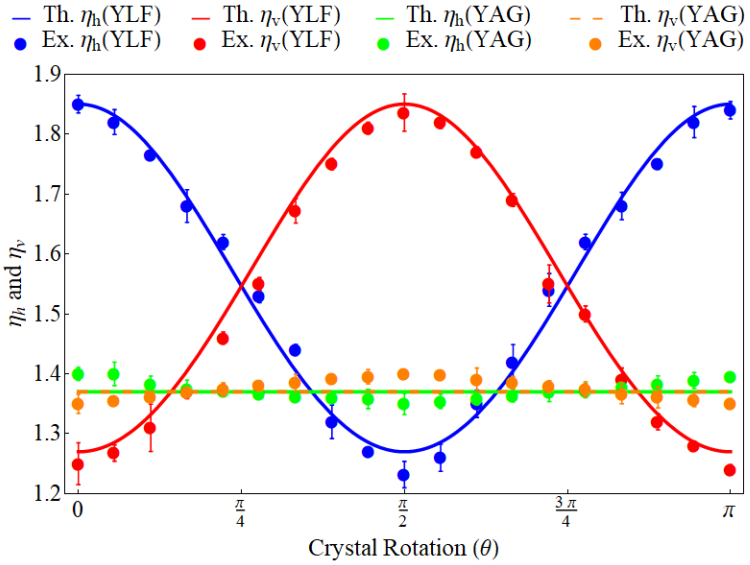


FIGURE 5.4: Measured (data points) and theoretical (solid lines) amplification factors for each polarisation component for the two crystals as a function of the crystal angle. Nd:YLF is a strong birefringent medium resulting in the oscillating behaviour, while Nd:YAG is a weakly birefringent resulting in almost equal gain for both the horizontal and vertical components of the beam. No fitting parameters were used in the theoretical plots.

This relative rotation was achieved by rotating the incident field using a half-wave plate (HWP) and a dove prism (DP). To undo this effect prior to measurement, a second DP and HWP was applied.

The vector purity V was determined by measuring the coefficients in the expansion shown in Eq. 5.5. This was experimentally realised by using a polarising beam splitter (PBS) to separate the incident field into the horizontal and vertical polarised components, U_H and U_V, and then directing them to a spatial light modulator (SLM) encoded with the necessary spatial projections [121, 131, 132].

5.4 Results & Discussion

With the MOPA active (pump on), the amplification factors for the horizontal and vertical polarisation components, η_h and η_v respectively, were measured as a function of the crystal orientation. The results are shown in Fig. 5.4 for the two crystal types (birefingent Nd:YLF and isotropic Nd:YAG amplifiers).

It is clear that the experimental results (data points) are in excellent agreement with the theory (solid lines), shown here without any fitting parameters and calculated from the rate equation model. For Nd:YAG we see that the two amplification factors, η_h (green dashed line) and η_v (orange dashed line), are approximately the same and independent

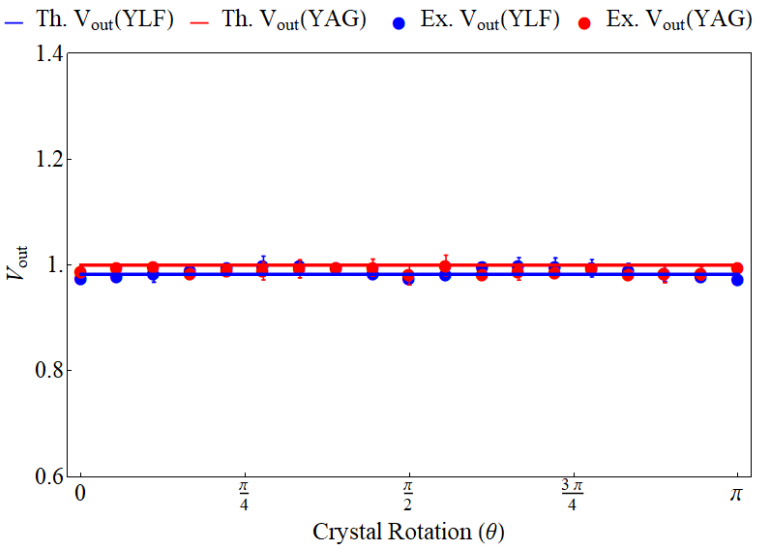


FIGURE 5.5: Purity of VV beams over the different orientation of Nd:YAG (red) and Nd:YLF (blue) amplifiers when the seed VV beam has purity $V_{\text{in}} = 1$.

of crystal orientation rotation angle, while for Nd:YLF the amplification factors oscillate with rotation angle in a predictable manner.

Such behavior is as expected due to the weak birefringence property in the Nd:YAG medium, while Nd:YLF is a strong birefringent medium resulting in lower gain for one polarisation when the amplifier oriented at its c-axis ($\theta = 0$). As the crystal is rotated so the amplification factors invert their values.

Herein lies the ability to compensate for poor initial vector quality by use of a birefringent gain: the ratio of amplification can be selected to bring the vector beam back to the ideal.

Next, a pure VV beam of purity $V = 1$ was generated and passed through the amplifier. The quality of the amplified output beam was measured over the different orientations of the amplifier crystal, as in Fig. 5.5. Theory predicts no change in purity, in agreement with experiment: the quality of the amplified VV beam was found to be 0.98 and 0.99 for Nd:YLF and Nd:YAG amplifiers, respectively. The pure VV beam acts similarly inside both amplifiers regardless of the birefringence.

If the quality of the incident vector beam is not perfect, i.e. moving off the equator of the HOPS, then the purity of the amplified beam becomes highly dependent on the nature of the amplifier. This has been demonstrated by generating two VV beams $\tilde{U}_1 = 0.976\exp(i\ell\phi)\hat{\mathbf{e}}_{\mathbf{H}} + 0.267\exp(-i\ell\phi)\hat{\mathbf{e}}_{\mathbf{V}}$ and $\tilde{U}_2 = 0.267\exp(i\ell\phi)\hat{\mathbf{e}}_{\mathbf{H}} + 0.976\exp(-i\ell\phi)\hat{\mathbf{e}}_{\mathbf{V}}$, that have the same quality $V = 0.5$, and studying the change in purity as a function of the amplifier's angle, as illustrated in Fig. 5.6. After amplification through the Nd:YAG amplifier, the quality of the VV beams remained unchanged and independent of the

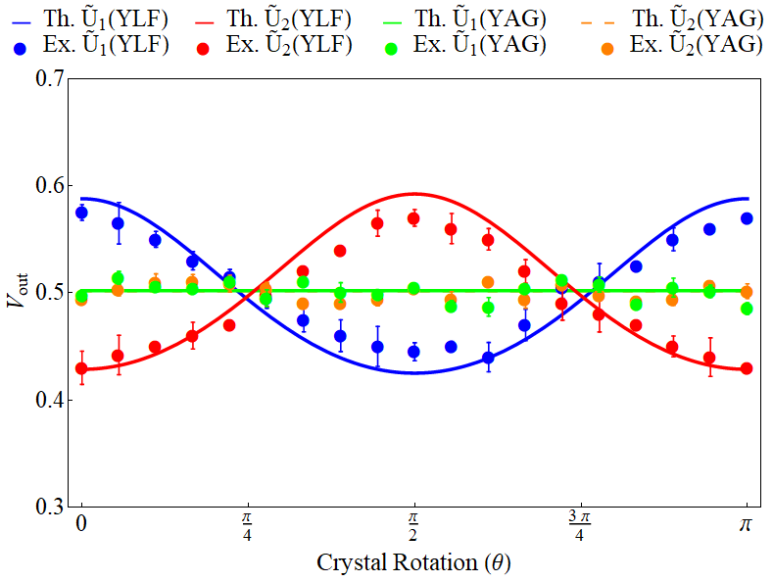


FIGURE 5.6: Measured (data points) and calculated (solid lines) purity variation as a function of the crystal angle for two incident VV beams: $\tilde{U}_1 = 0.976\exp(i\ell\phi)\,\hat{\mathbf{e}}_\mathbf{H} + 0.267\exp(-i\ell\phi)\,\hat{\mathbf{e}}_\mathbf{V}$ and $\tilde{U}_2 = 0.267\exp(i\ell\phi)\,\hat{\mathbf{e}}_\mathbf{H} + 0.976\exp(-i\ell\phi)\,\hat{\mathbf{e}}_\mathbf{V}$, both having initial purity of $V_{\text{in}} = 0.5$. For Nd:YAG, the purity is predicted not to change, in agreement with measured data showing only a marginal oscillation about $V_{\text{out}} = 0.5$. For Nd:YLF the purity for $\tilde{U}_1$ (blue) and $\tilde{U}_2$ (red) oscillate predictably. At some angles the purity decreases ($\theta = 0$ for $\tilde{U}_2$) while at others it increases ($\theta = \pi/2$ for $\tilde{U}_2$).

angle θ. In contrast, the quality of the amplified beam through the Nd:YLF amplifier oscillates predictably in purity. This suggests that the angle of the crystal can be adjusted to maintain or even improve the purity of the beam during amplification. For

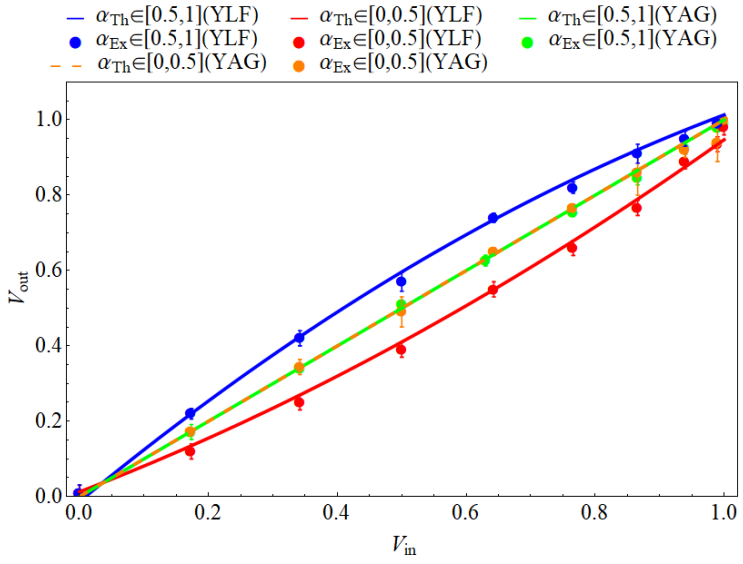


FIGURE 5.7: Measured (data points) and calculated (solid lines) variation in purity after the amplifier with the crystal angle fixed at $\theta = 0$. For Nd:YLF, the blue dots represent the output purity for beams with $\alpha \in [0.5, 1]$ in Eq. 5.1. The red dots represent the output purity for beams with $\alpha \in [0, 0.5]$. For Nd:YAG, the purity does not change and equates to the purity of the incident seed beam.

example, at $\theta = \pi/2$ the purity of the $\tilde{U}_2$ mode actually increases close to 0.6 from the initial 0.5. Theory predicts that this can be increased all the way to 1 if the medium has sufficient gain, perhaps even by using crystals in tandem.

Next, we adjusted the purity of the incident HOPS beams from 0 to 1 at crystal orientation $\theta = 0$ and measured the purity of the amplified beam V_{out} and plotted the results versus the theoretical predictions from Eq. 5.11 as shown in Fig. 5.7. The purity of the amplified beam through the Nd:YAG remains unchanged due to the weak birefringence effect, while for the strong birefringent Nd:YLF gain, the purity of the beam evolves according to the incident state.

Finally, we measured the average output power of a purely VV beam, $V_{\text{in}} = 1$, as a function of the amplifier pump power (after a single pass through the amplifier) as shown in Fig. 5.8. The power of the incident seed VV beam was constant at 164 mW. Figure 5.8 shows the inset images for the beam intensity profile at different pump powers with their output purity. While the power of the amplified VV beam increases either through the Nd:YAG (red data points) or Nd:YLF (blue data points) amplifiers, the purity of the output beam remains unchanged, consistent with theory shown in Fig. 5.5.

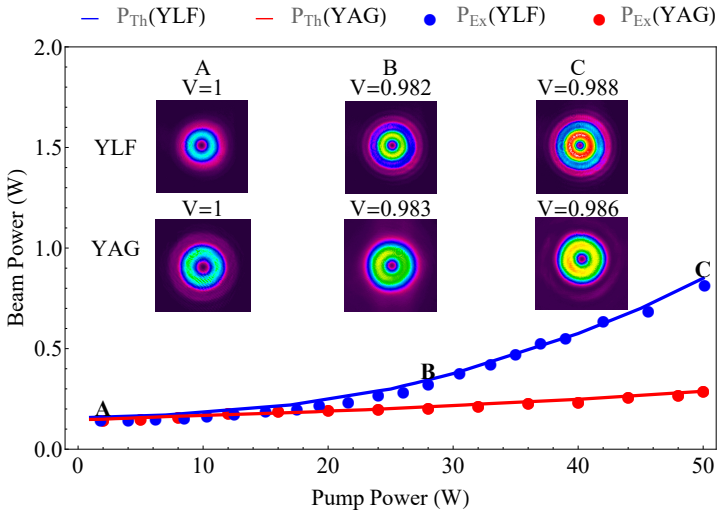


FIGURE 5.8: The output power for a purely VV seed beam as a function of the amplifier pump power. The initial power of the seed beam was 164 mW. The experimental data (data points) for both Nd:YAG (red) and Nd:YLF (blue) amplifiers is in good agreement with theory (solid curves). Inset images indicate the beam intensity profiles with the corresponding output purity at three pump strengths: low (A), medium (B) and high (C).

Conclusion

We have demonstrated a new approach to obtain high purity amplified VV beams through a MOPA system. We outlined the complete theory that accounts for both the amplification and purity aspects of general VV beams, which we believe provides a useful toolbox for further high-power work in this field. It is well understood from traditional scalar beam amplification studies that laser brightness requires the power to increase but not at the expense of the beam quality. The same is true for vector beams. Here we consider both aspects, an important step towards realizing high brightness vector beams. Further, the match between experiment and theory is excellent, and has been achieved without any fitting parameters. Our work shows that it is possible to maintain or even improve vector purity during amplification.

Chapter 6

Conclusion

The work presented in this thesis aimed to investigate intra-cavity generation of new families of structured light modes from solid state laser resonators. Over the course of Chapter 1, a literature review covering the basic theory of optical resonators and the solution of such resonators have been discussed using the Helmholtz wave equation and diffraction theory. We also explored some of these solutions, which are utilised in this thesis, such as Gaussian and Laguerre Gaussian beams. The approach to distinguish these modes by decomposing any beam into its basis modes, known as modal decomposition, was discussed. We presented the general problem of shaping laser beams and different approaches that can be exploited to structure exotic modes inside or outside the resonator.

In Chapter 2, we demonstrated the first experimental evidence for fractal light from canonical unstable resonators. We observed a variety of fractal shapes in transverse intensity cross-sections through the lowest-loss eigenmodes of unstable laser resonators, thereby demonstrating the controlled generation of a new family of structured light modes with fractal geometry inside a laser cavity. We showed, quantitatively, that intensity cross-sections are the most self-similar in the magnified self-conjugate plane. We also advanced the existing theory of fractal laser modes by showing that imaging and diffraction also occurs in the longitudinal direction, resulting in 3D self-similar fractal structure around the centre of the magnified self-conjugate plane. This work offered a significant advance in the understanding of a fundamental symmetry of Nature as found in lasers.

In Chapter 3 we demonstrated a novel laser that generates HOPS beams by manipulating the geometric phase of light using metasurface J-plates. We generated pure OAM states as well as vector vortex beams that can be mapped on the HOPS. In principle, our laser has no limitation over the OAM that can be generated. Subsequently, we proved this

by generating the largest pure OAM state with $\ell = 100$ as well as the largest vector vortex beams of net OAM $\ell = 110$. The significance of this Chapter was to demonstrate a novel laser system that allows controlling light's different degrees of freedom such as wavelength, polarisation and azimuthal modes.

In Chapter 4, the question on how to measure the quality of the HOPS beams was addressed. Since all HOPS beams possess the same propagating divergence, i.e. M^2 is identical, Thus traditional quality measurements do not apply for these beams. The quality of these beams was measured using qualitative techniques to distinguish scalar and vector modes. However, there were no quantitative techniques that can tell how vector the mode is. Because vector beams can be viewed as "entangled" or non-separable in their spatial and polarisation degrees of freedom, we applied entanglement measures to quantify this quintessential property of vector modes, which we called the vector purity. This tool allowed to quantify the purity of any HOPS beam on a scale from 0 (pure scalar modes) to 1 (pure vector modes). We demonstrated this technique on a variety of HOPS beams in a continuous range from purely scalar to purely vector. This technique offers a new tool for laser beam characterisation of vector modes.

Despite the many advances in the generation of vector vortex beams, they are limited to low power applications due to the power handling capabilities of the generation tools. Many high power applications highlighted a need for high power HOPS beams. Although the amplification of particular HOPS beams have been extensively researched, they have been limited to isotropic amplifiers. The purity of the beam, which is a crucial property, never been considered. The question of how the purity of vector beams changes under amplification was addressed in Chapter 5. In this chapter we employed a master-oscillator-power-amplifier approach and studied the problem of purity of HOPS beams through vector beam amplifiers. The gain media, Nd:YAG and Nd:YLF, were selected to cover both non-birefringent and birefringent conditions, respectively. We executed this study both theoretically and experimentally, showing excellent agreement between the two. Intriguingly, we showed that pure vector vortex beams maintain their vector purity regardless of the gain medium, while general vector vortex beams may have their purity improved by the use of a suitable birefringent amplifier. Importantly, our results highlighted a road map towards high brightness vector beams, a core requirement for applications such as laser-enabled manufacturing and long-distance optical communication in free space and fiber.

Future work

In Chapter 2, we have confirmed the emergence of 2D self-similar fractal light from a laser system while we extended the theory to the 3D fractals. When not considered in the context of resonators, the existence of 3D self-similar fractal light fields is surprising: the 3D intensity distribution of any light field is fully determined by any transverse cross-section, and so the lowest-loss eigenmode is fully determined by its cross-section in the magnified self-conjugate plane. The existence of self-similar transverse cross-sections whose corresponding beams - their 3D diffraction patterns - are also self-similar is a non trivial task due to a limitation in the imaging of the longitudinal direction of the beam. The future work could include developing imaging techniques to experimentally realise 3D fractals. Also, the type of applications, where this family of structured modes could be utilised, will still be an ongoing research that we will be partaking in future.

The selective excitation of a pure Laguerre Gaussian modes from a solid-state laser resonator was discussed in Chapter 3. We showed that it is possible to control many degrees of light in one resonator (i.e. wavelength, azimuthal mode and the polarisation). These results provide a possible route for future work of controlling all degrees of freedom of laser beams. The future work would include extra-cavity controlling the radial modes of the beam which can be achieved by many techniques such as printing a radial phase mask into the J-plates or into the output coupler or maybe shape the radial modes of the pump beam.

Intra-cavity beam shaping has been demonstrated using different static and custom optical elements that require design and fabrication efforts and their performance deteriorated with the variation in the beam size. These elements necessitated custom designed resonators, rather than being very limited to select a particular spatial mode. The well-known digital laser also suffered from many drawbacks such as limitations over the power handling capabilities of the device, the slow time switching ($\approx$ 60 Hz) as well as being limited to modulate only particular wavelengths. Digital micromirror device (DMD) may provide a possible route for future work of laser beam shaping due to their fast switching rates (20 kHz), polarisation insensitivity, their higher power capability, and spectrum sensitivity [133]. DMD has millions of tiny switchable mirrors. Each mirror of the device can individually switched to either +12° (on-state or white) or -12° (off-state or black) with respect to the surface normal. The DMD can tailor and control the phase, amplitude of light using binary amplitude modulation. The DMD also provide real-time mode controlling and switching by mechanically flipping the micromirrors from one state to the other. These advantages will prove to be significant for many applications ranging from optical communication to remote sensing and metrology.

Bibliography

[1] Wikipedia contributors. Optical cavity — Wikipedia, the free encyclopedia, 2018. [Online; accessed 20-November-2018].

[2] J. A. Baker and C. W. Peters. Mode selection and enhancement with a ruby laser. *Applied Optics*, 1(5), 1962.

[3] T. Li. Diffraction loss and selection of modes in maser resonators with circular mirrors. *Bell System Technical Journal*, 44(5), 1965.

[4] A. F. Abouraddy and K. C. Toussaint. Three-dimensional polarization control in microscopy. *Physical Review Letters*, 96(15), 2006.

[5] Q. Zhan. Trapping metallic rayleigh particles with radial polarization. *Optics Express*, 12(15), 2004.

[6] K. T. Gahagan and G. A. Swartzlander. Optical vortex trapping of particles. *Optics Letters*, 21(11), 1996.

[7] J. Ng, Z. Lin, and C. T. Chan. Theory of optical trapping by an optical vortex beam. *Physical Review Letters*, 104(10), 2010.

[8] Y. Kozawa and S. Sato. Optical trapping of micrometer-sized dielectric particles by cylindrical vector beams. *Optics Express*, 18(10), 2010.

[9] B. J. Roxworthy and K. C. Toussaint Jr. Optical trapping with π-phase cylindrical vector beams. *New Journal of Physics*, 12(7), 2010.

[10] M. G. Donato, S. Vasi, R. Sayed, P. H. Jones, F. Bonaccorso, A. C. Ferrari, P. G. Gucciardi, and O. M. Maragò. Optical trapping of nanotubes with cylindrical vector beams. *Optics Letters*, 37(16), 2012.

[11] V. Parigi, V. D'Ambrosio, C. Arnold, L. Marrucci, F. Sciarrino, and J. Laurat. Storage and retrieval of vector beams of light in a multiple-degree-of-freedom quantum memory. *Nature Communications*, 6, 2015.

[12] C. E. Souza, C. V. Borges, A. Z. Khoury, J. A. Huguenin, L. Aolita, and S. P. Walborn. Quantum key distribution without a shared reference frame. *Physical Review A*, 77(3), 2008.

[13] X. Li, T. H. Lan, C. H. Tien, and M. Gu. Three-dimensional orientation-unlimited polarization encryption by a single optically configured vectorial beam. *Nature Communications*, 3, 2012.

[14] A. Forbes. Controlling light's helicity at the source: orbital angular momentum states from lasers. *Philosophical Transactions of the Royal Society A*, 375(2087), 2017.

[15] N. Hodgson and H. Weber. *Laser Resonators and Beam Propagation: Fundamentals, Advanced Concepts, Applications*. Springer, 2005.

[16] A. E. Siegman. Lasers university science books. 1986.

[17] H. Kogelnik and T. Li. Laser beams and resonators. *Applied Optics*, 5(10), 1966.

[18] A. G Fox and T. Li. Resonant modes in a maser interferometer. *Bell System Technical Journal*, 40(2), 1961.

[19] I. A. Litvin. *Intra–cavity laser beam shaping*. PhD thesis, 2010.

[20] A. L. Dudley. *Superpositions of light fields carrying orbital angular momentum*. PhD thesis, 2012.

[21] A. Holleczek, A. Aiello, C. Gabriel, C. Marquardt, and G. Leuchs. Classical and quantum properties of cylindrically polarized states of light. *Optics Express*, 19(10), 2011.

[22] G. Deschamps and P. Mast. Poincaré sphere representation of partially polarized fields. *IEEE Transactions on Antennas and Propagation*, 21(4), 1973.

[23] G. Milione, H. I. Sztul, D. A. Nolan, and R. R. Alfano. Higher-order poincaré sphere, stokes parameters, and the angular momentum of light. *Physical Review Letters*, 107, 2011.

[24] M. J. Padgett and J. Courtial. Poincaré-sphere equivalent for light beams containing orbital angular momentum. *Optics Letters*, 24(7), 1999.

[25] G. S. Agarwal. Su (2) structure of the poincaré sphere for light beams with orbital angular momentum. *JOSA A*, 16(12), 1999.

[26] C. Rosales-Guzmán, B. Ndagano, and A. Forbes. A review of complex vector light fields and their applications. *Journal of Optics*, 20(12), 2018.

[27] G. Milione, S. Evans, D. A. Nolan, and R. R. Alfano. Higher order pancharatnam-berry phase and the angular momentum of light. *Physical Review Letters*, 108(19), 2012.

[28] A. E. Siegman. Defining and measuring laser beam quality. In *Solid State Lasers*. Springer, 1993.

[29] C. Schulze, A. Dudley, D. Flamm, M. Duparre, and A. Forbes. Measurement of the orbital angular momentum density of light by modal decomposition. *New Journal of Physics*, 15(7), 2013.

[30] F. M. Dickey. *Laser beam shaping: theory and techniques*. CRC press, 2014.

[31] F. M. Dickey, S. C. Holswade, T. E. Lizotte, and D. L. Shealy. *Laser beam shaping applications*. CRC Press, 2005.

[32] D. L. Shealy and J. A. Hoffnagle. Laser beam shaping profiles and propagation. *Applied Optics*, 45(21), 2006.

[33] I. A. Litvin, G. King, and H. Strauss. Beam shaping laser with controllable gain. *Applied Physics B*, 123(6), 2017.

[34] A. Forbes. *Laser beam propagation: generation and propagation of customized light*. CRC Press, 2014.

[35] V. Samarkin and A. Kudryashov. Deformable mirrors for laser beam shaping. In *Laser Beam Shaping Xi*, volume 7789. International Society for Optics and Photonics, 2010.

[36] J. A. Hoffnagle and C. M. Jefferson. Refractive optical system that converts a laser beam to a collimated flat-top beam, September 25 2001. US Patent 6,295,168.

[37] V. Peet. Biaxial crystal as a versatile mode converter. *Journal of Optics*, 12(9), 2010.

[38] X. Tan, B. Y. Gu, G. Z. Yang, and B. Z. Dong. Diffractive phase elements for beam shaping: a new design method. *Applied Optics*, 34(8), 1995.

[39] Y. Zhang, B. Z. Dong, B. Y. Gu, and G. Z. Yang. Beam shaping in the fractional fourier transform domain. *JOSA A*, 15(5), 1998.

[40] D. C. O'Shea, T. J. Suleski, A. D. Kathman, and D. W. Prather. *Diffractive optics: design, fabrication, and test*. Spie Press Bellingham, WA, 2004.

[41] E. Cagniot, M. Fromager, T. Godin, N. Passilly, M. Brunel, and K. Ait-Ameur. Variant of the method of fox and li dedicated to intracavity laser beam shaping. *JOSA A*, 28(3), 2011.

[42] G. A. Turnbull, D. A. Robertson, G. M. Smith, L. Allen, and M. J. Padgett. The generation of free-space laguerre-gaussian modes at millimetre-wave frequencies by use of a spiral phaseplate. *Optics Communications*, 127(4-6), 1996.

[43] A. Forbes, A. Dudley, and M. McLaren. Creation and detection of optical modes with spatial light modulators. *Advances in Optics and Photonics*, 8(2), 2016.

[44] F. Wilczek and A. Shapere. *Geometric phases in physics*. World Scientific, 1989.

[45] M. V. Berry. The adiabatic phase and pancharatnam's phase for polarized light. *Journal of Modern Optics*, 34(11), 1987.

[46] G. Milione, S. Evans, D. A. Nolan, and R. R. Alfano. Higher order pancharatnam-berry phase and the angular momentum of light. *Physical Review Letters*, 108(19), 2012.

[47] L. Marrucci, C. Manzo, and D. Paparo. Optical spin-to-orbital angular momentum conversion in inhomogeneous anisotropic media. *Physical Review Letters*, 96(16), 2006.

[48] E. Karimi, B. Piccirillo, E. Nagali, L. Marrucci, and E. Santamato. Efficient generation and sorting of orbital angular momentum eigenmodes of light by thermally tuned q-plates. *Applied Physics Letters*, 94(23), 2009.

[49] S. Slussarenko, A. Murauski, T. Du, V. Chigrinov, L. Marrucci, and E. Santamato. Tunable liquid crystal q-plates with arbitrary topological charge. *Optics Express*, 19(5), 2011.

[50] B. Walther, C. Helgert, C. Rockstuhl, F. Setzpfandt, F. Eilenberger, E. B. Kley, F. Lederer, A. Tünnermann, and T. Pertsch. Spatial and spectral light shaping with metamaterials. *Advanced Materials*, 24(47), 2012.

[51] A. Arbabi, Y. Horie, M. Bagheri, and A. Faraon. Dielectric metasurfaces for complete control of phase and polarization with subwavelength spatial resolution and high transmission. *Nature Nanotechnology*, 10(11), 2015.

[52] P. Genevet, F. Capasso, F. Aieta, M. Khorasaninejad, and R. Devlin. Recent advances in planar optics: from plasmonic to dielectric metasurfaces. *Optica*, 4(1), 2017.

[53] D. Wen, F. Yue, W. Liu, S. Chen, and X. Chen. Geometric metasurfaces for ultrathin optical devices. *Advanced Optical Materials*, 6(17), 2018.

[54] S Pancharatnam. The adiabatic phase and pancharatnam's phase for polarized light. In *Proc. Indian Acad. Sci*, volume 44, 1956.

[55] R. Oron, Y. Danziger, N. Davidson, A. A. Friesem, and E. Hasman. Discontinuous phase elements for transverse mode selection in laser resonators. *Applied Physics Letters*, 74(10), 1999.

[56] R. Oron, N. Davidson, A. A. Friesem, E. Hasman, and E. Wolf. Transverse mode shaping and selection in laser resonators. *Progress in Optics*, 42(6), 2001.

[57] H. C. Eckstein and U. D. Zeitner. Experimental realization of a diffractive unstable resonator with gaussian amplitude of the outcoupled beam using a vecsel amplifier. *Optics Express*, 17(20), 2009.

[58] D. Naidoo, M. Fromager, K. Äit-Ameur, and A. Forbes. Radially polarized cylindrical vector beams from a monolithic microchip laser. *Optical Engineering*, 54(11), 2015.

[59] P. A. Bélanger and C. Paré. Optical resonators using graded-phase mirrors. *Optics Letters*, 16(14), 1991.

[60] P. A. Belanger, R. L. Lachance, and C. Pare. Super-gaussian output from a co 2 laser by using a graded-phase mirror resonator. *Optics Letters*, 17(10), 1992.

[61] D. Naidoo, I. A. Litvin, and A. Forbes. Brightness enhancement in a solid-state laser by mode transformation. *Optica*, 5(7), 2018.

[62] U. D. Zeitner, F. Wyrowski, and H. Zellmer. External design freedom for optimization of resonator originated beam shaping. *IEEE Journal of Quantum Electronics*, 36(10), 2000.

[63] D. Naidoo, F. S. Roux, A. Dudley, I. Litvin, B. Piccirillo, L. Marrucci, and A. Forbes. Controlled generation of higher-order poincaré sphere beams from a laser. *Nature Photonics*, 10(5), 2016.

[64] B. B. Mandelbrot. *The fractal geometry of nature*. WH freeman New York, 1982.

[65] K. O'Holleran, M. R. Dennis, F. Flossmann, and M. J. Padgett. Fractality of light's darkness. *Physical Review Letters*, 100(5), 2008.

[66] M. Lehman and M. Garavaglia. Beam reflection from multilayers with periodic and fractal distributions. *Journal of Modern Optics*, 46(11), 1999.

[67] D. H. Werner and S. Ganguly. An overview of fractal antenna engineering research. *IEEE Antennas and propagation Magazine*, 45(1), 2003.

[68] M. Lehman. Fractal diffraction gratings built through rectangular domains. *Optics Communications*, 195(1-4), 2001.

[69] G. Saavedra, W. D. Furlan, and J. A. Monsoriu. Fractal zone plates. *Optics Letters*, 28(12), 2003.

[70] S. Kirihara, M. W. Takeda, K. Sakoda, K. Honda, and Y. Miyamoto. Strong localization of microwave in photonic fractals with menger-sponge structure. *Journal of the European Ceramic Society*, 26(10-11), 2006.

[71] M. V. Berry and S. Z. Klein. Integer, fractional and fractal talbot effects. *Journal of Modern Optics*, 43(10), 1996.

[72] M. Berry, C. Storm, and W. Van Saarloos. Theory of unstable laser modes: edge waves and fractality. *Optics Communications*, 197(4-6), 2001.

[73] G. P. Karman and J. P. Woerdman. Fractal structure of eigenmodes of unstable-cavity lasers. *Optics Letters*, 23(24), 1998.

[74] G. P. Karman, G. S. McDonald, G. H. New, and J. P. Woerdman. Laser optics: Fractal modes in unstable resonators. *Nature*, 402(6758), 1999.

[75] G. H. New, M. A. Yates, J. P. Woerdman, and G. S. McDonald. Diffractive origin of fractal resonator modes. *Optics Communications*, 193(1-6), 2001.

[76] M. Berry. Fractal modes of unstable lasers with polygonal and circular mirrors. *Optics Communications*, 200(1-6), 2001.

[77] M. A. Yates and G. H. New. Fractal dimension of unstable resonator modes. *Optics Communications*, 208(4), 2002.

[78] J. A. Loaiza. *Experimental demonstration of the fractal nature of unstable-resonator modes*. PhD thesis, 2005.

[79] J. G. Huang, J. M. Christian, and G. S. McDonald. Fresnel diffraction and fractal patterns from polygonal apertures. *JOSA A*, 23(11), 2006.

[80] D. Avnir, O. Biham, D. Lidar, and O. Malcai. Is the geometry of nature fractal? *Science*, 279(5347), 1998.

[81] J. Courtial and M. J. Padgett. Monitor-outside-a-monitor effect and self-similar fractal structure in the eigenmodes of unstable optical resonators. *Physical Review Letters*, 85(25), 2000.

[82] C. M. Watterson, M. J. Padgett, and J. Courtial. Classic-fractal eigenmodes of unstable canonical resonators. *Optics Communications*, 223(1-3), 2003.

[83] J. A. Loaiza, E. R. Eliel, and J. P. Woerdman. Experimental observation of fractal modes in unstable optical resonators. *arXiv preprint physics/0304046*, 2003.

[84] J. A. Rivera, T. C. Galvin, A. W. Steinforth, and J. G. Eden. Fractal modes and multi-beam generation from hybrid microlaser resonators. *Nature Communications*, 9(1), 2018.

[85] A. Forrester, M. Lönnqvist, M. J. Padgett, and J. Courtial. Why are the eigenmodes of stable laser resonators structurally stable? *Optics Letters*, 27(21), 2002.

[86] Young tim source code. ,https://sourceforge.net/projects/javawaveoptics/. Accessed: 2015.

[87] E. A. Sziklas and A. E. Siegman. Mode calculations in unstable resonators with flowing saturable gain. 2: Fast fourier transform method. *Applied Optics*, 14(8), 1975.

[88] J. Courtial, J. Leach, and M. J Padgett. Image processing: Fractals in pixellated video feedback. *Nature*, 414(6866), 2001.

[89] J. Leach, M. J. Padgett, and J. Courtial. Fractals in pixellated video feedback. *Contemporary Physics*, 44(2), 2003.

[90] W. H. Press, W. H. Press, B. P. Flannery, B. P. Flannery, S. A. Teukolsky, and W. T. Vetterling. *Numerical recipes in Pascal: the art of scientific computing*. Cambridge University Press, 1989.

[91] L. Wang, Y. Zhang, and J. Feng. On the euclidean distance of images. *IEEE Transactions on Pattern Analysis and Machine Intelligence*, 27(8), 2005.

[92] D. Naidoo, K. Ait-Ameur, I. Litvin, M. Fromager, and A. Forbes. Observing mode propagation inside a laser cavity. *New Journal of Physics*, 14(5), 2012.

[93] M. V. Berry. Diffractals. *Journal of Physics A: Mathematical and General*, 12(6), 1979.

[94] H. Rubinsztein-Dunlop, A. Forbes, M. V. Berry, M. R. Dennis, D. L. Andrews, M. Mansuripur, C. Denz, C. Alpmann, P. Banzer, T. Bauer, et al. Roadmap on structured light. *Journal of Optics*, 19(1), 2016.

[95] X. Yi, Y. Liu, X. Ling, X. Zhou, Y. Ke, H. Luo, S. Wen, and D. Fan. Hybrid-order poincaré sphere. *Physical Review A*, 91(2), 2015.

[96] Y. Liu, Z.and Liu, Y. Ke, Y. Liu, W. Shu, H. Luo, and S. Wen. Generation of arbitrary vector vortex beams on hybrid-order poincaré sphere. *Photonics Research*, 5(1), 2017.

[97] S. C. Tidwell, D. H. Ford, and W. D. Kimura. Generating radially polarized beams interferometrically. *Applied Optics*, 29(15), 1990.

[98] N. Passilly, R. de Saint Denis, K. Aït-Ameur, F. Treussart, R. Hierle, and J. Roch. Simple interferometric technique for generation of a radially polarized light beam. *JOSA A*, 22(5), 2005.

[99] W. M. Lee, X. C. Yuan, and W. C. Cheong. Optical vortex beam shaping by use of highly efficient irregular spiral phase plates for optical micromanipulation. *Optics Letters*, 29(15), 2004.

[100] C Maurer. C. maurer, a. jesacher, s. fürhapter, s. bernet, and m. ritsch-marte. *New Journal of Physics*, 9, 2007.

[101] C. Rosales-Guzmán, N. Bhebhe, and A. Forbes. Simultaneous generation of multiple vector beams on a single slm. *Optics Express*, 25(21), 2017.

[102] L. Marrucci, C. Manzo, and D. Paparo. Pancharatnam-berry phase optical elements for wave front shaping in the visible domain: switchable helical mode generation. *Applied Physics Letters*, 88(22), 2006.

[103] L. Marrucci, E. Karimi, S. Slussarenko, B. Piccirillo, E. Santamato, E. Nagali, and F. Sciarrino. Spin-to-orbital conversion of the angular momentum of light and its classical and quantum applications. *Journal of Optics*, 13(6), 2011.

[104] L. Marrucci. Rotating light with light: Generation of helical modes of light by spin-to-orbital angular momentum conversion in inhomogeneous liquid crystals. In *Liquid Crystals and Applications in Optics*, volume 6587, 2007.

[105] F. Cardano, E. Karimi, S. Slussarenko, L Marrucci, C. de Lisio, and E. Santamato. Polarization pattern of vector vortex beams generated by q-plates with different topological charges. *Applied Optics*, 51(10), 2012.

[106] P. Chen, W. Ji, B. Y Wei, W. Hu, V. Chigrinov, and Y. Q. Lu. Generation of arbitrary vector beams with liquid crystal polarization converters and vector-photoaligned q-plates. *Applied Physics Letters*, 107(24), 2015.

[107] X. Yi, X. Ling, Z. Zhang, Y. Li, X. Zhou, Y. Liu, S. Chen, H. Luo, and S. Wen. Generation of cylindrical vector vortex beams by two cascaded metasurfaces. *Optics Express*, 22(14), 2014.

[108] Z. Zhao, J. Wang, S. Li, and A. E. Willner. Metamaterials-based broadband generation of orbital angular momentum carrying vector beams. *Optics Letters*, 38(6), 2013.

[109] F. Yue, D. Wen, J. Xin, B. D. Gerardot, J. Li, and X. Chen. Vector vortex beam generation with a single plasmonic metasurface. *ACS photonics*, 3(9), 2016.

[110] E. Karimi, S. A. Schulz, I. De Leon, H. Qassim, J. Upham, and R. W. Boyd. Generating optical orbital angular momentum at visible wavelengths using a plasmonic metasurface. *Light: Science & Applications*, 3(5), 2014.

[111] Ronen C. Michael Y. Vladimir K. Erez H. Asher A. F. Maguid, E. and Nir D. Topologically controlled intracavity laser modes based on pancharatnam-berry phase. *ACS Photonics*, 5(5), 2018.

[112] R. Chriki, E. Maguid, C. Tradonsky, V. Kleiner, A. A. Friesem, N. Davidson, and E. Hasman. Spin-controlled twisted laser beams: intra-cavity multi-tasking geometric phase metasurfaces. *Optics Express*, 26(2), 2018.

[113] R. C. Devlin, A. Ambrosio, N. A. Rubin, J. P. B. Mueller, and F. Capasso. Arbitrary spin-to–orbital angular momentum conversion of light. *Science*, 358(6365), 2017.

[114] R. C. Devlin, M. Khorasaninejad, W. T. Chen, J. Oh, and F. Capasso. Broadband high-efficiency dielectric metasurfaces for the visible spectrum. *Proceedings of the National Academy of Sciences*, 113(38), 2016.

[115] A. E. Siegman. Laser beams and resonators: beyond the 1960s. *IEEE Journal of Selected Topics in Quantum Electronics*, 6(6), 2000.

[116] A. E. Siegman. Defining the effective radius of curvature for a nonideal optical beam. *IEEE Journal of Quantum Electronics*, 27(5), 1991.

[117] C. Schulze, D. Flamm, M. Duparré, and A. Forbes. Beam-quality measurements using a spatial light modulator. *Optics Letters*, 37(22), 2012.

[118] V. V. G. K. Inavalli and N. K. Viswanathan. Switchable vector vortex beam generation using an optical fiber. *Optics Communications*, 283(6), 2010.

[119] G. Milione, M. P.J. Lavery, H. Huang, Y. Ren, G. Xie, T. A. Nguyen, E. Karimi, L. Marrucci, D. A. Nolan, R. R. Alfano, et al. 4× 20 gbit/s mode division multiplexing over free space using vector modes and a q-plate mode (de) multiplexer. *Optics Letters*, 40(9), 2015.

[120] W. K. Wootters. Entanglement of formation and concurrence. *Quantum Information & Computation*, 1(1), 2001.

[121] M. McLaren, T. Konrad, and A. Forbes. Measuring the nonseparability of vector vortex beams. *Physical Review A*, 92(2), 2015.

[122] G. Milione, H. I. Sztul, D. A. Nolan, J. Kim, M. Etienne, J. McCarthy, J. Wang, and R. R. Alfano. Cylindrical vector beam generation from a multi elliptical core

optical fiber. In *CLEO: Science and Innovations*. Optical Society of America, 2011.

[123] B. Jack, J. Leach, H. Ritsch, S. M. Barnett, M. J. Padgett, and S. Franke-Arnold. Precise quantum tomography of photon pairs with entangled orbital angular momentum. *New Journal of Physics*, 11(10), 2009.

[124] Y. Liu, X. Ling, X. Yi, X. Zhou, H. Luo, and S. Wen. Realization of polarization evolution on higher-order poincaré sphere with metasurface. *Applied Physics Letters*, 104(19), 2014.

[125] B. Ndagano, R. Brüning, M. McLaren, M. Duparré, and A. Forbes. Fiber propagation of vector modes. *Optics Express*, 23(7), 2015.

[126] J. Kim, Y. Li, M. N. Miskiewicz, C. Oh, M. W. Kudenov, and M. J. Escuti. Fabrication of ideal geometric-phase holograms with arbitrary wavefronts. *Optica*, 2(11), 2015.

[127] A. Trichili, C. Rosales-Guzmán, A. Dudley, B. Ndagano, A. B. Salem, M. Zghal, and A. Forbes. Optical communication beyond orbital angular momentum. *Scientific Reports*, 6, 2016.

[128] M. A. Ahmed, J. Schulz, A. Voss, O. Parriaux, J. Pommier, and T. Graf. Radially polarized 3kw beam from a co 2 laser with an intracavity resonant grating mirror. *Optics Letters*, 32(13), 2007.

[129] P. B. Phua and W. J. Lai. Simple coherent polarization manipulation scheme for generating high power radially polarized beam. *Optics Express*, 15(21), 2007.

[130] M. A. Ahmed, M. Haefner, M. Vogel, C. Pruss, A. Voss, W. Osten, and T. Graf. High-power radially polarized yb: Yag thin-disk laser with high efficiency. *Optics Express*, 19(6), 2011.

[131] B. Ndagano, H. Sroor, M. McLaren, C. Rosales-Guzmán, and A. Forbes. Beam quality measure for vector beams. *Optics Letters*, 41(15), 2016.

[132] H. Sroor, N. Lisa, D. Naidoo, I. Litvin, and A. Forbes. Purity of vector vortex beams through a birefringent amplifier. *Physical Review Applied*, 9(4), 2018.

[133] Y. X. Ren, R. D. Lu, and L. Gong. Tailoring light with a digital micromirror device. *Annalen der Physik*, 527(7-8), 2015.